ELECTRONIC AND OPTOELECTRONIC DEVICES BASED ON 2D MATERIALS

Hüseyin ŞAR

PhD Thesis

Electrical and Electronics Engineering Program

Eskişehir 2019

ELECTRONIC AND OPTOELECTRONIC DEVICES BASED ON 2D MATERIALS

Hüseyin ŞAR

PhD THESIS

Electrical & Electronics Engineering
Supervisor: Assoc. Prof. Dr. Feridun AY

Eskişehir
Eskişehir Technical University
Institute of Graduate Programs
September 2019

This thesis has been supported by the project BAP 1606F568 and partially by BAP 116F445, which were accepted by the BAP Commission.

FINAL APPROVAL FOR THESIS

This thesis titled “Electronic and Optoelectronic Devices based on 2D Materials” has been prepared and submitted by Hüseyin ŞAR in partial fulfillment of the requirements in “Eskişehir Technical University Directive on Graduate Education and Examination” for the Degree of Doctor of Philosophy (PhD) in Electrical and Electronics Engineering Department has been examined and approved on 27/09/2019.

Comittee Members		**Title Name Surname**	**Signature**
Member (Supervisor) :		Doç. Dr. Feridun AY	……..
Member	:	Doç. Dr. Cem SEVİK	……..
Member	:	Doç. Dr. Nihan K. PERKGÖZ	……..
Member	:	Prof. Dr. Hilmi Volkan DEMİR	……..
Member	:	Prof. Dr. İdris AKYÜZ	……..

……..

Director of Institute of Graduate Programs

ÖZET

İKİ BOYUTLU MALZEMELER TABANLI ELEKTRONİK VE OPTOELEKTRONİK AYGITLAR

Hüseyin ŞAR

Elektrik ve Elektronik Mühendisliği Anabilim Dalı
Telekomünikasyon Bilim Dalı

Eşkişehir Teknik Üniversitesi, Lisansüstü Eğitim Enstitüsü, Eylül 2019

Danışman: Doç. Dr. Feridun AY

Bu tez çalışmasında, iki boyutlu (2B) malzemeler üzerine, bir çok karakterizasyon metodu kullanılarak kapsamlı bir araştırma yapılmıştır. 2B yapılar, bizim tarafımızdan kurulmuş kimyasal buhar biriktirme (KBB) sistemi ile büyütülmüş, büyütme parametreleri ve konfigürasyonları optimize edilmiştir. Bu malzemelerin tek katmanlarının yanı sıra, farklı tek katmanlardan oluşan heteroyapılar da üretilmiş ve Raman ve Fotolüminesans (PL) spektroskopi yöntemleri ile incelenmişlerdir. Grafen üzerine yerleştirilmiş MoS_2'nin PL şiddetinin, tek katman haline oranla, grafen ve MoS_2 arasındaki yük geçişinden kaynaklı 10 kat sönümlendiği görülmüştür. Ayrıca, grafen yüzeyinde yüksek yoğunluktaki çekirdeklenme noktalarından kaynaklı olarak, grafen üzerine doğrudan MoS_2 büyütme işlemi, nanometre boyutlarında tek katman yapraklar ve mikrometre boyutlarında kalın MoS_2 yığınları ile sonuçlanmıştır. Bunlara ek olarak, KBB ile büyütülmüş MoS_2 nin uzun dönem dayanıklılığı incelenmiştir. Yüksek yoğunluktaki çekirdeklenmeden dolayı yüksek büyüme hızı ile büyümüş MoS_2 yapılarının normal ortam koşulları altında kararsız oldukları ortaya konmuştur. Bu nedenle, düşük büyüme hızı sağlayan özgün bir büyütme konfigürasyonu önerilmiş ve bu önerilen metodun yetkinliği, uzun dönem gözlemler, termal yaşlandırma deneyleri ve yoğunluk fonksiyonelleri teorisi hesaplamaları ile kanıtlanmıştır. Ayrıca, MoS_2 ve WS_2'nin FET aygıt performansları, özdeş koşullarda koşulları altında incelenmiş ve bu cihazlar, sırası ile ~10^4 ve ~10^5 gibi akım AÇ/KAPA oranları ve yine sırası ile 1.45 ve 0.98 $cm^2V^{-1}s^{-1}$ gibi nispeten yüksek taşıyıcı mobiliteleri göstermişlerdir. WS_2 tabanlı aygıtların, ortam koşullarına karşı daha hassas oldukları ortaya çıkarılmıştır. Bunlara ek olarak, performans artırma metodu olarak, MoS_2 tabanlı fototransistorler, kolloidal kuantum kuyuları ile hassaslaştırılmış ve enerji transeri yoluyla yükseltilmiş soğurmadan kaynaklı ~11 katlık bir foto-duyarlılık artışı elde edilmiştir.

Anahtar Kelimeler: Grafen, MoS_2, WS_2, FET, Fototransistor,

ABSTRACT

ELECTRONIC AND OPTOELECTRONIC DEVICES BASED ON 2D MATERIALS

Hüseyin ŞAR

Department of Electrical & Electronics Engineering
Programme in Telecommunication

Eskişehir Technical University, Institute of Graduate Programs , September 2019

Supervisor: Assoc. Prof. Dr. Feridun AY

In this thesis, a comprehensive study on 2D materials has been carried out and investigated by various characterization tools. The 2D materials have been grown by in-house CVD system and the growth parameters and configuration have been optimized. Not only individual monolayers, but also their heterostructures, have been obtained and investigated by Raman and Photoluminescence spectroscopy. It has been found that, the PL intensity of MoS_2 on top of the graphene is quenched with a factor of 10 due to charge transfer between MoS_2 and graphene. In addition, direct growth of MoS_2 on top of graphene resulted in nanometer sized flakes and bulky micrometer stacks of MoS_2, mainly due to higher density of seeding spots on graphene. Furthermore, the long-term stability of the CVD-grown MoS_2 has been investigated. It has been found that higher growth rate due to higher seeding density, results in relatively unstable MoS_2 structures under ambient atmosphere conditions. A novel growth configuration with slower growth rate is proposed and the effectiveness of the proposed method has been verified by long-term observations, thermal aging experiments and DFT calculations. Device performance investigations of MoS_2 and WS_2 have been investigated under identical conditions. The FETs of MoS_2 and WS_2 show reasonably high current ON/OFF ratios and mobilities of ~10^4 and ~10^5 and 1.45 $cm^2V^{-1}s^{-1}$ and 0.98 $cm^2V^{-1}s^{-1}$, respectively. It is found that WS_2 shows higher sensitivity to environmental conditions. Furthermore, as a performance enhancement method, the MoS_2 phototransistor has been sensitized by colloidal quantum wells and ~11-fold photoresponsivity enhancement has been achieved by increase of absorbance via energy transfer.

Keywords: Graphene, 2D Materials, CVD, MoS_2, WS_2 FET, MoS_2 Phototransistor,

ACKNOWLEDGEMENTS

First and foremost, as a member and now an alumni member of Micro Nano Systems and Devices Research Group (MIDAS), I would like to express my sincere gratitude to my advisors: Assoc. Prof. Dr. Feridun AY, Assoc. Prof. Dr. Cem SEVİK and Assoc. Prof. Dr. Nihan KOSKU PERKGÖZ for providing one of the best possible working environments available in Turkey. I have immense respect. Their broad visions, critical observations and expert experimental and theoretical skills never cease to inspire me. Their wise advices and patient guidance have been as determinative to my personal and academic character. It has been my great fortune and honor to work in their lab, and for this I will forever be thankful.

I would like to also express my gratitude to my thesis committee members (Prof. Dr. Hilmi Volkan Demir and Prof. Dr. İdris AKYÜZ a) for their critical reading and valuable comments.

I would like to thank my friends and colleagues in MIDAS research group (Ayberk Özden, İlker Demiroğlu, Büşra YORULMAZ, Cem ODACI, Ezgi ŞAHİN, Merve ÖPER, Mustafa DEMİRTAŞ, Mehmet BAY, and Tuğbey KOCABAŞ) for their direct contribution to this work. I would like to also thank the rest of the MIDAS research group and my friends in other departments of Eskisehir Technical University for their friendship and great fun.

Last but not the least, I would like to thank my wife Dilan Güneş Şar for her unconditional emotionally support -throughout my degree. I could not have imagined overcoming this study without her support. And finally, I offer my biggest thanks to my family.

Hüseyin ŞAR

September 2019

27.09.2019

STATEMENT OF COMPLIANCE WITH ETHICAL PRINCIPLES AND RULES

I hereby truthfully declare that this thesis is an original work prepared by me; that I have behaved in accordance with the scientific ethical principles and rules throughout the stages of preparation, data collection, analysis and presentation of my work; that I have cited the sources of all the data and information that could be obtained within the scope of this study, and included these sources in the references section; and that this study has been scanned for plagiarism with "scientific plagiarism detection program" used by Anadolu University, and that "it does not have any plagiarism" whatsoever. I also declare that, if a case contrary to my declaration is detected in my work at any time, I hereby express my consent to all the ethical and legal consequences that are involved

Hüseyin ŞAR

TABLE OF CONTENTS

LIST OF FIGURES

Page

Page

Page

LIST OF TABLES

INDEX OF ABBREVIATIONS AND SYMBOLS

2D : Two Dimensional

PL : Photoluminescence

TMD : Transition Metal Dichalcogenide

FLIM : Fluorescence Lifetime Imaging

CVD : Chemical Vapor Deposition

CMOS **:** Complementary Metal Oxide Semiconductor

MOSFET : Metal Oxide Semiconductor Field Effect Transistor

VBM : Valance Band Maximum

FET : Field Effect Transistor

EOT : Equivalent Gate Oxide Thickness

vdWs : Van der Waals

FD **:** Face-Down

HO **:** Horizontal

CQWs **:** Colloidal Quantum Wells

R **:** Responsivity

D* **:** Specific Detectivity

CBM : Conduction Band Minimum

σ : Electrical Conductivity

μ : Charge Carrier Mobility

n : Charge Carrier Density

e : Electrical Charge

1. INTRODUCTION

1.1. Introduction

Today's electronics industry is heavily relying on on field effect transistors (FETs) devices. It is based mainly on semiconductor Silicon, in one single transistor architecture called complementary metal oxide semiconductor (CMOS) which consist of n-type and p-type silicon-based metal oxide semiconductor field effect transistors (Si-MOSFETs) on the same body [1]. So that, FETs (n-type or p-type) can be defined as the unit blocks of the huge modular technology system. In this manner, the progress of modern communication, defense, space, health and information technologies relies on the performance enhancement and size shrinking of this unit blocks (FETs) which means smaller and more efficient devices in relevant application areas. From the macro-scale transistors to multiple-gate FETs with 5 nm equivalent gate oxide thickness (EOT), (from past to present) more performance with smaller size, called as Moore's Law trend, has been followed. According to Moore's Law, the number transistor in an integrated circuit will double per 18 months with increased complexity and lowered costs [2]. However, the silicon based electronic components has almost reached its limits of shrinking down, because of very thin EOT thickness (higher leakages) like 10 nm or less and moderate carrier mobilities which limits high speed and more efficient electronics [3]. To exceed the mobility limits of the silicon-based devices, application of strain to the silicon itself has been used. Lately, strained Si based CMOS circuits have widely been used in the market [4]. In addition to that, the research on high-mobility III-V and Ge based devices are intensively pushed forward [5, 6]. As a most recent solution to EOT, the multi gated transistors are being used in latest IC technology, which relies on fine structured channel and high-k oxide layer as gate-oxide [6]. A higher performance with lower power consumption is achieved with this new architecture. However, all these attempts are partial and temporary solutions to needs of the market for much efficient devices. A promising and efficient solution is the introduction of novel channel materials into FET technology. After invention of the graphene with its extraordinary properties such as high mobility, high thermal conductivity, high mechanical strength, etc, it has attracted a great attention for electronic applications [7].

The era of two-dimensional (2D) materials, also known as van der Waals materials, has begun by the isolation of one-layer graphene from its bulk form (graphite) with its mentioned extraordinary properties above [7]. The expectations from graphene particularly raised after the observed and estimated high carrier mobility and have seen as a successor of the conventional semiconductor technology. The gapless nature of monolayer graphene which is essential for digital electronics and predominantly FETs, has lowered the high expectation after early days of it. Even if the Nobel prized graphene could not meet the expectation in FET technology, it pioneered the rise of a new research field so-called 2D materials and showed promising performance in sensing, plasmonics, radio frequency (RF) devices, heat sinks, and similar applications [8, 9]. During the interest drop in graphene, Radisavljevic *et al*. showed the superior FET operation performance (a carrier mobility of 200 $cm^2\ V^{-1}\ s^{-1}$ and room-temperature current on/off ratios of 1×10^8) of single layer MoS_2, which is a member of 2D material family know as transition metal chalcogenides (TMDs) [10]. After this work, a new momentum has been gained on graphene and other 2D material research. In a relatively short period of time, hundreds of new 2D materials with different electronic properties (2D semiconductors, 2D metal and 2D insulators) have been discovered and 2D materials family expanded [3]. The predicted novel physical phenomena and expected application performances contributed to this expansion and growing interest. Some of the novel physical phenomena reported for 2D materials can be named as unusual quantum hall effects in monolayer and bilayer graphene (or in silicene and germanene [11]), Berry’s phase [12], very large spin-orbit coupling in TMDs [13], accessible valley degree of freedom or valley polarization (in graphene and TMDs) [14], or thickness dependent band-gap, *etc.* [15].

In Figure 1.1, the citation report created from web of science academic search engine by the keywords “2D materials, Electronic” is demonstrated. The total number of publications about electronics of 2D materials (Figure 1.1a) and the sum of times cited of 2D materials (Figure 1.1b) indicates an exponential increase, proofs the growing importance and interest of 2D materials-based electronics year by year. Furthermore, the annual reports of the International Technology Roadmap for Semiconductors (ITRS), the strategic planning document of the semiconductor industry, has stated Graphene and other 2D materials as candidates for future electronics since 2011 [16].

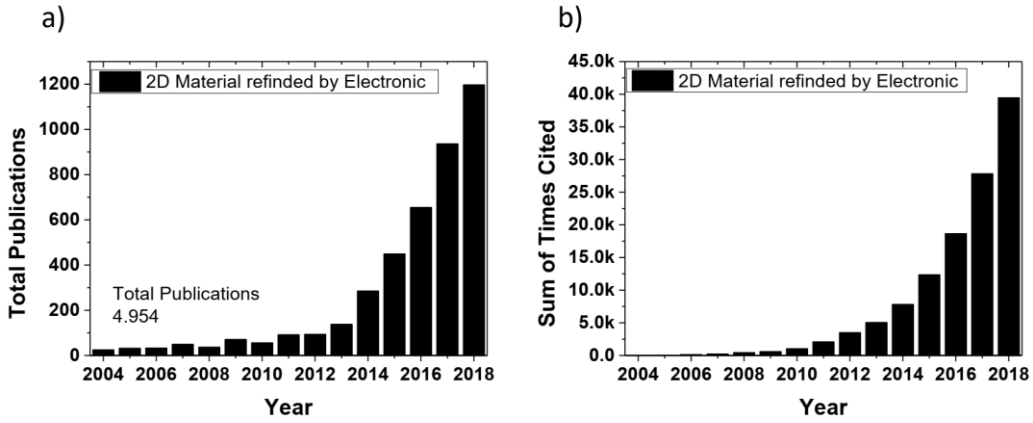

Figure 1.1. *Web of Science citation report created by the keywords "2D materials, Electronic": (a) The total number of publications per year and (b) The sum of times cited per year [17].*

In this regard, not only the extraordinary properties of 2D material, but also their ability to form vertical or lateral heterostructures while preserving their individual properties within heterostructure make them attractive in the literature and industry[18]. This ability of 2D materials brings the possibility of the purpose-specific channel structure design for any type of electronic or optoelectronic applications.

In summary, 2D materials are one of the most promising candidates for future electronics with their unique properties and ability to form efficient heterostructures. However, reaching these goals has some fundamental requirements such as large-area, high-quality growth, development of defect free transfer methods or substrate-independent epitaxial growth, characterization of single layers or form heterostructures to understand the physics behind, novel device architectures and fabrication methods with efficient encapsulation techniques. The listed requirements can be considered as the next steps of 2D materials research field.

1.2. Motivation of The Study

Regarding the general perspective given in the previous section, this dissertation contributes to fabricating high performance 2D materials based electronic and optoelectronic devices. The main approaches to achieve this goal are large area, controlled, homogeneous and high-quality growth of 2D materials, forming heterostructures like Graphene/MoS_2 and using high-k dielectrics in fabricated devices. In addition to these, this study contributes to the long-term physical stability of 2D TMDs by proposing a novel growth strategy. The growth technique is chosen as chemical vapor

deposition (CVD) method because of being a cost-effective, large area growth capable method among the other methods. The importance of the CVD technique is discussed more in details in the following chapters. Graphene, MoS_2 and WS_2 are the chosen target materials as channel materials for the fabricated devices. Besides, the focus of this dissertation is not only induvial monolayers of 2D materials but also their heterostructures such as Graphene/MoS_2 which is formed by transferring or direct-growth. The optimization and process of each task from growth to final device fabrication is investigated in detail to be able to achieve control on material quality and the effects of material growth method on the stability and performance of the final devices. These tasks can be summarized as follows; growth of large area high quality 2D materials with novel approaches, investigation of optimum transfer method for transferring the grown structures to target substrates, physical and optical characterization of the as-grown and transferred structures by several characterization tools such as Raman Spectroscopy, PL, Temperature dependent PL measurements, Fluorescence Lifetime measurements, Atomic Force Microscopy (AFM) and Scanning Electron Microscopy (SEM), performing all device fabrication steps using Optical/e-beam lithography and electronic/optoelectronic characterization of final devices.

The thesis contains the research outputs over a span of five years of a PhD degree study at the department of Electrical & Electronics Engineering, Eskisehir Technical University. It constitutes of 8 chapters. Starting with a general perspective on 2D material-based electronics and the motivation of this study. The brief literature review related to the thesis topic is presented in Chapter 2. Chapter 3 covers the experimental techniques including the growth, transfer, characterization and device fabrication of 2D materials. The details of forming Graphene/MoS2 heterostructure by transferring or direct growth are given in Chapter 4. Chapter 5 summarizes the growth configuration related long-term stability of TMDs. The proposed CVD growth configuration is supported by the characterization of naturally and thermally aged MoS_2 structures. Chapter 6 demonstrates the device performance comparison of MoS_2 and WS_2 as channel layers of FETs. A novel strategy to improve the photo detectivity of MoS_2, sensitization of MoS_2-based phototransistor by colloidal quantum wells is presented in Chapter 7. The thesis conclusion and future directions are parts of Chapter 8.

2. STATE OF THE ART

2.1. Introduction

2D material means a material which has a thickness which varies from one atomic thickness to about 10 nm. After discovery of graphene and realizing its gapless nature, researchers have intensively sought after new 2D materials beyond graphene. These investigations have been done through experimental and computational calculation efforts. They have prepared and analyzed 2D materials experimentally and estimated the possible candidates of 2D materials by thermodynamic stability and electronic band structures calculations. Mounet et al. identified easily or potentially exfoliable 1825 2D material candidates in addition to hundreds of experimentally studied ones [19, 20]. The electronic properties of these 2D materials spans all types of materials from metals to insulators.

Herein, a brief literature review on the growth, electronic properties and applications of graphene, MoS_2 and WS_2 is given in the following subsections.

2.2.Production methods of 2D Materials

The production of large area, high quality, monolayers of 2D materials (apart from graphene) remains a challenge. There are two main approaches on production of 2D materials. These are top-down and bottom-up approaches. The top-down strategy is based on producing the 2D materials from their bulk counterpart by using mechanical or liquid exfoliation, while bottom-up approach relies on growing the monolayers via vapor deposition in a sealed chamber (or similar approaches). In this section, the state-of-the-art production methods are introduced briefly.

2.2.1. Mechanical Exfoliation

Graphene was first produced by using adhesive tape, it was peeled off from layered graphite as a layer of honey-comb structured carbon atoms using tape [7]. This method was named as mechanical exfoliation and applied to produce other 2D materials beyond graphene such as $NbSe_2$ [21], MoS_2 [22], and WS_2 [23]. The most important drawback of this technique is the size of produced monolayer flakes which is in the order of 20 μm [24]. In addition to the small flake size, the conventional mechanical exfoliation method results adhesive residue on produced material due to used sticky tapes. On the other hand,

the flakes produced by mechanical exfoliation method demonstrates a less defective nature with respect to CVD grown structures[25]. So that the mechanical exfoliation method is commonly being used for proof of concept studies and applications for a novel 2D materials of in its first steps.

2.2.2. Liquid Exfoliation

Liquid exfoliation is a similar technique to mechanical exfoliation but it is capable of producing large number of samples. The method involves the dispersion of the powder of layered bulk materials in a liquid medium and applying an external force (like ultrasound) and centrifugation [26]. The final 2D nanosheets are dispersed in the solution which can be used as material coating, ingredient of a composite (hybrid) material. Monolayer production yield of this method is very low due to high Van der Waals (vdWs) bonding forces between the crystal layers, so that it is important to use a proper solution with higher surface energies to overcome vdWs forces. Another solution to overcome vdWs forces is using ions inside solution to intercalate between layers of the crystals and reduce the bonding energy[26]. As an intercalation ion, Lithium is commonly being used in several ways such as using Li foil as anode material in electrochemical exfoliation setup where TMD crystal is used as cathode[22, 27, 28]. Liquid exfoliation method is promising for solution-based applications such as printable electronics; however, it still needs to be further optimized.

2.2.3. Chemical Vapor Deposition (CVD)

The bottom-up approach on production of the 2D materials relies on gas phase growth from their solid or gas precursors. This method is also known as chemical vapor deposition (CVD). The mechanical exfoliation may produce high quality monolayers, but it is not suitable for large area production. The high yield production of liquid exfoliation method has some important limitations in its solution-based nature such as small flake size, not applicable to different applications and non-uniform thickness distribution. Hence, CVD method is more advantageous than top-down approaches with respect large area production ability, repeatability and relatively low production costs. All 2D materials used within this dissertation are grown by CVD, the detailed growth procedures of this materials will be described in related chapters. The growth of each 2D material by CVD differs with respect to precursor material, growth temperature, growth pressure, carrier gas type and flow rate and many other parameters. Therefore, CVD growth of each 2D

materials needs to be examined individually. Hence the literature is individually examined in order to understand the effect of process parameters on the quality and size of each specific 2D material namely, Graphene, MoS_2 and WS_2.

2.2.3.1. Graphene Growth by CVD

The growth of graphene by CVD process relies on two basic mechanisms. The first one is the growth on a catalytic metal surface in which the process starts by adsorption of hydrocarbon precursors (commonly methane) on to the growth surface, then follows by the decomposition and surface diffusion of precursor with the aid of catalytic surface and finally finishes by the surface reactions to form graphene [29, 30]. The second one is the catalytic growth of graphene, so-called segregation in which the diffused hydrocarbon precursors (commonly methane) within a heat/liquid substrate start to segregate to the surface during cooling step and form graphene layer [31-33].

The CVD growth of graphene has started by the first few-layer graphene growth on nickel sheet in 2006 after the mechanical exfoliation of it [34]. After that graphene growth by CVD has been investigated and reviewed excessively, for instance CVD growth mechanisms[35, 36] and growth of large area uniformly-monolayer single crystal graphene[37] are just two important aspects of these studies. Nevertheless large-area, high quality growth of graphene is of important for the transition from laboratory to industry. Therefore, large area monolayer/few-layer graphene growth by CVD has been reported on several substrates such as Cu [32, 33], Pt [38], Ni [29, 30, 39], SiC [40], Pd [31], PMMA/Cu/SiO_2/Si [41] and for different CVD configurations such as atmospheric-pressure CVD (APCVD), low-pressure CVD (LPCVD), and ultrahigh-vacuum CVD (UHVCVD) [42]. In addition to that Hesjedal *et al.* reported a continuous 1m long graphene growth on Cu foil with a novel methodology called roll to roll APCVD (R2R APCVD) which is a big step for large area continuous growth [43]. Later on, Deng *et al.* reported on a similar achievement on graphene growth with the size up to 5 cm x 5 m continuous graphene film on Cu foil by using R2R LPCVD method [44]. As a result of all these large area, high quality uniform monolayer growth of graphene, graphene has started to being used in commercial applications, for instance Huawei which is one the largest electronics company started to use graphene as a heat sink in their mobile phone (Mate 20).

2.2.3.2. MoS_2 and WS_2 growth by CVD

TMDs such as MoS_2 and WS_2 have also been grown by CVD method. The CVD growth of TMDs differs from graphene growth in many aspects but the most important difference is the type of the precursors used for the growth. In order to grow TMDs, solid precursors are commonly being used instead of gaseous precursors. The usage of solid precursor brings big challenges on large are, uniform growth of TMDs such as non-uniform vapor pressure trough growth chamber, absence of self-limiting growth mechanism, non-uniform shape and distribution of grown structures, different melting points of solid precursors, non-controllable evaporation of the precursors and sensitive growth to environmental conditions. To overcome these challenges, tremendous efforts has been endeavored in literature. The reported solutions and method can be categorized in three classes; Thermal Vapor Sulfurization (TVS), Thermal Vapor Deposition (TVD) and some innovative additions to these techniques to obtain large area growth and larger flake size.

Thermal vapor sulfurization is a two-step method that involves the deposition of transition metal precursor material on to the substrate and annealing of that material under sulfur rich atmosphere to transform it into the TMD layers. The term “Sulphur rich” can be extended for other chalcogenide atoms (Se, Te) to have different TMDs and their alloys. The deposition of metal precursor on to the growth substrate has utilized in different ways. Some reported studied on transition metal deposition can be listed as follow; Spin and Dip Coating of $(NH_4)_2MoS_2$ [45-47], Electron Beam Evaporation of Molybdenum [48], Thermal Evaporation of MoO_3 [49], Atomic Layer Deposition of MoO_3 [50], Thermal Evaporation of MoO_2 [51] and plasma assisted sublimation process of WO_3 [52]. After the deposition of metal or metal oxide films on to growth substrate, it is sulfurized under certain temperature and atmospheres [53]. Like the other growth techniques TVS has some advantageous and disadvantageous. For instance, there is no limitation on growth coveage. However, low crystallinity and small grain size are the two important disadvantages of the method. Applying post-treatments to increase grain sizes and crystallinity by sintering (like heating in an inert athmosphere)(approximately 100 nm) is a possible solution [49]. But still the treated films will be polycrystalline and the physical properties after treatment such as carrier mobility, electron-phonon scattering will be adversely affected.

The second growth strategy is the thermal vapor deposition where the vaporized precursor materials (S and MoO_3 for MoS_2 and S and WoO_3 for WS_2) are transported on to substrate and the reaction of source materials results the final 2D crystals. During this thesis, this strategy has been adopted and optimized. Even if these method results higher quality flakes with respect to TVS method, it has some challenges which have been mentioned in the first paragraph of this section. Hence the MoS_2 growth related literature is basically focused on to solve the mentioned problems. There are excellent review studies that summarizes the state of the art on different precursor materials, their amounts, carrier gaseous and their flow rates and growth pressures including physical properties [54-56].

The synthesis of graphene on the molten metallic substrate allows hexagonal grains to assembled in a highly aligned manner[57], thus inspiring the exploration of other molten substrates as different approach to thermal vapor deposition strategy. Molten glass offers a low-defective and isotropic surface with a low nucleation density allowing for deposition of large crystalline domains [58]. Apart from the afore mentioned, soda lime glass contains Na^+ ions, known to catalyze the growth of large sized and oriented monolayer TMDCs flakes [59, 60]. Chen *et al.* have manage to grow triangular monolayer MoSe2 crystals with sizes reaching approximately 2.5 mm in 5 min which is one the final big achivements in the TMDs growth related literature [61].

2.3. Electronic Properties of 2D Materials

Having atomic thickness, different electronic band structures (Metal, Insulator and Semiconductor) and easily heterostructure forming ability make 2D materials promising materials for more compact and applicable electronic device structures. Furthermore, theoretical simulations suggest that 2D semiconductors-based device channels could able to shrink the transistors more for smaller IC circuits due to not exhibiting short channel effects [62, 63]. So that it is important to mention the related literature about the electronic properties of 2D materials. Herein, a brief literature review and basic properties of 2D materials is given.

2.3.1. Graphene

Graphene is the first and most widely studied 2D material because of its unique and superior electronic and physical properties such as; a carrier mobility of $2{:}5 \times 10^5 cm^2 V^-$

$^{1}s^{-1}$ [64] at room temperature, a mechanical strength of 130*GP* [65], a thermal conductivity of 300 WmK^{-1} [66] and an optical absorption of $\pi a \approx 2{:}3\%$.

Graphene contains *sp*2-hybridized carbon-atoms with honeycomb packing. The three of four valence electrons of carbon-atom bond each other with the strong in-plane covalent bonds, and the remained fourth one stays in the *p* orbital and makes the out-of-plane π bonds which are able to be effortlessly delocalized among the atoms, results with exceptional linearly dispersed band structure of graphene as shown in Figure 2.1 [67].

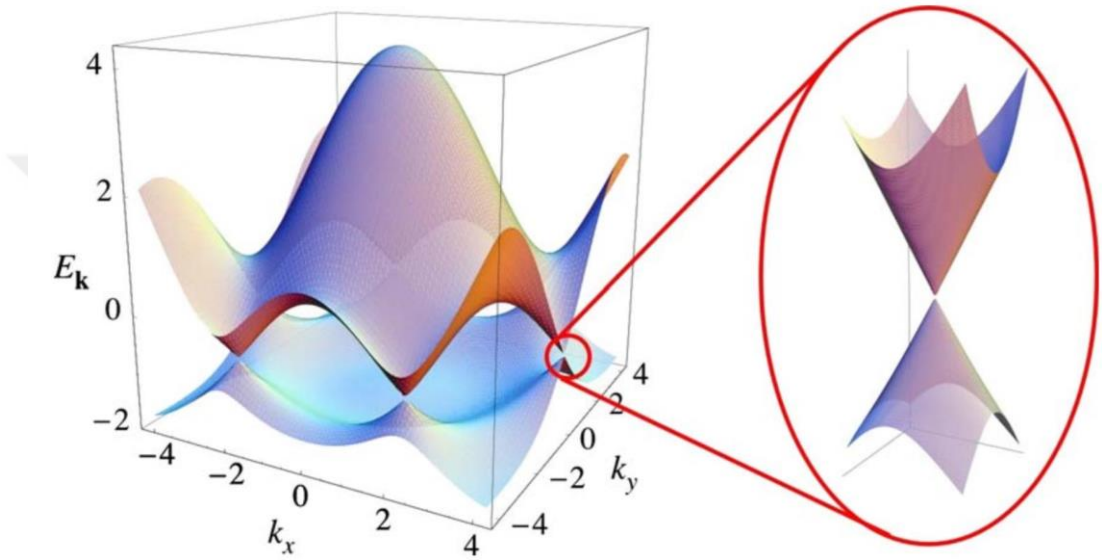

Figure 2.1 *Linearly dispersed electronic band structure of Graphene. The inset shows the Dirac cone where valance band and conduction band touch each other. Adopted from ref [67].*

The gapless nature which is a result of linear energy dispersion, open a new route for opening a finite band gap by constraining the graphene in one dimension to split the energy dispersion of graphene into multiple 1D modes. Han *et al.* demonstrated the first experimental prove of this idea and managed to open a bang gap of ~400 meV for nanoribbons with a width of less than 15 nm [68]. Later on, the importance of edge geometry of nanoribbons on the device stability has been understood after various graphene nanoribbons-based (GNR) studies [69-71]. The disordered edge termination of the nanoribbons (armchair, zigzag or combination of these two terminations) results ambiguity in device performances [72]. Band engineering efforts on graphene and GNRs are still being studied in literature for more promising devices. The origin of these efforts are coming from the ballistic carrier transport property of graphene[72]. In other words, the measured and estimated carrier mobilities of graphene are enormously high values which are reported as $10^4\,cm^2V^{-1}s^{-1}$ and $2.5x10^5\,cm^2V^{-1}s^{-1}$, consequently. These extremely

high carrier mobilities are the result of very small effective charge masses which comes from the second derivative of linear energy dispersion of graphene [73]. In addition to that it has been reported that the encapsulation of graphene by h-BN enhanced the mobility of graphene to $5x10^5$ $cm^2V^{-1}s^{-1}$ due to lowering the trap states and impurities [64, 74].

2.3.2. Transition Metal Dichalcogenides

Gapless nature of the graphene and the unexpected superior properties that comes from isolation of one single layer have pushed researchers to search for new 2D materials for electronic and optoelectronic applications. After these search endeavors, 2D transition metal dichalcogenides family has become prominent with its 39 members (excluding alloy systems) as new promising materials for electronic and optoelectronic applications.

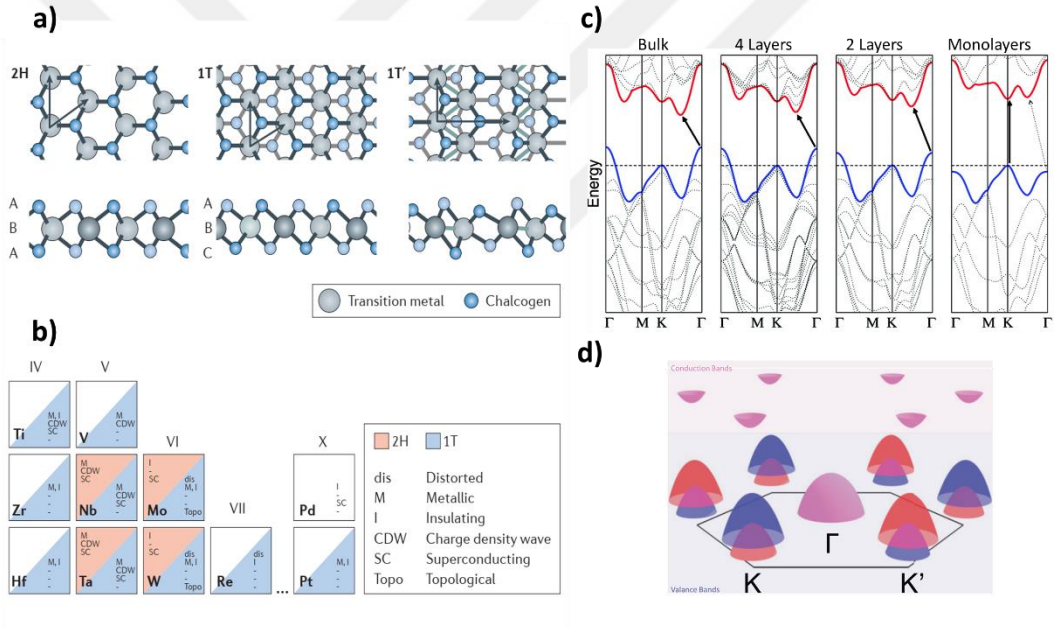

Figure 2.2 *a) Atomic structure and three different phases of single later TMDs which are trigonal prismatic (2H), octahedral (1T) and dimerized (1T'). Lattice vectors and atomic planes are indicated. b) Periodic table section of transition metals with electronic and structural properties. c) Layer dependent band-structure of 2H-MoS_2. d) Figurative representation of band structure of 2H-MoS2 with band splitting at high symmetry points: K and K'. a and b adopted from ref [75], c adopted from ref [76] and d adopted from [77].*

MoS_2, WS_2, $MoSe_2$ and WSe_2 are the most important and widely studied members of TMDs family due to their interesting electronic and optical properties. TMDs are being formulated as MX2 in where M refers to transition metals (Ti, Zr, Hf, V, Nb, Ta, Mo, W, Tc, Pd, Pt and Re) having a + 4 valency and X refers to chalcogenides (S, Se and Te) having a valency of -2 (Figure 2.2b) [78]. TMDs form as sandwiched metal atom between

two layers of chalcogen atoms in a hexagonally packed structures (as shown in Figure 2.2a)[79]. They are typically existing in two different coordination system which are trigonal prismatic (D_{3h}) and octahedral (D_{3d}). These two systems are acting as unit blocks which forms three different TMDs phases: 2H, 1T and 1T' as demonstrated in Figure 2.2a. These phases could exist in ABC or ABA stacking order where A and C stand for chalcogen atoms and B refers to transition metals (Figure 2.2a). 2H phase of TMDs (specifically MoS_2 and WS_2) is leading in nature and more stable than 1T and 1T'. 1T phase (octahedral system) is absence in nature and needs to be synthesized by Li intercalation or oxidation of potassium thiomolybdate [80, 81]. Furthermore, 1T phase is metastable and in tendency to transform 2H phase by heating or aging [22, 54]. The phase transformation from 1T to 2H also transforms the electronic structure of TMDs from metallic state to semiconductor state[81].

Single layer of TMDs materials are expected have no dangling bonds on their surfaces due to chalcogenides termination and lone-pair electrons in ideal case [82, 83]. Hence the surface stability of TMDs are expected to be robust against impurities or environmental species. This property of TMDs is superior for stable and high-performance electronic applications due to dangling-bond-free surface lowers the number of trap states [78]. However, CVD grown or exfoliated (Mechanical or Liquid) samples contains structural defects (such as S-vacancy) due to the equilibrium and the kinetics of processing [84].

Another and one of the most important properties of 2D TMDs is their indirect to direct band-gap transition after isolation of one single layer from their bulk counterparts. Since the electronic and optical properties of any material depends on the electronic band structure of it, these band gap transition transforms these materials from to be a lubrication [85] material to a promising channel material candidate for future electronic and optoelectronics [86]. The band gap transition while the dimension reduction from bulk to monolayer is not only changing the indirect to direct bandgap but also the gap width of related TMDs, for instance from 1T-MoS_2 to 2H MoS_2 transition changes the band gap from ~1.2 eV to ~1.9 eV which is depicted in Figure 2.2c. As another example of band gap width change is could be the band gap transition of WS_2 which changes from 0.9 eV to 2.0 eV [87]. In Figure 2.2d, figurative representation of band structure of 2H-MoS_2 with band splitting at high symmetry points: K and K' which is due to the strong Spin-Orbit coupling [88]. This split band structure of 2H-MoS_2 makes it proper for quantum information processing and spin electronics [89]. This layer dependent electronic

structure is the origin of transparency and high quantum yield properties of TMDs (specifically MoS_2 and WS_2).

One of the most important and promising properties of TMDs is this enlarged and direct bandgap which attracted researchers to adopt these materials to electronic and optoelectronic applications, more specifically FETs or phototransistors. The conditions of being a proper material for electronic and optoelectronic applications can be listed as follows [3];

- Proper Bandgap (E_g) (E_g application dependent but mainly between 1.1 to 2.5 eV),
- High Carrier Mobility and Velocity with Low Effective Masses (for fast devices),
- Large current ON/OFF ratio (To have low stand-by power consumption),
- High Thermal Conductivity (To have cooler devices for high performance),
- Low Contact Resistance,
- Absence of Short-Channel Effects (To have smaller devices).

One of the important parameters in the list above is the high carrier mobility which depends on several parameters. Especially, the mobility of TMDs and other 2D materials are delicate to several parameters such as, number of layers, charged impurities, localized trap states, carrier polarity, contacts, substrate, defects and device geometry [78]. Due to these various parameters, the reported mobility values of MoS_2 and WS_2 based devices span a wide range from 0.003 to 200 $cm^2V^{-1}s^{-1}$ [10, 90]. In addition to mobility, the charge polarity of TMDs is not same for all members. For instance, MoS_2 and WS_2 has a n-type character which is due to sulfur defects and substrate screening effects [91, 92].

2.4. Device Applications of 2D Materials (Graphene, MoS_2 and WS_2)

2.4.1. FETs Figures of Merit

MOSFETs is are one the most widely used unit blocks of electronic devices in digital integrated circuits as mentioned in the first chapter. In digital electronics a MOSFET functions as a switch which controls the conductivity of semiconductor channel between source and drain terminals by utilizing gate terminal voltage. In Figure 2.3a the schematic representation of a typical MOSFET cross-section is shown. A conventional n-channel MOSFET consists of source and drain electrodes which are deposited on n-type Si areas

on p-type Si substrate and gate electrode which is deposited on insulating gate-oxide (Figure 2.3a).

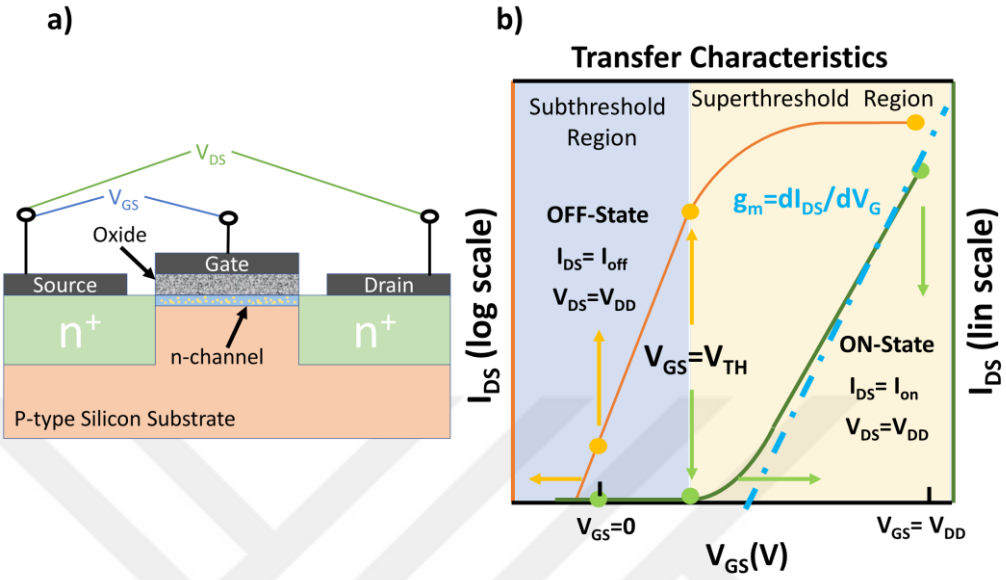

Figure 2.3 *a) Cross-section of an n-channel Si MOSFET and b) a typical transfer characteristic (Drain current vs gate voltage) of a MOSFET.*

Under a positive gate bias (V_{GS}), electrons within the semiconducting channel are attracted by the gate voltage and forming an inversion layer which lets charge transport through the channel, between source and drain voltage. The point where the inversion layer connects the source and the drain is called as the threshold voltage (V_{TH}). MOSFETS should have no current flow for gate voltages smaller than V_{TH} (OFF-state) and have no resistance for gate voltages higher than V_{TH} (ON-state) in the ideal case (Figure 2.3b). Besides, OFF to ON or ON to OFF state transition should occur within a single gate voltage step. Hence, the ratio of maximum ON-state current to minimum OFF-state current is regarded as the maximum current modulation factor for real MOSFETs as a figure of merit. In figure 2.3b a typical transfer characteristic of a conventional MOSFET is given. Here, the drain-source current data is plotted in logarithmic (orange curve) and linear (green curve) scale as function of gate voltage. The inverse of the slope of the I_{DS} current in logarithmic scale is referred as subthreshold swing (SS) value, given in units (mV/decade). Furthermore, the slope of I_{DS} current in linear scale is called as transconductance (g_m) which is used to estimate the field effective mobility (μ_{FE}), given in units of ($cm^2V^{-1}s^{-1}$) [3].

2.4.2. 2D Materials Based Field Effect Transistors

2.4.2.1. Graphene based FETs

Thus far, there has been tremendous research on graphene-based FETs. The state of the art on graphene based FETS are indexed in several detailed review papers from different perspectives [69, 93-95]. It is not possible to cite the large number of published papers in this dissertation, so that the main challenges and latest progress of graphene in electronic applications will summarized below.

The I_{ON}/I_{OFF} ratio (switching off rate) of graphene-based FETs are in the order of 10^0 to 10^1 which is not adequate for digital electronic applications. The low switch off rates of graphene that comes from gapless nature of it, has been tried to overcome by fabricating GNRs to open a band gap. GNR-based FETs with back gate configurations manage to achieve I_{ON}/I_{OFF} ratios from 10^4 to 10^5 [96-98]. Graphene, GNR or TMD based transistors are generally driven by a large gate voltage swings of 3-50 V for switching due to thick gate dielectric layers. However, the supply voltage of the commercial logic circuits is below 1V, and will decrease further for future circuits [3]. Hence, GNR based FETs with very thin dielectric layer (top or back gate structures) are required for lower gate voltage swing rates (sub-1V). Besides, GNR formation from graphene layers causes a dramatic degradation of carrier mobility [71]. These are main challenges in the literature up to now.

Another proposed solution to switching problem of graphene is vertical non-FET transistor architectures. The main idea of these concepts is either fabricating graphene-Si Schottky barriers or applying graphene into hot electron transistor as the base layer [99, 100]. The I_{ON}/I_{OFF} ratios up to10^5 have been reported from devices using that concepts [99].

2.4.2.2. TMDs (MoS_2 and WS_2) Based FETs

After the awareness of gapless nature of graphene, 2D semiconductor TMDs draw attention in electronic application due to their practical application as channel material in field effect transistors (FETs). In addition to their wide bandgap; due to their thermal stability and robust surface against chemical modifications due to dangling bond free nature, they have become the most significant candidates for future electronics. As mentioned before, there have been various studies to optimize the performance of 2D TMDs based devices in terms of carrier mobility, I_{ON}/I_{OFF} ratio, contact resistance, gate

and device architecture, *etc.* In the following, a brief review on these performance optimization attempts is given.

In 2011, an exfoliated monolayer flake of MoS_2 used as channel material in a metal oxide field effect transistor (MOSFET) for the first time which is also the first example of 2D TMDs based transistor applications [10]. The I_{ON}/I_{OFF} ratio of this device was reported as 10^8 for gate sweep range of 4 V which was a promising performance. After this epitomic study, other groups started to fabricate FETs based on different TMDs with different thickness from single layer to multilayer [91, 101-103]. In addition to reports on single device there has been attempts on fabricating MoS_2 based complex circuits such as microprocessors, logic gates *etc.* [104, 105].

The carrier mobility of TMDs based device is the first characteristic that have started to optimize for overall performance enhancement of fabricated devices. The mobility is limited by disorder and scattering centers which can trap or scatter the charges. Besides, the optical phonons in the environment of 2D material also have a significant effect on the mobility at room temperature (RT) [75]. The predicted mobility of MoS_2 by calculations is in a range of 10-1000 $cm^2V^{-1}s^{-1}$ for RT and ~10^5 at low temperatures which is highly related to the defect density and dielectric environment [106-108]. The experimental results demonstrate almost two orders of magnitude lower mobilities than the predicted values [10, 21, 109]. The reason of these performance degradation is considered to be their environmental sensitive nature due to high surface-to-volume ratio. It was found that encapsulation and/or an efficient gate dielectric architecture can increase the mobility by decreasing the environmental effects and increasing dielectric modulation efficiency [10, 108-111]. Similar effort has been spent for WS_2 also and mobility increase (for instance, a carrier mobility of 214 $cm^2V^{-1}s^{-1}$ is achieved for h-BN/WS_2/h-BN structure [112]) has been achieved [112-114].

The contact resistance is another important subject that has been investigated in many studies, since the Schottky barrier existence at metal-semiconductor interface decrease the off-state and charge injection performance of 2D based devices. The presence of non-ohmic (Schottky) barrier has been reported by several studies [115-117]. The origin of this barrier is assumed to be Fermi Level Pinning (FLP) effect at metal-semiconductor junction which is assumed to be due to high density of defects and impurities such as S-vacancies [118-122].

Das *et al.* reported on the effect of different metal contacts on carrier transport properties of multilayer MoS_2 [116]. They used both low and high work function metals including Ti, Pt, Ni and Sc to observe the p-type behavior for high work function metals and n-type behavior for low work function ones. However, the fabricated multilayer MoS_2 based devices with all four metals showed n-type characteristics which explained by FLP mechanism. They extracted the SBH for Pt, Ni, Ti and Sc as 230, 150, 50 and 30 meV correspondingly and the effective carrier mobilities as 21, 36, 125 and 184 $cm^2V^{-1}s^{-1}$ respectively [116]. The findings of mentioned study and several other studies proves the importance of contact formation due to its effect on effective performance of the devices.

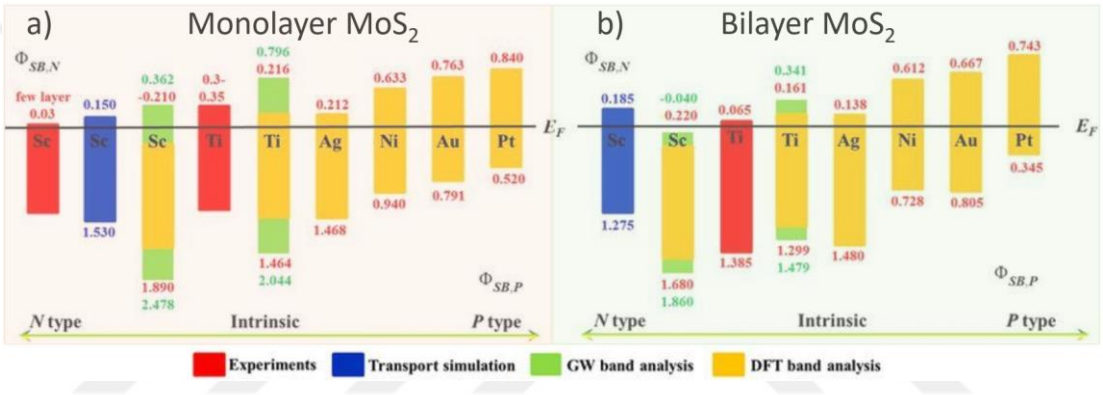

Figure 2.4 *Schottky Barrier Heights (SBH) of (a) Monolayer and (b) Bilayer MoS_2 on the six metal surfaces. $\Phi_{SB,N}$ refers to n-type for SBH electrons and $\Phi_{SB,P}$ denotes p-type SBH for holes. Adopted from ref [123].*

In Figure 2.3, the calculated and experimentally estimated SBH of monolayer (ML) and bilayer (BL) MoS_2 with respect fermi level alignment which is reported by Zhong *et al.* are shown. The lowest SBH was achieved for ML and BL MoS2 by Sc contacts in both experiments and theoretical calculations [123]. Even if the metals with large work function (Pt) are expected to show a p-type characteristic, the results of experimental studies (as mentioned above) are inconsistent with the estimated results of Figure 2.3.

In addition to the efforts on contact resistance optimization for the sake of mobility enhancement, the influence of the channel surrounding is another important issue that needs be handled and effects mobility and device stability. The effect of channel encapsulation and high- κ dielectric layer has been mentioned at beginning of this section [10, 108, 109]. In Figure 2.4, two examples of encapsulation engineering related mobility enhancement are shown. In Figure 2.4a and 2.4b the effect of encapsulation by HfO_2 and top gate on the temperature dependent mobility results are demonstrated [110]. Before

applying HfO_2, the bare back-gated MoS_2 transistor, the mobility increases with respect to increasing temperature until the temperature ranges to 200 K then it starts to decrease which indicates the dominant mobility limiting mechanism is charge scattering before T~ 200 K and after T~ 200 K the phonon scattering turns to be dominant mechanism. Furthermore, the maximum mobility is between 10-20 $cm^2V^{-1}s^{-1}$ around T~ 200 K [110]. After encapsulating the same device with high- κ dielectric constant HfO_2, decrease the Coulomb scattering from charged impurities that results in an increased low temperature mobility which is between 100-200 $cm^2V^{-1}s^{-1}$ around T~ 200 K. Hence the mobility behavior with respect to temperature is also changed in which the mobility starts to degrade with increased temperature that indicates the dominant effect of phonon scattering[110].

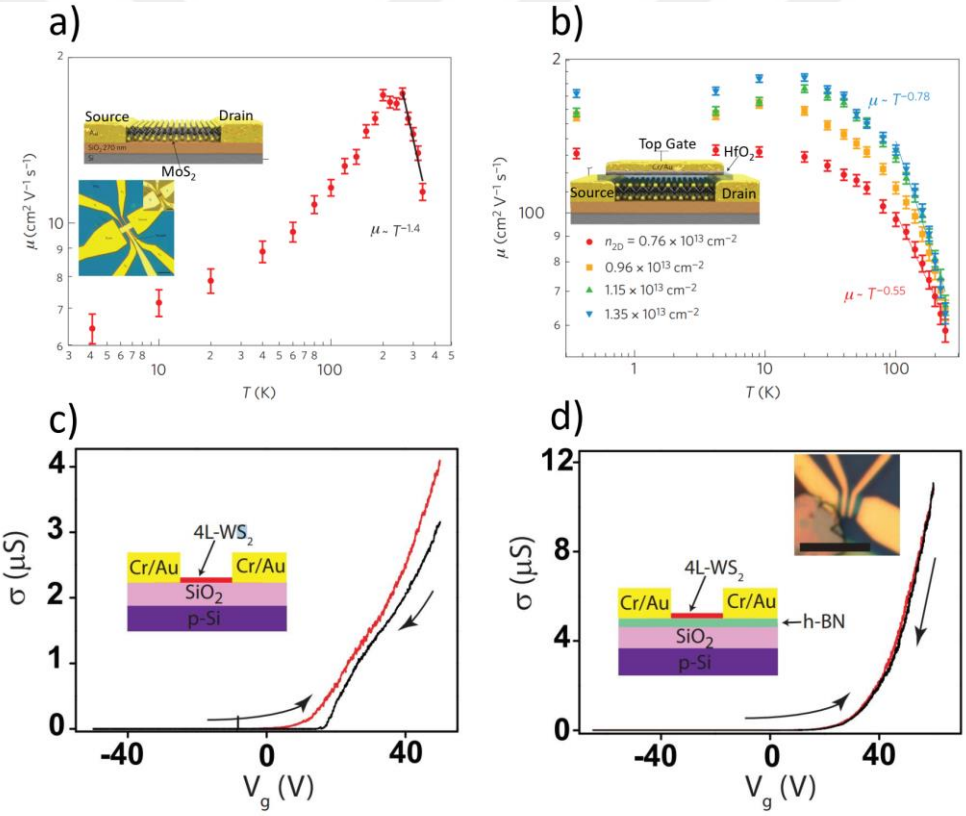

Figure 2.5 *The temperature dependent mobility of ML MoS_2 based transistors with (a) bare and (b) encapsulated channel in HfO_2 and with a top gate (The same transistor is encapsulated; the insets show the schematic diagrams of device structures). The conductance of 4-layer WS_2 based transistor (c) with and (d) without h-BN dielectric environment (The insets show the schematic diagrams of device structures).* ***a*** *and* ***b*** *adopted from ref [110].* ***c*** *and* ***d*** *adopted from ref [124].*

In Figure 2.4c and 2.4d, the back gate dielectric layer dependent conductivity results of 4-layer (4L) WS_2 transistor is demonstrated. The transistor with bare SiO_2 dielectric layer shows a smaller conductivity with large hysteresis behavior which due to trap states

at the interface of 2D semiconductor- dielectric layer [124]. However, applying a h-BN layer on the top of the SiO_2 under 4L-WS_2 suppressed the large hysteresis behavior and increased the maximum saturation current within the same gate voltage swing that result in an increased field effective mobility [124]. There has been several other studies that reporting the similar effect of PMMA encapsulation on the enhanced carrier mobility [125].

2.4.3. Photodetectors/Phototransistors

The photodetection or photo-sensing with high responsivity and low dark current is essential for numerous applications such as imaging, spectroscopy and communication etc. Basically, the photodetection is converting light into measurable electrical current or voltage signals. Graphene and 2D materials beyond graphene are the new attractive material family for optical detection and sensing application due to their high responsivities, low dark currents, direct band gaps (except from Dirac materials) applicability to a wide range of wavelengths and their modular structures makes them proper for purpose-specific design ability [126]. Even if, graphene doesn't have a gap, the unique band structure of it (linear dispersion), make possible to tune the working spectrum window of it by using electronic doping (electrical gating) to modulate the fermi level. Hence, graphene-based photodetectors/phototransistors have wide range of application from infrared to THz [126, 127]. On the other graphene-based photodetectors, suffers from high dark currents due to its gapless nature. The direct band gap of 2D semiconductor TMDs which ranges from 1 eV to 2.3 eV, cover the spectrum from infrared to visible light detection. Besides, the photodetectors based on this material family shows low dark currents and high responsivity performances compared to graphene based-ones.

The principal of the photodetection is to generate illumination dependent-photocurrent mechanisms which can be classified into three classes: photovoltaic effect, photo-thermoelectric effect and bolometric effect. The photovoltaic effect (Photogating effect, photoelectric effect or photoconductivity effect) is the harvesting the photo-excited electron-hole pairs by an electric field which could be a built-in (p-n junction [128, 129], TMD-metal barrier- SBH) [130] or external (Electrical gating) [131, 132]. The photo-

thermoelectric effect is the accumulation of the carries on the cold side of a temperature gradient which occurs by nonuniform illumination heating.

In 2D materials-based photodetectors the dominant photocurrent generation mechanism is photovoltaic effect. Herein, a summary of graphene and TMDs based photodetector application are given below in two subsections.

2.4.3.1. Graphene-Based Phototransistors

The fermi level modulation ability of graphene in several ways, make it desirable for a wide range of application with a large spectral range. The fermi level modulation can be done by band bending at metal contact graphene interface and the carrier injection (108). With aid of these unique property of graphene, Xia *et al.* manage to fabricate an ultra-fast phototransistor based on few- and single layer graphene which has a bandwidth of 40 GHz. They estimated that graphene photodetectors could exceeds a bandwidth 500 GHz [127]. The main drawback of their design was the low photoresponsivity of fabricated devices (the relative photoresponsivity with respect to light intensity modulation frequency and gate voltage dependent photoresponsivity is depicted in Figure 2.5a) which in the order of 0.5 mAW^{-1} [127]. To overcome the low responsivity problem of graphene-based photodetectors, gate modulation approach has been applied to graphene active channel by *Guo et al.* [133].

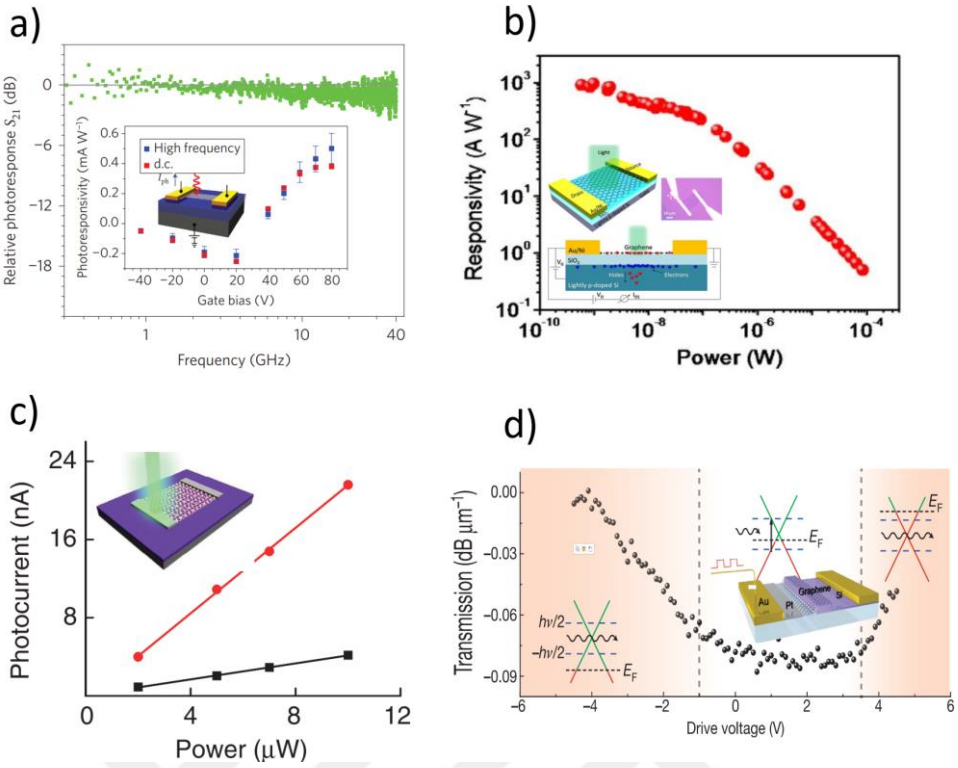

Figure 2.6 a) *Relative alternative current photo response $S_{21}(f)$ of ultrafast graphene photodetector as a function illumination intensity modulation up to 40 GHz with a gate bias of 80 V. The first inset is direct current and alternative current photoresponsivity as function of gate voltage and the second inset is the schematic representation of graphene photodetector. b) The responsivity of high-performance graphene photodetector as function of illumination power at V_{DS}= 1 V and V_{GS}= 0 V. The inset shows the schematic representation and optical image of the fabricated graphene photodetector on lightly p-doped SiO_2/Si substrate. c) The photocurrent vs illumination power characteristics of the plasmon resonance enhanced graphene photodetectors. The red and black lines indicate the response of a typical device with and without Au nanoparticles, respectively. $\lambda_{Excitation}$:514 nm. The inset shows the schematic representation of device. d) Electro-optical response of graphene-based broadband optical modulator for different drive voltages with band alignment schematics. The inset shows the schematic representation of device. a, b, c and d adopted from ref [127], ref [133], ref [134] and ref [135], respectively.*

A graphene/SiO_2/Si heterostructure was formed to harvest the light-induced electron-hole pairs in silicon by a built-in electric field at SiO_2/Si interface and migration of charges to graphene/gate interface. In figure 2.5b the very high photoresponsivity of this hybrid device with respect to illumination power which exceeds ~10^3 AW^{-1} is demonstrated [133].

Plasmonic structures are proved to be beneficial for performance enhancement in graphene photodetectors [136-138]. The localized electrical field around the plasmonic metal structures plays a significant role in improving the generation, separation and conduction of photo-induced quasi particles. Hence, these structures improve the photoresponsivity and also enables the selective multicolor spectral response of the photodetectors [134]. As an example of this concept, the efficient coating of gold nano

particles on the surface graphene channel of a photodetector, achieved an external quantum efficiency of 1500% and allowed to select detection color. In figure 2.5c the effect of ensemble of plasmonic gold nanoparticles on the photocurrent is depicted in which a clear enhancement of photocurrent is visible [134].

Another area of getting benefits from the light interaction of graphene is silicon waveguide-based optoelectronic applications. The main bottleneck of silicon-based optoelectronics is the indirect band gap of silicon which results in weak light interaction. The exceptional photoelectric performance of graphene with its tunable working spectral range and carrier transport characteristic makes it attractive as solution the problems of silicon-based optoelectronic applications. With aid of tunable absorption property of graphene, Liu *et al.* designed an optical graphene modulator [135]. This designed manage to achieve a modulation depth of 0.1 dB μm^{-1} with spectrum range reaching 1.6 μm [135]. The transmission modulation with respect gate voltage and schematic diagram of the device are represented in Figure 2.5d.

The mentioned applications are just some selected studies from different concepts, there numerous graphene based photodetectors which can found from the review paper ref [24].

2.4.3.2. 2D TMDs-Based Phototransistors

The direct wide band gap of TMDs has made this material family attractive for optoelectronics. The direct band gap of 2D semiconductor TMDs which ranges from 1 eV to 2.3 eV, cover the spectrum from infrared to visible light detection. MoS_2, WS_2 and $MoSe_2$ are the most popular member of TMDs family with superior photodetection performances. The first photodetector application of ML exfoliated MoS_2 showed a significant photocurrent generation performance with photoresponsivity of 7.5 mAW^{-1} for $\lambda_{excitation} < 670$ nm [131]. As mentioned before, the main drawbacks of the MoS_2 (or TMDs) are the high contact resistance due to SBH and low back gate modulation efficiencies. Lee *et al.* investigated both top gate and the number of layers effect on the detection performance of MoS_2 based phototransistors [139]. The results showed that increasing the layer number of MoS_2 from monolayer to trilayer, tunes the detection wavelength from green to red light [139]. Another bottleneck of MoS_2 based phototransistors is the temporal response time which is in the order of several seconds.

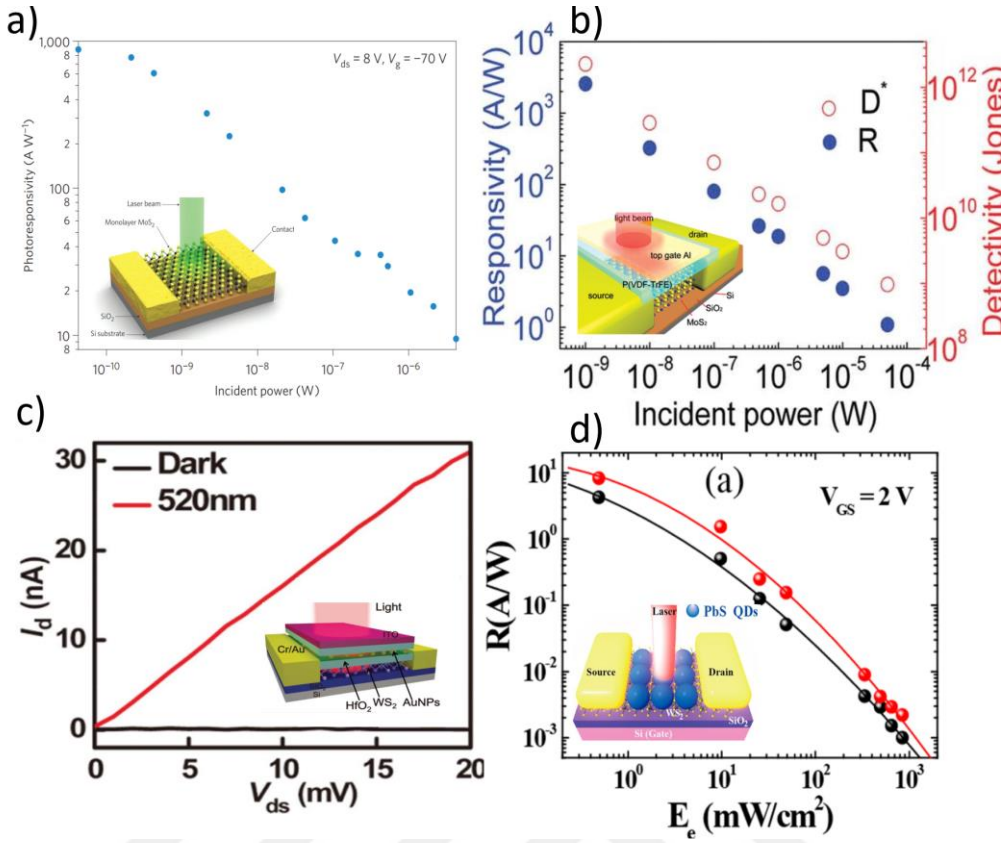

Figure 2.7 *a) The power dependent photoresponsivity of ultrasensitive ML MoS_2 based photodetector which exhibits a photoresponsivity of 880AW^{-1} for an illumination intensity of 24μWcm^{-2}. The inset shows schematic diagram of the device. b) The photoresponsivity and specific detectivity of triple-layer MoS_2 photodetector as a function of incident power. The detector shows a high responsivity and detectivity of 2570 AW^{-1} and 2.2x10^{12} Jones for an illumination power of 1 nW, respectively. The inset shows structure of the device. c) The output characteristic of the floating gate WS_2 phototransistor with and without illumination. The inset shows device architecture. d) The illumination power dependent responsivity of PbS quantum dots sensitized WS_2 photodetectors for drain biases of 0.5V (Black) and 1.5V (red). The inset shows the schematic diagram of the device. a, b, c and d are adopted from ref [140], ref [141], ref [142] and ref [143].*

As solution to this problem a two-pulse photovoltage correlation technique is proposed and a certainly fast response of 3 ps is achieved [141]. Lopez et al. increased the photo response performance of MoS_2 based phototransistor by improving the effective carrier mobility with lower contact resistance [140]. They achieved a photoresponsivity of 880 AW^{-1} (Figure 2.6a). The exfoliated MoS_2 flakes were being used for the first attempt of MoS_2-based photodetector fabrication, the fist CVD grown MoS_2-based photodetector designed by Zhang et al. and manage to reach the photoresponsivity of 2200 and 780 AW^{-1} in vacuum and in air, consequently [144]. This study revealed the effect of atmosphere on the performance of 2D TMDs based devices. Since the effect of dark current on photodetectors seems pretty obvious, suppressing the dark current of TMDs based

photodetectors is another studied topic in literature. In this aspect, poly (vinylidene fluoride–trifluoroethylene) (P(VDF-TrFE)) had been used as dielectric layer in a ferroelectric-regulated phototransistor (Figure 2.6b). The phototransistor with this novel architecture reached a superior photoresponsivity of 2570 AW^{-1} thanks to the its structure which reduces the dark current [141]. In addition to MoS_2 based photodetector designs, WS_2 is another shining candidate as possible channel material for photodetectors. Gong *et al.* used multilayer WS_2 in a floating gate structured phototransistor to suppress the dark current and increasing the devices hysteresis behavior for memory applications [142]. They achieved superior photoresponsivity of 1090 AW^{-1} with a very low bias voltage of 0.02V. The difference between suppressed current and illuminated current is demonstrated in Figure 2.6c [142].

The low absorption coefficient of 2D TMDs is another drawback which is being widely studied by researchers. A possible solution to this is applying a sensitizer layer on top the TMDs material to increase the absorption and also spectral selectivity. Semiconductor colloidal quantum dots are widely used photonic crystals due to their high responsivity, tunable spectral response windows and absorption [145]. As an example of this concept, PbS quantum dots were used as sensitizer layer on top of WS_2 to construct a hybrid phototransistor by Yu et al. in 2017. They achieved comparatively high photoresponsivity of 14 AW^{-1}. The schematic diagram and power dependent responsivity curve are demonstrated in Figure 2.6d [143].

3. EXPERIMENTAL TECHNIQUES

3.1. Introduction

In this chapter, the experiment methods which have been used during this PhD study are introduced and schematic diagrams of the set-ups are demonstrated. The chapter is organized as CVD, the transfer method, optical and physical characterization techniques, fabrication methods namely optical and E-beam lithography, metal coating and lift-off steps and electro-optical characterization and analysis methods.

3.2. CVD Growth of 2D Materials (Graphene, MoS_2 and WS_2)

3.2.1. CVD growth and transfer procedure of Graphene

3.2.1.1. CVD growth of Graphene

The first graphene like growth is the one in 1984 done by Kholin et al. to research the catalytic and thermionic properties of Ir in the carbon atmosphere [146]. However, uniform, single layer and large area graphene was first grown on Cu foil with CVD system by Li et al in 2009. The process occurred with thermal catalytic decomposition of methane on low carbon solubility metal Cu under hydrogen flow [147]. CVD method has become a standard line for graphene growth after study of Li et al. Therefore, we chose the CVD method for graphene growth like in literature.

In this thesis the Graphene growth will be done over ultra-smooth copper foils by thermal CVD system. The CVD system installed in MIDAS research group laboratories has been used for reported works in this dissertation. The schematic drawing of the CVD system is shown in Figure 3.1. The system is consisting of a quartz chamber with 8 cm inner diameter, vacuum control unit that able to control from 1 atm to 1 mbar vacuum levels, three heating zone with different temperature ranges (max 400 °C, max 1100 °C and max 1100 °C) and 4 mass flow controllers for reactant or carrier gas flow control (Figure 1).

The contemplated framework of graphene growth recipes is as follow;

- Set the Cu substrate in the middle of the first zone,
- Vacuum the quartz tube till reach ≈ 5 mtorr or below,
- Set the H_2/Ar flow according to receipt,
- Turn on the first heat zone of furnace (ramp to growth temperature),
- (Annealing of the copper if it is necessary),

- When the growth temperature reached start the CH_4 flow,
- Wait as long as growth duration,
- Stop the CH_4 flow
- Open the furnace lid,
- Wait for the temperature to decrease below 100 °C

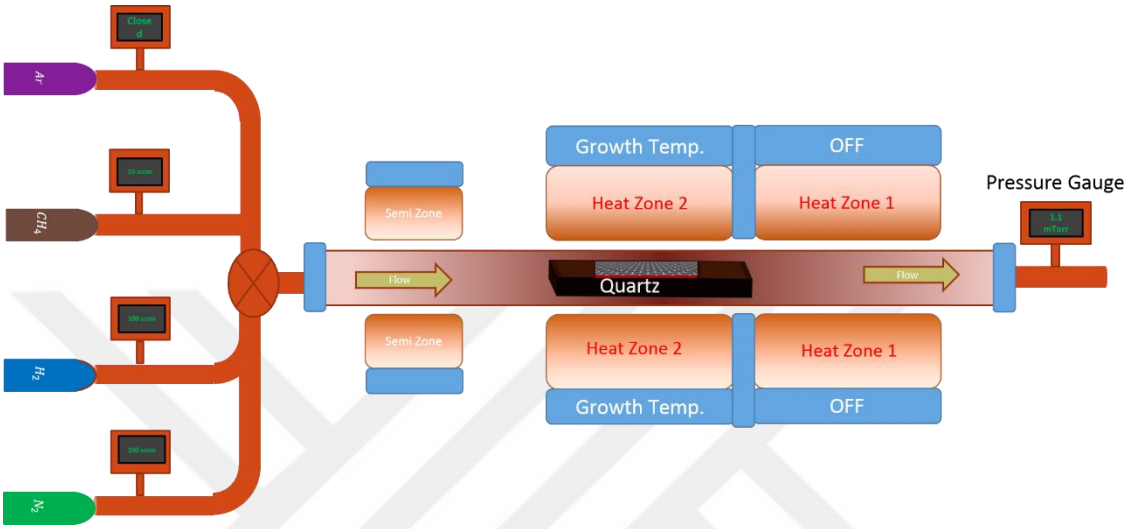

Figure 3.1. *The schematic diagram of the CVD system with all environmental attachments.*

The Cu substrates which shaped in desired geometry, will be heated until growth temperature under H_2 flow to etch the natural oxide layer of the copper foils and make possible CH_4 –Cu interaction for decomposition. After that, the CH_4 flow will be started with planned flow rate to start growth as long as growth duration. During the growth flow of CH_4 and H_2 gases will be set on. Finally, for terminating the growth by stopping the flow of methane and opening the lid, the samples will be cooled down to room temperature under H_2 atmosphere.

3.2.1.2. Transfer procedure of Graphene

The wet transfer procedure for graphene is shown in Figure 3.2. in which the transfer procedure is depicted step by step. The process is starting with pouring photoresist (PR) (S1413) on top of the samples (Graphene/Cu). Then the samples are baked at 70 °C for 12 hours to remove the solvent in photoresist and handle a solid holder for graphene. The sample with hardened PR is left in Iron (III) Chloride ($FeCl_3$) solution to etch Cu substrate. Then the remained (Photoresist/Graphene) are placed on target the substrate. After that the sample (PR/Graphene) on substrate baked at 70 °C (soft bake) for 1 minutes

and baked at 120 °C (Hard Bake) for two more minutes to ensure adhesion of PR/graphene to substrate. As final step the PR is removed by acetone solution and the samples rinsed under acetone, isopropanol alcohol and DI water, respectively.

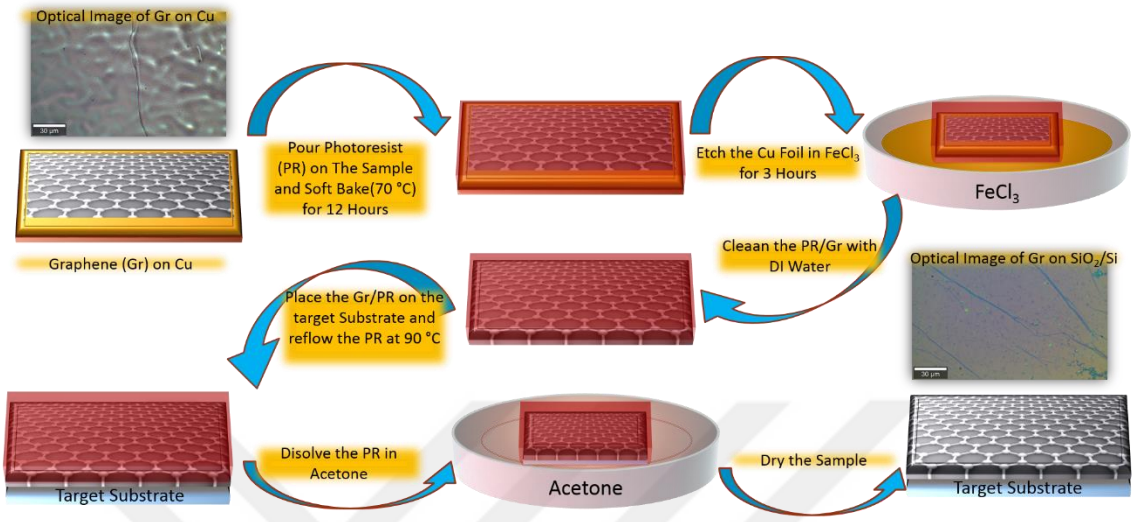

Figure 3.2 *The transfer procedure of the Graphene from as-grown substrate Copper to target substrate.*

3.2.2. CVD growth of TMDs (MoS_2 and WS_2)

3.2.2.1. The CVD growth of TMDs on SiO_2/Si substrate

The CVD growth of 2D MoS_2 and WS_2 flakes is performed in a home-built, dual-zone furnace with a 70 mm diameter horizontal orientation quartz tube operated at atmospheric pressure. The growth zone configuration of the set-up is depicted in Figure 3.3 SiO_2/Si substrate is positioned face-down above the MoO_3 or WO_3 precursors. Quartz boats containing the precursors are placed on the quartz plate and therefore are positioned at the center of the quartz tube. Sulfur is placed at the upstream direction of the furnace having 16 cm distance with the metal-oxide precursors. The precursor amounts are kept constant for both MoS_2 and WS_2 growth processes at values of 150 mg for S and 1 mg for MoO_3 and WO_3, respectively. The growth procedure can be summarized as follows: 1 mg of MoO_3 (Sigma Aldrich, 99.5%) and 150 mg of S (Sigma Aldrich, 99.5%) powders are used as precursors and reacted to form MoS_2 flakes at 700 ºC under 400 sccm N_2 flow. Similar to MoS_2 growth configuration, 1 mg of WO_3 (Sigma Aldrich, 99.5%) and 150 mg of S powders have been used as precursors to form WS_2 flakes at 950 ºC, under 95 sccm N_2 and 5 sccm H_2 on SiO_2/Si substrates. An inner one side-sealed quartz tube (2 cm

diameter) is used to confine or keep WO_3 vapor on the substrate. The distance between Sulphur and oxide precursors is fixed to 16 cm."

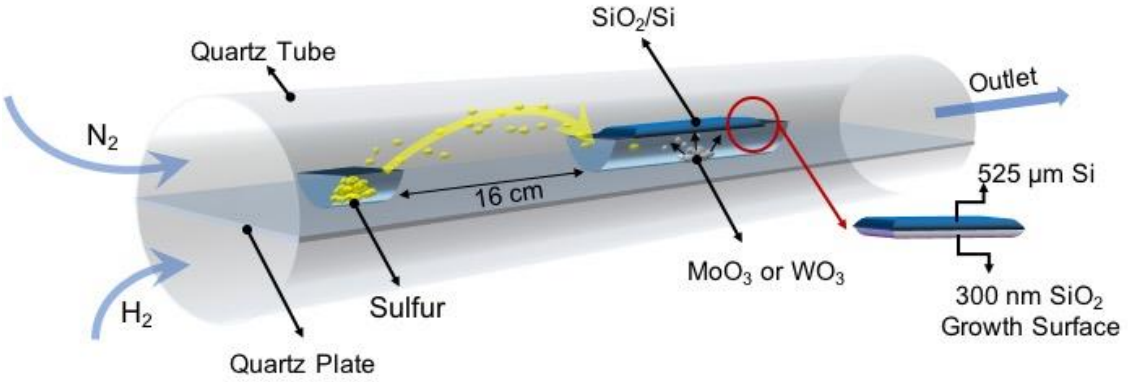

Figure 3.3 *Schematic representation of the growth zone configuration of the CVD system for TMDs growth on SiO_2/Si substrate*

3.2.2.2.The CVD growth of TMDs on glass substrate

An extraordinary amount of research has been imbibed by atomic layer thick materials, otherwise known as 2 dimensional (2D) materials, graphene[9] being the pioneer. This is elucidated largely by their extraordinary and excellent electrical, electronic, photonic, spintronic, magnetic and mechanical properties, when reconciled with their bulk counterparts. 2D materials are endowed with a myriad of exceptionally phenomenal properties that if successfully exploited, could bring new aspects to the electronic and optoelectronic applications. TMDCs as part of the 2D materials family have secured for themselves a considerable part of this research attention due to their wide direct band gaps, high photoemission and absorption properties. As this field is in a cradle state, one of the issues thwarting the mass utilization of the so called 2D materials is the lack of control ability on growth of large are high quality 2D TMDs. A good amount of research attention is given to this area, where, Micromechanical cleavage[148], solution sonication, Atomic Layer Deposition (ALD), liquid phase exfoliation, electrochemical exfoliation, chemical exfoliation, and chemical vapor deposition (CVD) are the popular growth techniques, each method having its strength as well as shortcomings[149]. The CVD methods is the most common used growth method that is widely investigated, due to its large area growth ability and affordability. Many research approaches have been applied to CVD method like sulfurization, face to face feeding or horizontal growth to have large area and high quality TMD materials. However, the progress that would enable these material systems to be removed from the laboratory and transferred to real

applications has not been made yet. Silica is one of the mostly used substrate since its dielectric layer and thermal strength. However, TMD growth on silica seems to not efficient in terms of coverage, single crystal size and lack of catalyst contents (like Na). So that, researchers attempt to find different growth substrate materials such as silica (Si/SiO_2), quartz glass, sapphire, polyimide (PI) 8 and soda lime glass. Soda lime glass has proven to be one of the best substrates out there, supporting large coverage and high-quality flakes- with perfect triangular structures; high photoluminescence (PL) intensities and low defect density. This has been proven by Chen et al, demonstrating outstanding results growing MoS_2 and $MoSe_2$, with flake size of millimeter scale[61]. So that soda lime glass (glass) is used for TMD growth in this study to overcome repeatability and coverage problem of TMDs growth. In the next sub sections, the growth configuration and growth results of MoS_2 and $MoSe_2$ materials will be given in detail.

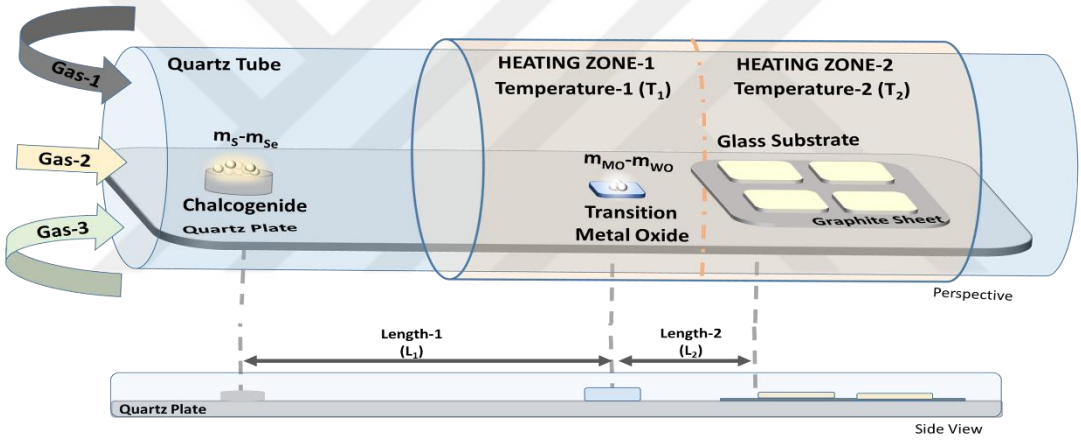

Figure 3.4 *Schematic view of CVD configuration for TMDs growth on glass substrate*

Schematic representation of CVD growth configuration is demonstrated in Figure 3.4. In this growth scheme, glass substrates are positioned next to the precursor. The growth parameters that needs to be optimized are shown in Figure 3.4 and can be summarized as follow; glass substrates are the weight of transition metal oxide (m_{Mo} ve m_{WO}) and chalcogenides (m_S and m_{Se}) precursors materials, the distance between two precursors (L_1) and the distance between transition metal oxide and growth substrates (L_2), the temperatures of precursors and substrates (T_1 and T_2), the flow rates of N_2, Ar ve H_2' carrier gases and the type of glass substrate in terms of chemical composition. These parameters optimized for each material (MoS_2 and $MoSe_2$) individually. The optimized CVD parameters of MoS_2 growth on glass are as follow; m_{Mo}: 1 mg, m_S: 300 mg, L_1: 12 cm, L_2: 4 cm, T_1: 150 °C, T_2: 750 °C and 20 sccm of N_2. The optimized CVD recipe for $MoSe_2$ growth on glass substrate can be summarized as follow; m_{Mo}: 1 mg, m_{Se}: 300 mg, L_1: 10 cm, L_2: 2 cm, T_1: 400 °C, T_2: 800 °C and 50 sccm of H_2 after T_2 reached 560 °C and 20 sccm of N_2.

3.2.2.3. Transfer procedures of TMDs

Transfer from SiO_2/Si substrate to target Substrate:

In this transfer technique, Poly(methyl methacrylate) (PMMA)-anisole (PMMA 950 A2) solvent is used as transfer medium for the 2D flakes. PMMA-anisole solvent is used as a support layer for the MoS_2 flakes when the as-grown substrate SiO_2 etched away. Another important material used during transfer is Sylgard(r) 184 silicone elastomer (Poly(dimethyl siloxane)-PDMS). PMMA is being used as flexible and a thin film for easy dissolving after transfer so that PDMS is acts as a thick support for PMMA during as-grown substrate etch and locating process. The transfer procedure is explained step by step with illustrations in Figure 3.5.

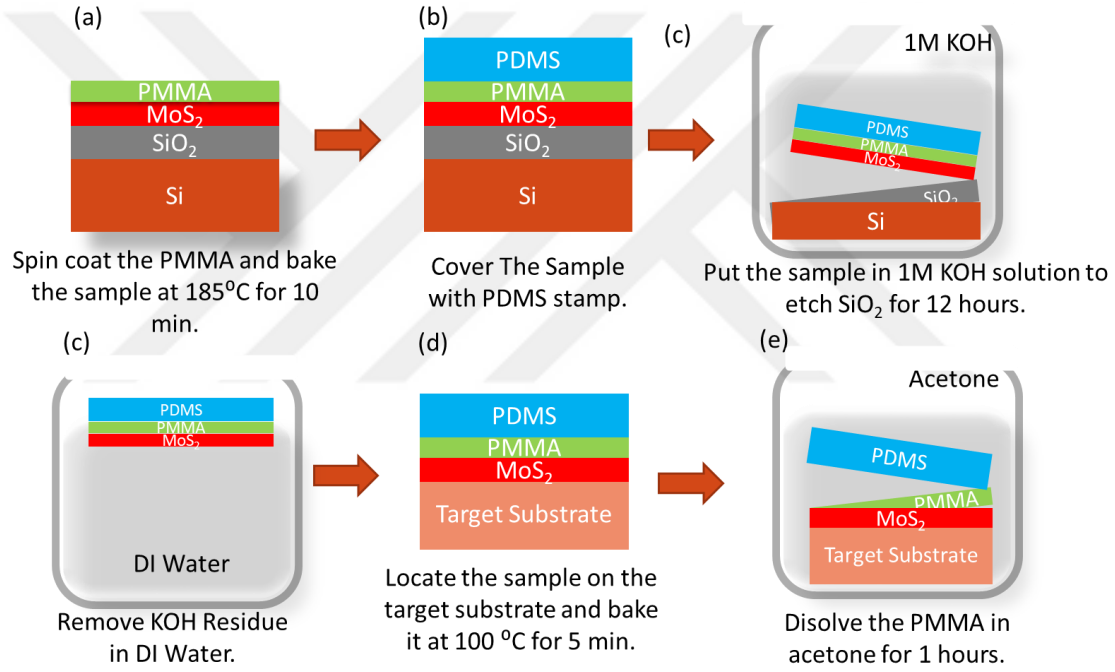

Figure 3.5 *The transfer procedure of TMDs from SiO_2/Si growth substrate to target substrate*

In figure 3.5 the transfer procedure is shown with illustration of each step. The all steps are detailed as follow;

Step-1: Coat the sample with PMMA with spin coater (2000 rpm, 500 ACL and 60 sec).

Step-2: Bake the PMMA coated sample at 185 ºC for 10 minutes.

Step-3: Cover the sample with ~2 mm thick PDMS stamp

Step-4: Throw PDMS/PMMA/MoS_2/SiO_2/Si in 1M KOH solution at 80 ºC for 12 hours to etch SiO_2 layer.

Step-5: Take the PDMS/PMMA/MoS_2 sample in DI water to remove KOH residues.

Step-6: Dry the sample and locate on the top of target substrate and bake the transferred sample at 100 ºC for 5 min to achieve uniform adhesion between target substrate and PDMS/PMMA/MoS_2 sample.

Step-7: Throw sample in hot acetone (60 ºC) to dissolve the PMMA layer for 1 hours.

Step-8: Clean the sample with acetone and Isopropyl alcohol, respectively.

Step-9: Bake the final transferred sample at 110 ºC for 1 hour to remove any solvent residue.

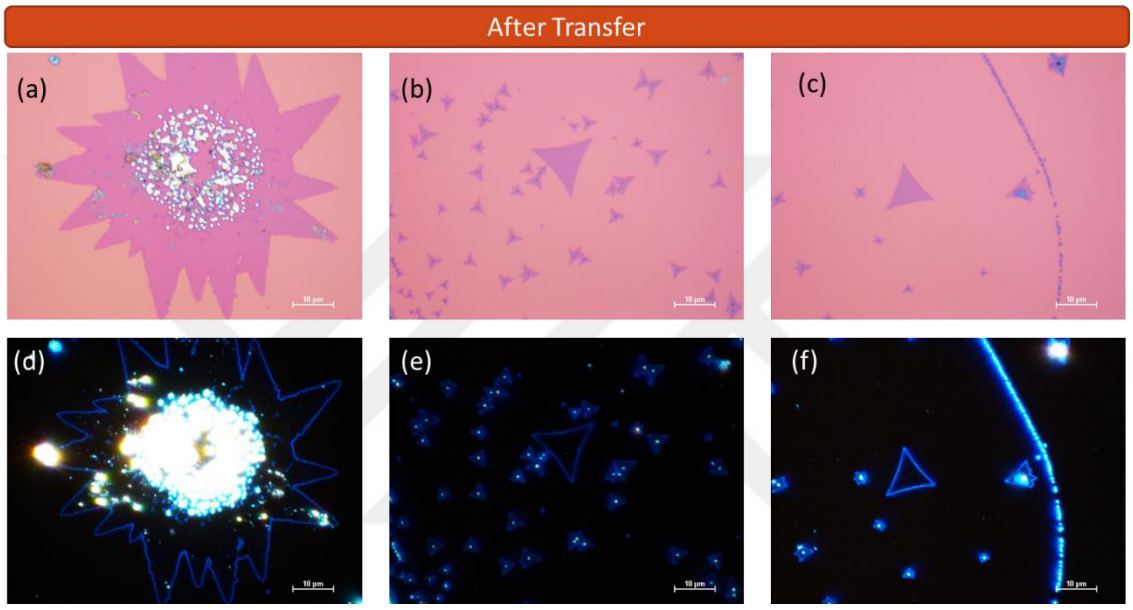

Figure 3.6 *After transfer optical and dark field microscope images of different type MoS_2 flakes*

The optimized transfer procedure has been tested for 12 months aged MoS_2 flakes to understand the effect of transfer and transfer related materials on aging and cracking of MoS_2. In figure 3.6 the transferred MoS_2 triangles and circle are shown. The MoS_2 flakes has no damages that caused by transfer procedure.

Transfer from glass substrate to target Substrate:

During previous period of the thesis the transfer procedure was optimized for the materials grown on SiO_2/Si substrate. This optimized method could still be used for materials grown on glass too. However, the previous method contains usage of KOH solution which toxic and hazardous. Using glass substrates not only allowing large area high quality growth but also the hydrophobic nature of glass make possible to use water instead of KOH which is more preferable since concerns of hazardous situations. In this

transfer technique, Poly(methyl methacrylate) (PMMA)-anisole (PMMA 950 A2)solvent is used as transfer medium for the 2D flakes. PMMA-anisole solvent is used as a support layer for the TMD flakes when the flakes detached from glass substrate by water. The transfer procedure is explained step by step with illustrations in Figure 3.7.

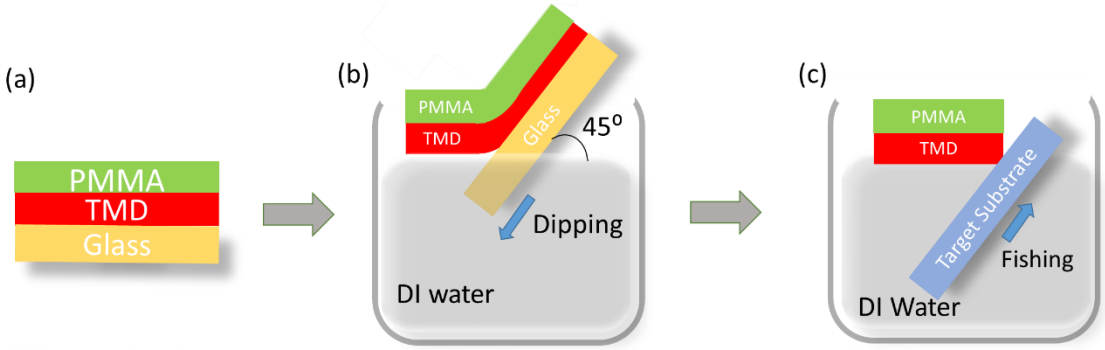

Figure 3.7 *The optimized transfer procedure for TMDC materials grown on glass*

In figure 3.7 the transfer procedure is shown with illustration for each step. The all steps are detailed as follow;

Step-1: Coat the sample with PMMA with spin coater (1000 rpm, 500 ACL and 40 sec).

Step-2: Bake the PMMA coated sample at 130 ºC for 2 minutes.

Step-3: Dip the PMMA/TMD sample into DI water with an angle of 45º with respect to water surface.

Step-4: Take the separated PMMA/TMD sample from DI water by fishing it with target substrate.

Step-5: Bake the transferred sample at 80 ºC for 10 min to achieve uniform adhesion between target substrate and /PMMA/TMD sample.

Step-6: Throw sample in hot acetone (60 ºC) to dissolve the PMMA layer for 1 hours.

Step-7: Clean the sample with acetone and Isopropyl alcohol, respectively.

Step-8: Bake the final transferred sample at 110 ºC for 1 hour to remove any solvent residue.

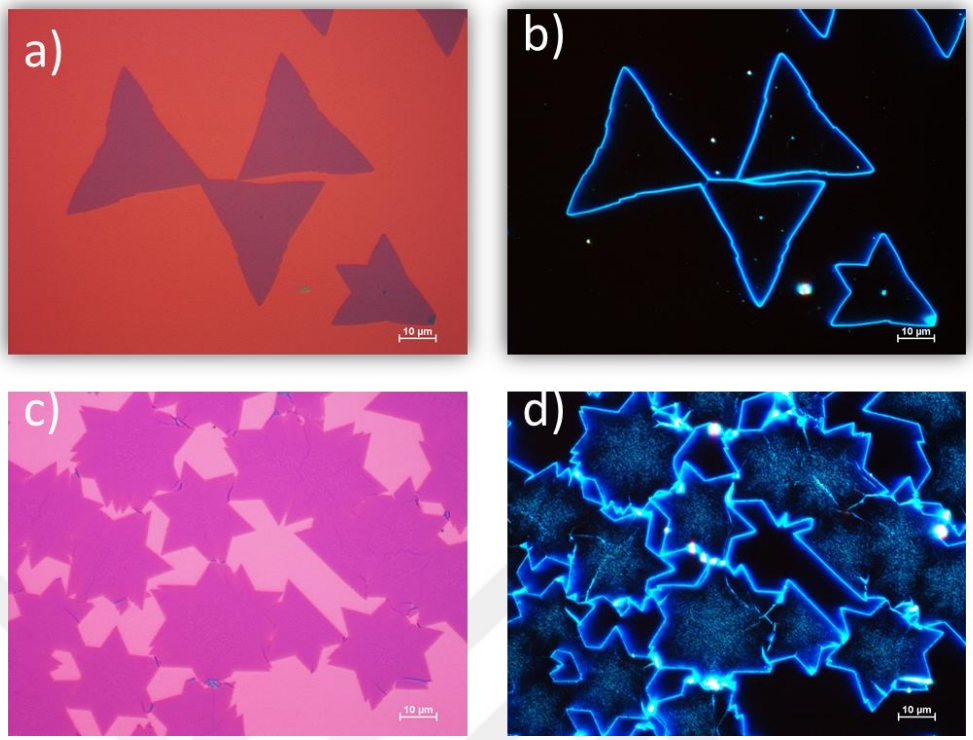

Figure 3.8 *After transfer optical bright and dark field microscope images of MoS_2 (a and b) and $MoSe_2$ (c and d) Flakes.*

In figure 3.8 the transferred MoS_2 and $MoSe_2$ triangles are shown. The flakes have no damages that caused by transfer procedure. Visual inspection proves that. Another outcome from the optical images is not only the MoS_2 flakes but also growth sourced MoO_3 or MoO_2 oxide crystals are also transferred on target substrate. This is a proof of optimized transfer procedure.

3.3. Characterization Techniques

In this thesis, Raman and Photoluminescence spectroscopy techniques iare utilized together with Fluorescence lifetime imaging (FLIM). All these characterization methods are integrated in a commercial system which is the Witec Alpha 300 R µ-Raman and photoluminescence (PL) spectroscopy system with a Zeiss, 100X, 50X, 10X microscope objectives and a 532 nm continuous wave (CW) and 485 nm pulsed laser sources. The AFM measurements are carried out with the Nanomagnetic-ezAFM system to validate the thickness of the flakes. Moreover, optical microscopy (Nikon Eclipse LV100NDA) is used for dark field imaging. Morphological features of grown flakes are also characterized by SEM using inlens-SEM techniques.

Since the Raman spectroscopy provides not only the identification of the samples, but also indirectly provides information about the thickness, doping levels and quality etc., it will be briefly introduced.

3.3.1. The μ-Raman and Photoluminescence Spectroscopy Techniques

The Raman effect is the result of the interaction between a laser beam with a defined power intensity and a sample which could be in the phase of gas, solid or liquid. The interaction of laser with sample causes elastic (Rayleigh) or inelastic scattering process if the polarization of the electric field of incident beam change within the unicell or molecule. The occurrence probability of this process is very small and very fast which is in the orders of femtoseconds that makes challenging to collect informative signal.

The result of elastic scattering event may cause red (Stokes) or blue shift (Anti-stokes) in the wavelength of incident laser beam. The stokes shifts are being used for Raman spectrum generation in almost all Raman microscope systems due to low intensity of anti-stokes shifts (122).

Raman spectra of specimen is built by collecting and dispersing the scattered light onto a charge coupled device (CCD) detector. The dispersion of the scattered light is performed by optical components called as diffraction gratings which splits the incident light into several beams. The gratings could have different resolution such 300 groves/mm, 600 groves/mm and 1200 groves/mm. In this thesis, the Raman and PL spectra are collected by 1200 g/mm and 600 g/mm gratings, if not stated otherwise . The incident light to the grating is filtered out from the excitation or Rayleigh scatterings by an edge filter. The laser beam positioning on the sample is done by optical objectives with different magnifications and numerical aperture values (NA). The spatial resolution of a Raman microscope is proportional to the ratio of excitation laser wavelength to NA (λ/NA). The spatial resolution of the 100X objectives is ranges from 400 nm to 500 nm. In addition to that the depth resolution is being calculated by λ/NA^2 which is in the orders of 1 μm. The Raman configuration used in this dissertation is as follow; 50X and 100X objectives with 0.87, 0.9 NA, 532 nm CW and 485 nm pulsed lasers and a CCD detector. The pulsed laser is used with a repetition rate of 80 MHz for FLIM measurements.

The Raman and PL spectra of 2D materials has been used determine monolayer properties of these materials such as Layer number, Coulombic interaction, electron doping and adsorbates and crystal quality.

The thickness or more specifically layer number (monolayer, bilayer, few layers and multilayer) of graphene is being estimated by the intensity ratio of G and 2D Raman modes (I_{2D}/I_G) [150]. Furthermore, the thickness of the TMDs is estimated by the difference between the position of their fundamental Raman modes (generally in plane - out of plane). In the case of two distinct Raman modes of MoS_2, these Raman modes are in plane (E^1_{2g}) and out of plane vibration of S atoms (A_{1g}) s. When moving from single layer to multilayer the frequency of E^1_{2g} mode increases, whereas in the case of A_{1g} mode it moves towards lower frequencies [123-126].

For more details and theoretical background about the Raman and PL spectroscopy of 2D materials, one could check the related literature [23, 151, 152].

3.4. Optical Lithography

The optical lithography method is a well-known and efficient method for device fabrication. The fabrication of back gated FET by patterning and depositing two metal contacts to flakes by optical lithography is explained in details step by step as follow;

Step 1. CVD grown MoS_2 flakes on SiO_2;/Si substrate are coated by AZ5214 photoresist by spin coater for 30 seconds with a speed of 3000 rpm for thickness of 1.5 or 1.6 μm.

Step 2. The photoresist (PR) coated sample baked on hot plate at 110 °C for 60 seconds.

Step 3. The optical mask aligner is used to optical lithography mask (Figure 4.a) (align designed device structure) to MoS_2 flakes on PR/SiO_2/Si sample.

Step 4. After alignment procedure, the sample is exposed 15s with 30 W UV lamp.

Step 5. The final step of patterning the PR is development step. The sample was kept in 1:4 DI water: AZ400 developer solution to etch UV seen areas.

Step 6. Patterned regions were deposited with 5 nm Ti and 100 nm Au respectively by thermal evaporator coating system.

Step 7. By dipping the metal coated sample in acetone Lift-off of residual metal regions are removed, and the final device structure is achieved as shown in Figure 3.9b.

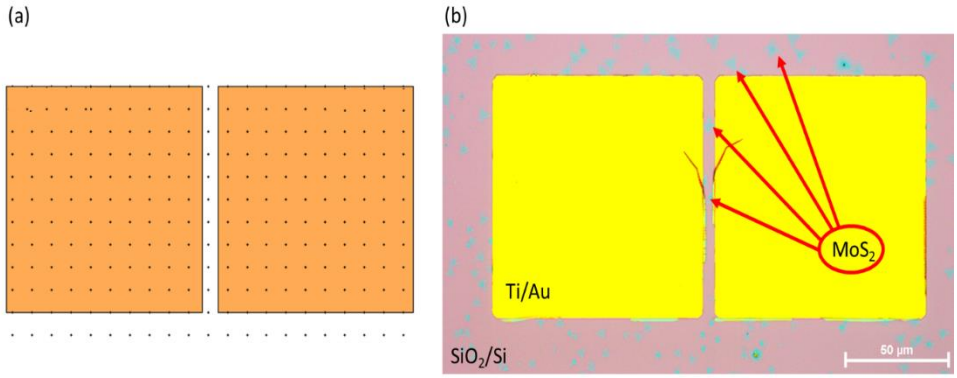

Figure 3.9 *(a) The designed back gated FET structure, (b) Optical image of fabricated final device*

3.5. Electrical and Opto-Electrical Measurements

The electrical and opto-electrical measurement has done by in-house manual probe station which is shown in Figure 3.10. The manual probe station is consisting of Stereo optical microscope, motorized positioning stage, micromanipulators with 25 µm tungsten tips and two channel source-measure unit (SMU) (Figure 3.10). The specifications of each component is listed below;

The Nikon Stereo Microscope: The microscope is equipped with three axis movement stage and 0.75X objective with 107 mm of working distance and 0.0788 of numerical aperture.

The Motorized Stage: The 3-axis motorizes stage is built in from Thorlabs-MAX302 piezo stage with 20 µm of travel distance and 20 nm of resolution (when driven by stepper motor). In addition, the stage is equipped with vacuum sample holder chuck.

The Source-Measure Unit: The SMU (Keysigth B2902A) is a two channel DC source and meter tool. It is able to supply up to 200 V with a 100 fA resolution.

The electrical characterization of fabricated devices is a two-step process. The first step is doing the dark and under illumination measurements and the second step is analysis of the measured data to extract the characteristics of the devices. During the first step for the electrical characterization, the transfer curves (I_{DS}-V_{BG}) with different drain bias voltages, the output characteristics (I_{DS}-V_{DS}) under different gate bias voltages and finally the time dependent stability curves (I_{DS}-Time) are being measured under dark conditions to eliminate the light excitation effects. For the electro-optical characterization, the mentioned electrical measurements are being repeated under illumination which is being decided according to application. In addition to under

illumination electrical measurements, the spectral response (R- $\lambda_{excitation}$ which is estimated from I_{DS}-V_{BG} measurements under different wavelength excitations), temporal response (I_{DS}-Time, along with light ON/OFF periods) and power dependent transfer measurements (I_{DS}-V_{BG} for different excitation powers) are being done. For the second step, the fundamental characteristics of a FET and Phototransistor are being estimated from the measurements.

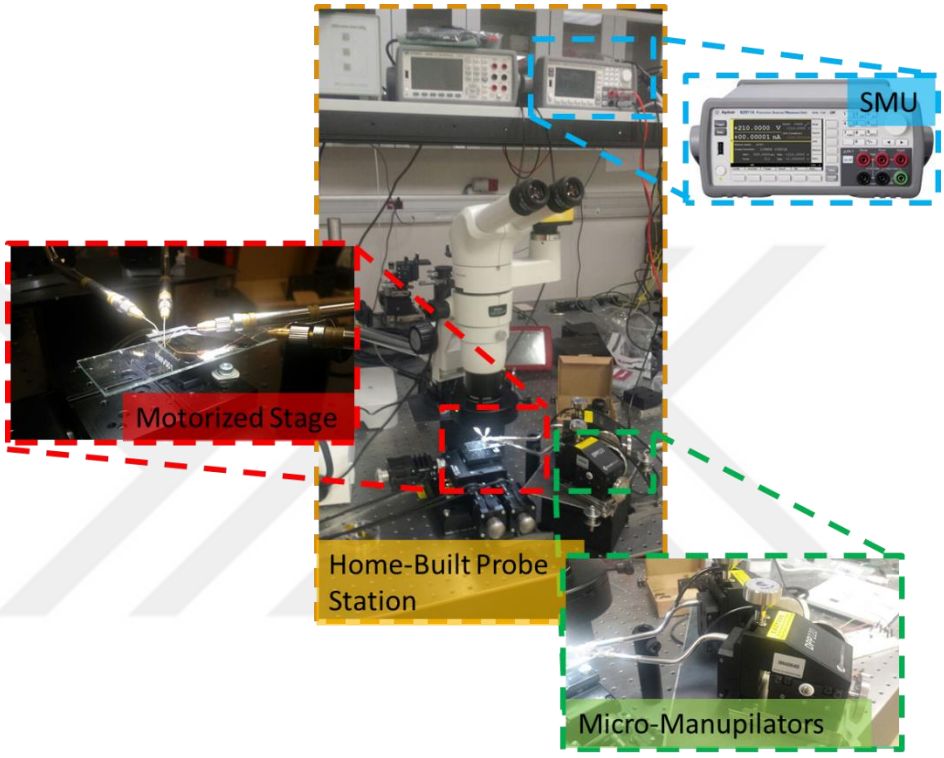

Figure 3.10 *The self-built manual probe station with environmental components*

These characteristics are current on -off ration (I_{ON}/I_{OFF}), field effective carrier mobility (μ_{eff}), subthreshold swing (SS), thershold voltage (V_{TH}) and photoresponsivity (R). The esitmation methods of these caharcteristics are summirized below.

Current ON/OFF Ratio (I_{ON}/I_{OFF}): This ratio is important parameter which is referred as maximum current modulation and informative about the power consumption and logic circuit performance of the fabricated device. The I_{ON}/I_{OFF} is being estimated from I_{DS}-V_{DS} curves where the I_{ON} current is picked as the maximum current at saturation region and the I_{OFF} current is chosen as the minimum current at the cut-off region[3].

Field Effective Carrier Mobility (μ_{eff}): Field effect mobilities are calculated from estimated transconductance from I_{DS}-V_{BG} curves as $g_m = \partial I_{DS}/\partial V_{BG}$ using:

$$\mu_{FE} = \frac{L_{CH}}{W_{CH}} \frac{1}{V_{DS} C_g} \frac{\partial I_{DS}}{\partial V_{BG}} \quad (\mathrm{cm^2 V^{-1} s^{-1}}) \quad (1)$$

Where μ_{FE} is the field effective carrier mobility, I_{DS} is drain-source current, L_{CH}/W_{CH} is the ratio of channel length to channel width, V_{DS} is bias voltage and C_g is the gate capacitance per unit area. $C_g = \varepsilon_g/t_g$ where ε_g and t_g is the dielectric constant and the thickness of gate oxide, respectively[10].

Subthreshold Swing (SS): The measured transfer curves are being used for SS estimation. The SS value of transistor is calculated by the following equation;

$$SS = \ln 10 \frac{dV_{BG}}{d(\ln I_{DS})} \quad (2)$$

Where I_{DS} is drain-source current and V_{BG} is the gate-source voltage[3].

Threshold Voltage (V_{TH}): The I_{DS}-V_{BG} curves are being used for V_{TH} calculation. Even if there several methods used for VTH estimation in this dissertation V_{TH} values are extracted during forward sweep by using Linear Extrapolation (LE) method [153]. The tangent line with maximum slope to I_{DS}-V_{BG} curve at the peak transconductance (g_m) is linearly extrapolated to V_{BG} (axis) to extract V_{TH}. This procedure is shown in Figure 3.11.

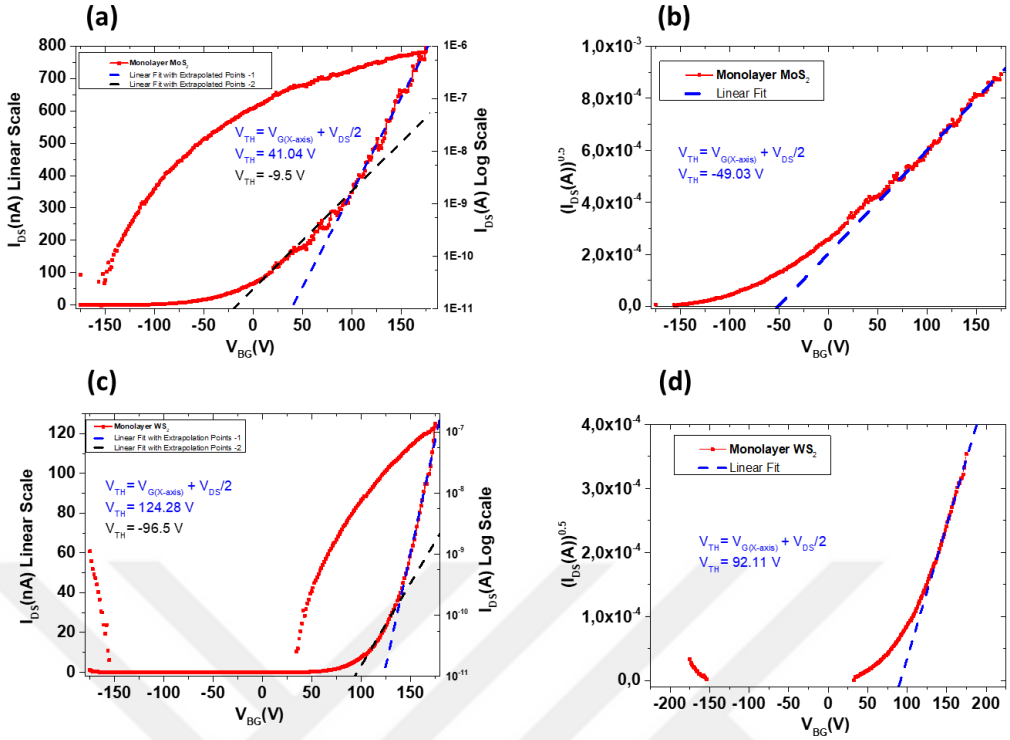

Figure 3.11 *Transfer curves of the MoS_2 (a) and WS_2 (c) based devices with linear fits. The $I_{DS}^{0.5}$-V_{BG} curves of MoS_2 (b) and WS_2 (d) based devices with linear fits.*

In Figure 3.11 the transfer curves of MoS_2 and WS_2 based devices are presented as an example to visualize the extraction of V_{TH}. The $I_{DS}^{0.5}$-V_{BG} plots (Figure 3.11b and 3.11d) are also included to show LE method in saturation region.

Photoresponsivity (R): The responsivity (R) is measured to evaluate the performance of the fabricated photodetector. It is calculated by using the photocurrent and incident effective illumination power. Photocurrent is defined as the difference between the current under illumination (I_{II}) and the dark current (I_D) as in (2). The photocurrent and responsivity are calculated as follow;

$$I_{PH} = I_{II} - I_D \qquad (2)$$

$$R = \frac{I_{PH}}{P_{eff}} \qquad (3)$$

where $P_{eff} = P_{in} \times \frac{A_{device}}{A_{beamspot}}$, A is the area and I_{PH} is the photocurrent[154].

4. GRAPHENE/MoS_2 HETEROSTRUCTURE

4.1. Introduction

2D materials has been investigated in many aspects due to their unique and outstanding characteristics since the discovery of graphene. Graphene which is the first 2D material, is zero band gap semi metallic material which has a superior carrier mobility and a native (without tuning) optical absorption of 2.3%. The monolayer MoS_2 as member of 2D TMDs family, is a semiconducting material with a direct band gap of 1.8 eV which makes it a promising candidate for electronic and optoelectronic application [1]. Furthermore, not only the usage of a monolayer but also usage of the combination of their heterostructures like modular Legos, have also drew great attention in the past few years. The origin of this attention is coming from the combining of the individual superior properties of monolayers into one heterostructure block such as using the large band gap of MoS_2 with the higher conductivity of Graphene in the same device.

Graphene/MoS_2 structure is one of the promising combinations of two-dimensional heterostructures. Graphene/MoS_2 or MoS_2/Graphene heterostructures has found various applications such as; MoS_2/Graphene based FET with a current ON/OFF ratio of $>10^3$ [2], Graphene/MoS_2 based photodetector with a photoresponsivity of $> 10^7$ AW^{-1} [3], Graphene/MoS_2 based non-volatile memory device with a current ON/OFF ratio of ~10^3-10^4 [4] and Graphene/MoS_2 based DNA biosensor which can detect DNA in concentration of 10^{-18} M [5]. Therefore, the direct growth of Graphene/MoS_2 or other 2D heterostructures has crucial importance and it is a novel and growing topic up every moment.

The first direct of growth of Graphene/MoS_2 heterostructure was done over graphene on Cu foil using an organic solvent as precursor carrier by low pressure CVD which is not convenient completely for device fabrication [6]. In another study the CVD growth of MoS_2 with solid precursors onto graphene on SiC substrate were reported [7]. Molecular beam epitaxial (MBE) growth of MoS_2 on graphene on SiC [8] and on Pt substrates are some other direct growth attempts [9]. The growth on graphene on SiO2/Si substrate was reported that they growth nanoribbon heterostructure which is applicable for specific applications [10].

Here, we demonstrate the growth of MoS_2 on top of graphene which is successfully transferred onto SiO_2/Si substrate. The CVD growth of MoS_2 is accomplished by solid

precursors of Sulphur and MoO_3 in Ar ambient. Optimization is done by choosing the proper sulphur weight which is substantive at determining the flake thickness and flow rates of carrier gas. The coverage difference of graphene on the substrate showed that the growth of MoS_2 occurs mostly on top of the graphene rather than the oxide surface. In addition to that the detailed Raman and PL spectroscopy analysis of the direct growth and transferred MoS_2 on top of Graphene is examined and results are discussed here. The characterization of formed heterostructures is done by SEM, Raman and PL spectroscopy and optical microscopy. It is shown that the MoS_2 flake sizes are larger than several microns and also the flake distribution over graphene is seen to be almost uniform according to SEM analysis while there are rarely MoS_2 flakes over oxide surface.

4.2. CVD Growth Procedure of Graphene /MoS_2 Heterostructure

The direct growth procedure of MoS_2 on Graphene/SiO_2/Si is schematically shown in Figure 4.1. The CVD method is used for the growth of MoS_2 by using the solid precursors S (Sulphur) and MoO_3. The S and MoO3 precursors are located on the specific positions where the temperatures are 130 °C and 700 °C during growth to obtain optimum vapor pressure of S and Mo on top of the graphene coated substrate (Figure 4.1). The distance between S and MoO_3 is fixed as 18 cm. Split furnace is used to have a mobile heater body to control the growth process carefully. When the growth temperature is reached, the furnace is shifted to the S precursor region to achieve sufficient flux of sulphur vapor to prevent formation of molybdenum oxides. When all the Sulphur evaporates, the upper furnace is lifted up for fast cooling to prevent secondary nucleation. The schematic illustration of the furnace and furnace positions before and after the growth temperature is demonstrated in Figure 4.1a and 4.1b. The graphene growth and transfer is done as described in chapter 3. The graphene position on SiO_2/Si substrate and sample dimensions are shown in Figure 4.1c and 4.1d. There are two growth configuration which has been used for MoS_2 growth on SiO_2/Si substrates up to now. These are side by side growth (horizontal growth) and face-down growth (Figure 4.1c and 4.1d). The side by side and face-down growth scheme is optimized in the manner of sample positions and precursor ratios and used gasses with bare SiO_2/Si samples before using the graphene coated samples.

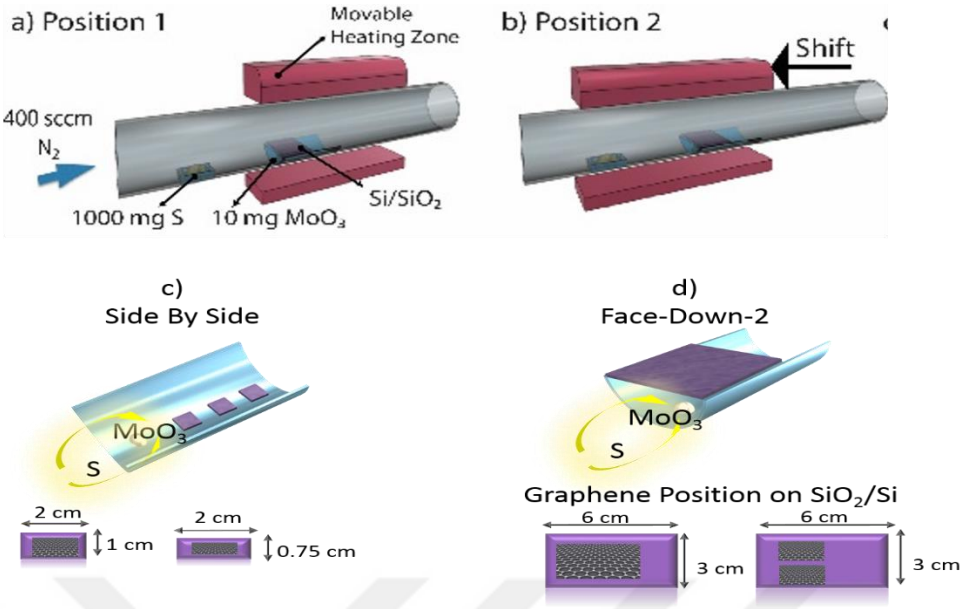

Figure 4.1 a) *Schematic configuration of the growth system and the initial furnace position (position 1) b) Furnace position 2 is used when the growth temperature is reached. Furnace is shifted on the sulphur powder c) The side by side growth configuration with sample dimensions and graphene position on SiO_2/Si substrate d) The face down growth configuration with sample dimensions and graphene position on SiO_2/Si substrate*

The direct growth experiments are performed with same growth framework defined above but with slightly chanced parameters. These parameters are the distance between sample and MoO3 and the growth procedure (horizontal or facedown growth). The growth recipes used for MoS2 on graphene growths are listed in Table 4.1.

Table 4-1. *The growth recipes of direct MoS_2 growth on Graphene/SiO_2/Si Substrate. Yellow colored cells indicates the changed parameter with respect to previous experiment recipe.*

# of Experiment	Precursor Rates (mg)	Flow (sccm)	Sample Position (Side/Top)	Sample Distance (Distance from MoO_3)	Sample Size
1	MoO_3: 2 S : 200	N2:400 H2:0	Side by Side	2.5 cm	0.75 cm x 2 cm
2	MoO_3: 2 S : 200	N2:400 H2:0	Side by Side	2.5 cm	1.5 cm x 2 cm
3	MoO_3: 2 S : 200	N2:400 H2:0	Side by Side	6 cm	1.5 cm x 2 cm
4	MoO_3: 2 S : 200	N2:400 H2:0	Side by Side	4 cm	1.5 cm x 2 cm
5	MoO_3: 2 S : 200	N2:400 H2:0	Side by Side	2.5 cm	1.5 cm x 2 cm
6	MoO_3: 1.5 S : 1000	N2:396.75 H2:3.75	Face Down	-	4 cm x 6 cm (Graphene on two possible flake growth positions)
7	MoO_3: 1.5 S : 1000	N2:396.75 H2:3.75	Face Down	-	4 cm x 6 cm (Full Coated with graphene)

In Exp.-1 to Exp.-5 the flow rate N_2, the ratio of precursors (MoO_3-S) and sample dimensions are kept constant as 400 sccm, 2-200 mg and 1.5x2 cm^2, respectively. But the optimum sample distance with respect to MoO_3 is scanned in a range of 2.5 to 6 cm in order to optimize the growth.

In addition to the direct grown MoS_2/Graphene/SiO_2/Si structure, the same heterostructure is formed by transferring CVD grown-MoS_2 on SiO_2/Si to graphene coated SiO2/Si to compare the effect of graphene on the growth and physical properties of MoS_2. The details of the TMDs transfer are given in experimental techniques chapter (chapter 3).

4.3. Raman, PL and Fluorescence Lifetime Imaging Analysis

In Figure 4.2a the brigth field optical microscope (OM) image of graphene which is CVD-grown on Cu and transfered onto SiO_2/Si substarte is represented. Graphene shows an uniform contarts distrubution with small darker region which reperesent multilayer islands on continious monolayer graphene.The thickness of the graphene is verified by Raman spectroscopy as shown in Figure 4.2c [150]. The size of MoS_2 triangles grown on SiO_2/Si substrate by CVD ranges around 20-30 μm and has a seed structure in the middle of the triangles which is assumed to be the start points of the growth (Figure 4.2b and 4.2d) [155]. The dark field OP image of MoS_2 on SiO_2/Si represents the edge profiles of MoS_2 flakes (Figure 4.2e).

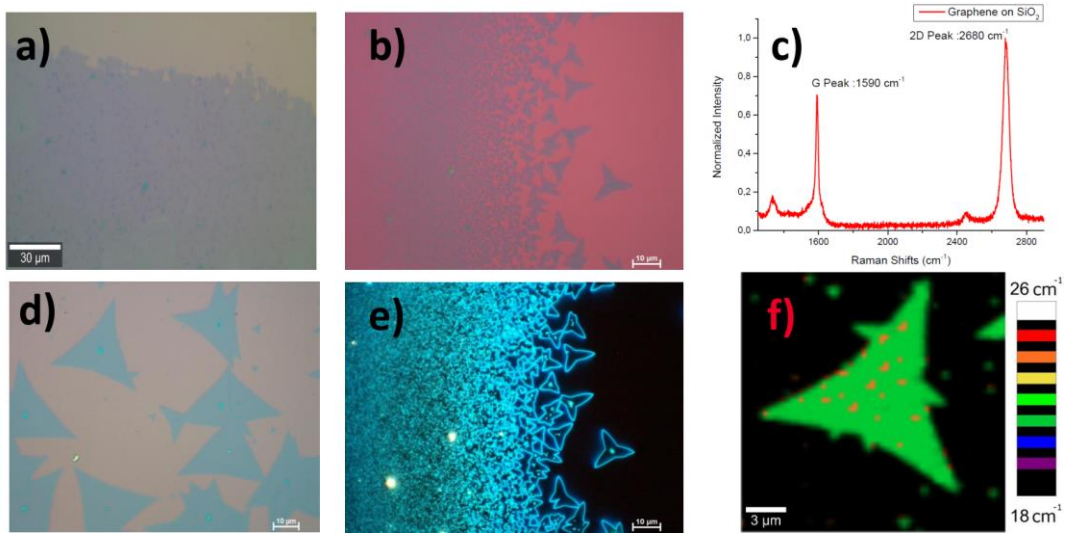

Figure 4.2 *The optical microscope image of (a) Graphene on SiO_2/Si, (b) and (d) MoS_2 on SiO_2/Si. (c) the single point Raman spectrum of Graphene on SiO_2/Si. (e) the dark field microscope image of MoS_2 on SiO_2/Si (The same region in (b)). (f) the map of Raman shift difference between the Raman modes of MoS_2 which are E^1_{2g} and A_{1g}.*

The Figure 4.2f represents the map of Raman shift difference between the Raman modes of MoS_2 which are E^1_{2g} and A_{1g}. As mentioned before, this difference between the raman modes of MoS_2 is being used to determine the thickness of the MoS_2. The position difference around 18-21 cm^{-1} means the MoS_2 formations are monolayer [152]. The map of the Mos2 triangle flakes is covered by the green color which refers to a position difference of 21 cm^{-1} and monolayer formation.

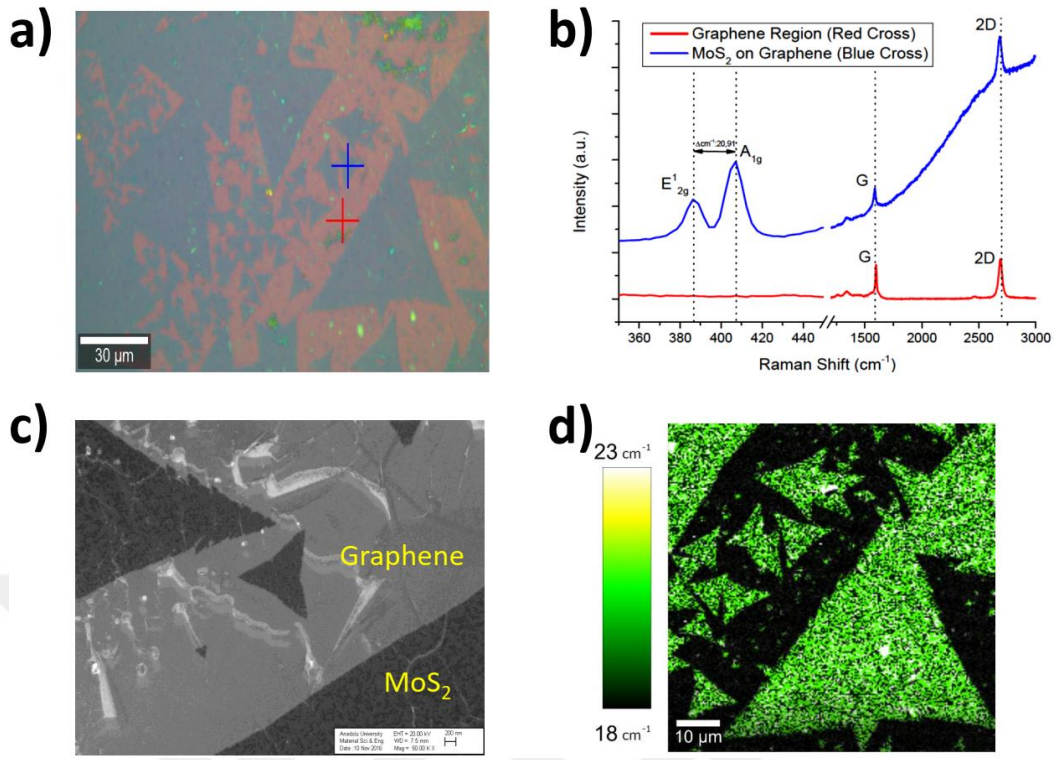

Figure 4.3 *Transferred MoS_2 on top of the Graphene/SiO_2/Si. (a) The bright field optical microscope and (c) the SEM image of formed heterostructure, (b) Single point Raman spectra of MoS_2/Graphene/SiO_2/Si (blue cross) and Graphene/SiO_2/Si (red cross) regions, the map of Raman shift difference between the Raman modes of MoS_2*

In Figure 4.3 The visual and Raman spectroscopy analysis of transferred MoS_2 onto graphene/SiO_2/Si are demonstrated. The transfer procedure caused damages due to overheating. The damaged regions are visible in the bright field optical and SEM images (Figure 4.3a and 4.3c). Since, the resolution of the Raman microscope is very high (spatial resolution is around 300nm with 100x objective.), the macro damages assumed to not affect the characterization results. The Raman spectra of blue and red crosses on the heterostructure are shown in Figure 4.3b which proves the formation of MoS_2 graphene heterostructure. The Raman modes of Graphene and MoS_2 are clearly visible from the spectrum. Furthermore, the thickness of MoS_2 is determined from the difference between Raman shift modes of MoS_2 and mapped through the triangle flake on graphene. The dominant color on the Raman shift difference map of heterostructure is green which means the difference between Raman modes of MoS_2 is around 19-21 cm^{-1} that shows the monolayer MoS_2 on top of the graphene.

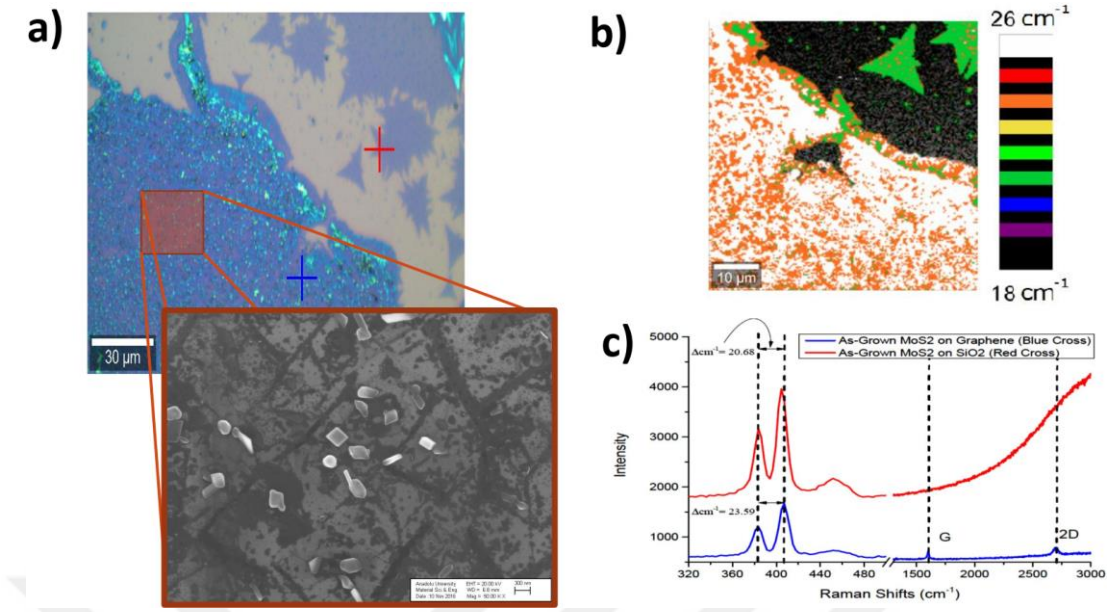

Figure 4.4 *The direct grown MoS_2 on top of the graphene/SiO_2/Si. (a) The optical image of direct grown MoS_2 on graphene, the inset shows the higher magnification (50000KX) SEM image of the marked region. (b) the map of Raman shift difference between the Raman modes of MoS_2 (c) the single point Raman spectra of MoS_2/Graphene/SiO_2/Si (blue cross) and MoS_2/SiO_2/Si (red cross).*

In order to compare the direct growth effect on the characteristics of the heterostructure, the direct grown MoS_2 on top of the graphene/SiO_2/Si substrate is analyzed by Raman spectroscopy, too. In Figure 4.4a the OM image of the direct grown heterostructure by two step CVD methods are demonstrated. The boundary of the graphene coated region and two different formation of MoS_2 are clearly visible. The first formation on the SiO_2/Si region is large monolayer triangle like flakes. The second formation of MoS_2 on the graphene is thick MoS_2 clusters. However, the SEM image of the marked regions shows the monolayer flakes with sizes of 100–200 nm. Besides, since the spatial resolution of the Raman system with 100X objective is ~300 nm, the monolayer flakes are not distinguishable. Hence the Raman signal is being collected as the cumulative sum of signal from the thick clusters and monolayer flakes. Then the overall Raman spectrum shows multilayer MoS_2 formation on top of graphene.

In addition to Raman Analysis of the transfered and direct growth heterostructure of MoS_2-graphene, the PL measuements and analysis has been done. In figure 4.5, the PL analysis results are shown.

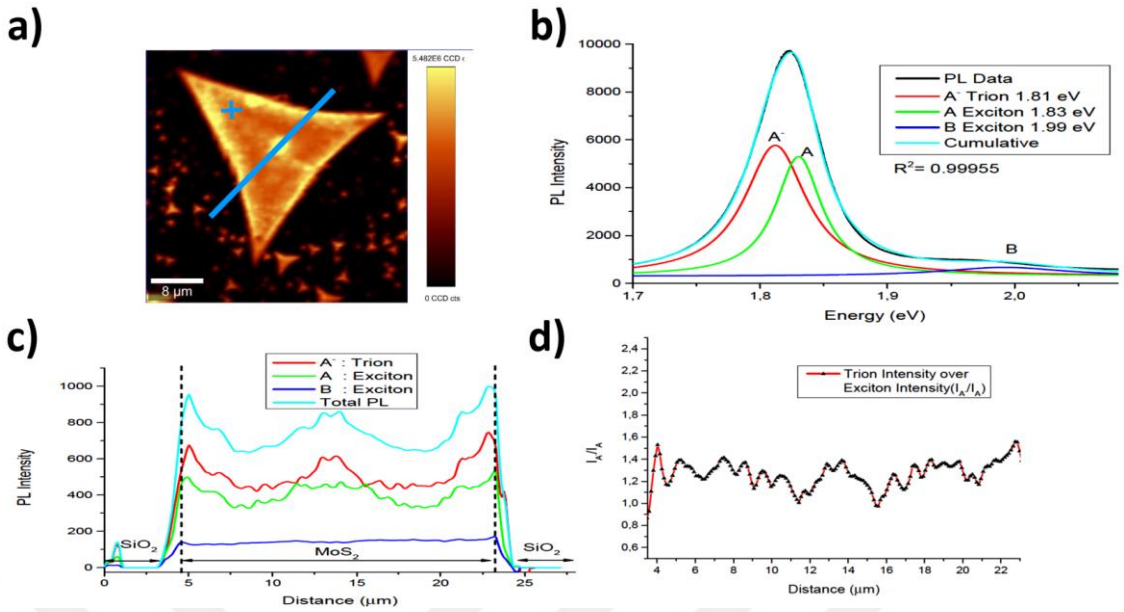

Figure 4.5 *The PL analysis of monolayer MoS_2 on SiO_2/Si. (a) the integrated PL map of the monolayer MoS_2 triangle flakes, (b) the single point PL spectrum of MoS_2 with decomposed excitonic species taken from blue cross, (c) the PL intensity profile of each excitonic specie through the blue line on the triangle, (d) the intensity ratio of A-trion over A-excitonic along with the blue line.*

The integrated PL map of bare MoS_2 on the SiO_2/Si substrate, shows very high intensity over whole triangle with non-uniform intensity distribution (Figure 4.5a). The integrated PL intensity on the edge sides of the triangle is higher than the one in interior regions. The PL emission of MoS_2 is a cumulative emission which comes from different mechanisms which are A^- trion (charged exciton) , A-exciton and B-exciton [156]. These features are obtained by fitting three Gaussian curves to the raw data (Figure 4.5b). It is known that the central wavelengths of A trion, A-exciton and B-exciton are in the ranges of 1.81-1.83 eV, 1.84-1.87 eV and 1.97-2.02 eV, respectively [156]. The extracted central wavelengths of these excitonic features by fitting are consistent with reported values in literature. According to extracted intensity profiles of excitonic mechanisms, the A-trion seems to be the dominant mechanism which is known to be a result of high defect/trap density that creates trap states close to the conduction band minimum (Figure 4.5c). The high defect density is a chronic problem of CVD-grown TMDs [157]. In Figure 4.5d the intensity ratio of A-trion over A-exciton (I_{A^-}/I_A) along with blue line on the flake is given which validate the high defect density for entire flake.

The same PL analysis made for bare MoS_2 on SiO_2/Si is repeated for MoS_2-Graphene heterostructures which are formed by transfer and direct-growth of MoS_2 on top of graphene (Figure 4.6).

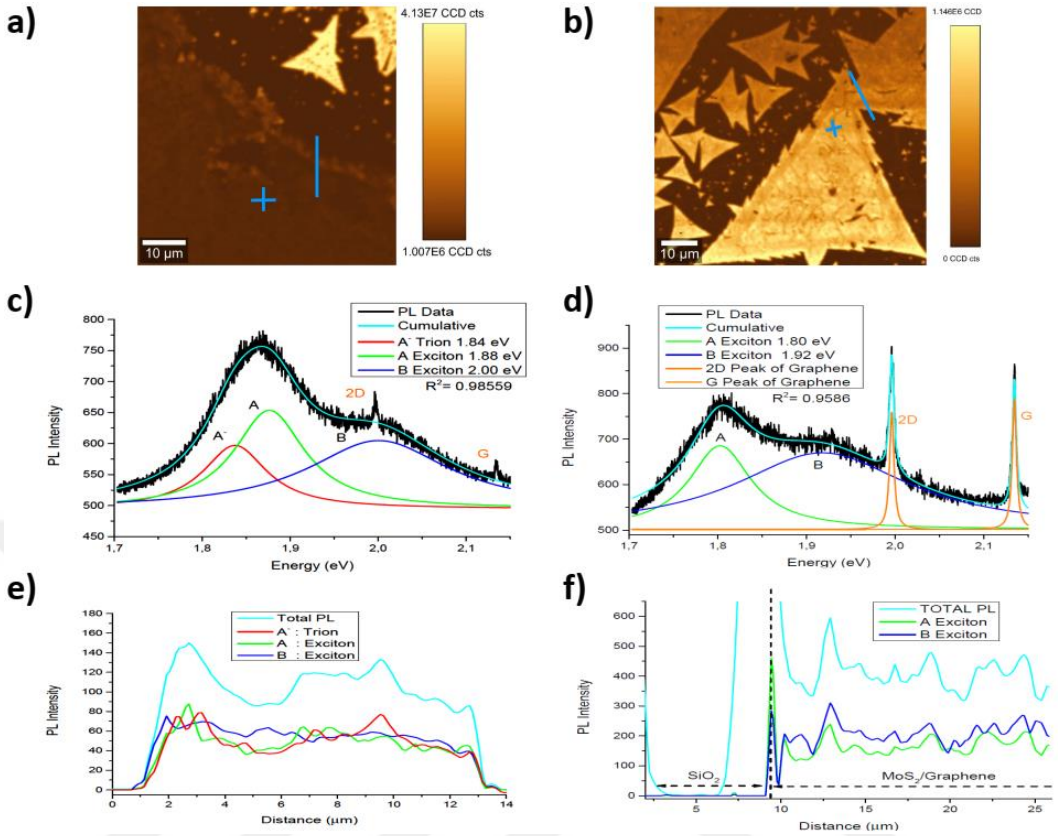

Figure 4.6 *The PL analysis of transferred and direct-grown MoS_2-graphene heterostructures. The integrated PL maps of the transferred and (b) the direct-grown MoS_2-graphene heterostructures. The single point PL spectra of (c) the transferred and (d) the direct-grown MoS_2-graphene heterostructures with decomposed excitonic species taken from blue crosses. The PL intensity profiles of each excitonic specie through the blue lines on (e) transferred and (f) direct-grown MoS_2-graphene heterostructures.*

In Figure 4.6a and 4.6b the integrated PL maps of transferred and direct-grown MoS_2-Graphene heterostructures are represented. The integrated PL intensity distribution over the heterostructures are close to each other. However, the PL intensity of heterostructures with respect to bare MoS_2 on SiO_2/Si, is quenched with a factor of 10. The PL quenching in semiconductor TMDs may occur due to increased thickness, charge transfer or chemical modifications [158, 159].

The PL analysis for transferred MoS_2 on Graphene /SiO_2 heterostructure shows that there is no dominant excitonic mechanism through the blue line. Besides, the intensity ratio of A-trion over A-exciton intensity ratio is around one through measurement line and the PL intensity distribution is uniform over the triangle flakes.

On the other hand, The PL analysis of the heterostructure with direct grown MoS_2 on Graphene shows two different regions. The first region is the heterostructure region with quenched PL distribution and the second region is monolayer MoS_2 flakes with uniform and higher PL distribution which grown on SiO_2/Si. The quenched PL at heterostructure region is expected due to increased thickness of MoS_2. However, uniform and higher PL of monolayer flakes may be result of existence of graphene. The A-exciton and B-exciton intensity through the blue line shows that the intensities of A and B excitons are almost same. In addition to that, the measured PL curves could not fit with A-trion peaks which may be the result of PL intensity quenching.

4.4. Conclusion

In this study, the Raman and PL analysis results of the heterostructures of MoS_2/Graphene formed by transfer and direct grown MoS2 represented and compared by the bare monolayer MoS2 which is grown by CVD on SiO2/Si. The effect of transfer procedure and graphene on PL and Raman spectrums of MoS_2 has also been studied in detail. Additionally, the heterostructure has been characterized by SEM and optical microscopy. It is found that the PL intensity of the MoS_2 has been quenched as one order of magnitude because of charge transfer between MoS_2 and graphene. A blue shift has been measured on peak center of A-exciton which is the result of stress relaxation. That the stress formed during growth has been relaxed due to weak van Der Waals bonding of MoS_2/graphene.

5. LONG TERM STABILITY OF TMDs

5.1. Introduction

Two-dimensional (2D) transition metal dichalcogenide (TMD) semiconductors such as monolayer or few-layer MoS_2, WS_2, and $MoSe_2$ etc. have attracted significant attention due to their potentially excellent electronic and optical properties. In particular, researchers have put significant effort to adopt these materials in future optoelectronic and photonic applications[160, 161]. Bandgap transition from indirect (bulk) to direct bandgap (monolayer) and valley selective polarization drive the main interest towards adaptation and integration of these materials especially into optoelectronics field [15, 162]. As a member of TMD family, MoS_2 is one the most popular 2D semiconductor materials and a potential candidate for the next generation electronic and optoelectronic devices including resonators, phototransistors, chemical sensors, biosensors, photodetectors, amplifiers and batteries [101].

In addition to electronic and optoelectronic properties, the integration compatibility of these materials into practical devices, considering manufacturing procedures, is another significant issue that requires large scale and high-quality growth systematics with long-term chemical and mechanical stability. Aspects related to self-limiting, controllable, homogeneous and large-scale growth remain as main challenges in the growth of TMD layers [55, 163]. To this end, micromechanical exfoliation (ME), liquid phase exfoliation (LPE), physical vapour deposition (PVD), solution chemical process (SCP), chemical vapour deposition (CVD), molecular beam epitaxy (MBE) and metalorganic chemical vapour deposition (MOCVD) have been studied to obtain monolayer TMDs specifically for MoS_2 [149, 164-166]. Although the growth mechanism of these materials has not been fully well understood large scale film and/or flake growth is achieved to some extend by the mentioned methods including cost effective CVD systems and more complicated MOCVD systems[166].

CVD is a promising and cost-effective technique in terms of capability of achieving large isolated flakes (2000 μm $MoSe_2$-glass [61]) and large-scale films [167]. In the process of integration of these flakes into different devices and heterostructures, it is a critical requirement to ensure their chemical and mechanical stability for the reliability of the intended operation. In this respect, formation of cracks (cracking) and aging behaviour of the CVD grown MoS_2 or other TMDs need to be understood and controlled to validate

the promising future of the monolayer TMDs. MoS_2 and other TMDs (CVD grown or exfoliated) were known to be chemically and mechanically stable under ambient conditions until the study of Gao *et. al.* [159]. Gao et al have demonstrated that MoS_2 and WS_2 do not preserve their physical integrity for a period of 1 year. The structural instability of the flakes has been associated with the possible oxidation and the adsorption of organic contaminants to these monolayers. On the other hand, fracture behaviour of MoS_2 has also been studied by Hao *et. al* [168]. They have shown that the quenching of the flakes by N_2 induces thermal strain and sulphur vacancies, which cause fractures in 2D MoS_2 formations, underlining the importance of sulphur vacancy defects and tensile stress induced during growth [168, 169]. On the theoretical perspective, Martincova *et. al.* has studied the oxidation profile of MoS_2 at grain boundaries and edges using density functional theory (DFT) calculations. They have demonstrated that the oxidation is favoured at grain boundaries and edges rather than on the surface of the MoS_2, which results in atomically thin chain like MoO_3 structure at boundaries or edges. The lattice mismatch between the MoO_3 structure and the remaining MoS_2 layer causes stress, resulting in cracks at boundaries or edges [170]. Furthermore, KC *et. al.* has shown that oxygen adsorption and dissociation kinetic barrier of MoS_2 is reduced by half in the presence of Sulphur (S) vacancy defect [171]. Therefore, previous studies underline the cracking and aging problem of 2D MoS_2, which is attributed to the residual thermal strain effect, and S vacancy induced oxidation [168, 169, 172, 173]. However, the reliability of such monolayers in terms of long-term mechanical integrity is not thoroughly studied and no prominent solution has been proposed for this critical problem yet. Therefore, it is still a critical and challenging task to understand and provide a solution to the formations of the cracks and aging issues for these materials intended for particular use in the electronic and optoelectronics.

In this study, we propose a MoS_2-specific solution to the stability problem of TMDs by controlling the precursors vapour concentration on the growth surface while investigating origins of the cracking behaviour of these materials in detail considering long term observation, thermal aging tests and first principle calculations. We compare long term aging behaviour of two different growth configurations, namely horizontal (HO) (proposed) and face-down (FD) (commonly used), by keeping the remaining growth parameters identical (Figure 5.1). In this regard, the proposed configuration sheds light onto the growth mechanism and provides a solution for the stability-fracture issue for

TMDCs, specifically for MoS_2 monolayers reported in this work. A clear difference is found in the mechanical stability of the flakes grown by FD and HO approaches (Figure 5.1), where the FD grown flakes spontaneously crack but HO flakes remain unchanged and keep their as grown structures for the duration of their observation period, exceeding 18 months. In addition to the long-term aging experiments at ambient conditions, MoS_2 flakes grown with the FD and HO growth methods have been aged with thermal annealing to test the reliability of the proposed method. Our analysis on the MoS_2 flakes using spatially resolved Raman and photoluminescence spectroscopy measurements demonstrate a clear resistance to oxidation and moisture absorption of the MoS_2 flakes when the horizontal approach is utilized, which is suggested to be linked with the precursor vapour concentration on the growth surface. Therefore, we emphasize the importance of the growth zone geometry and propose a growth approach enabling durable flakes against oxidation and moisture at ambient atmosphere. In addition to that, the role of tensile stress and S vacancy defect on aging is investigated with first principle calculations to understand the mechanism inducing aging.

5.2. The CVD Configurations of HO- and FD-Growth

Monolayer MoS_2 flakes/films on SiO_2 substrate are synthesized using CVD technique. A schematic representation of FD and H CVD growth configurations is demonstrated in Figure 5.1a. A quartz tube with a diameter of 8 cm and a length of 150 cm is used as the growth chamber. Growth duration, referring to the reaction time of 1mg MoO_3 and 150 mg Sulphur at 700 ºC, is set to 10 min for both of the mentioned configurations. N_2 flow of 400 sccm is used as the carrier gas and oxidation protection (Figure 5.1a, 5.1b and 5.1c). The growth parameters such as the amount and positions of precursors, growth temperature, cooling and heating rates and carrier gas flow rate, are kept identical for FD and HO growth procedures. For the FD growth schemes, the SiO_2 substrate is positioned on the top (vertically) of MoO_3 precursor as shown in Figure 5.1a and 5.1b. In the HO growth, Si/SiO_2 substrate is positioned next to the MoO_3 precursor (Figure 5.1a and 5.1c). The distance between the substrate and the MoO_3 precursor is fixed at 1.5 cm on the vertical axis and 5-8 cm on horizontal axis for FD and HO growth, respectively.

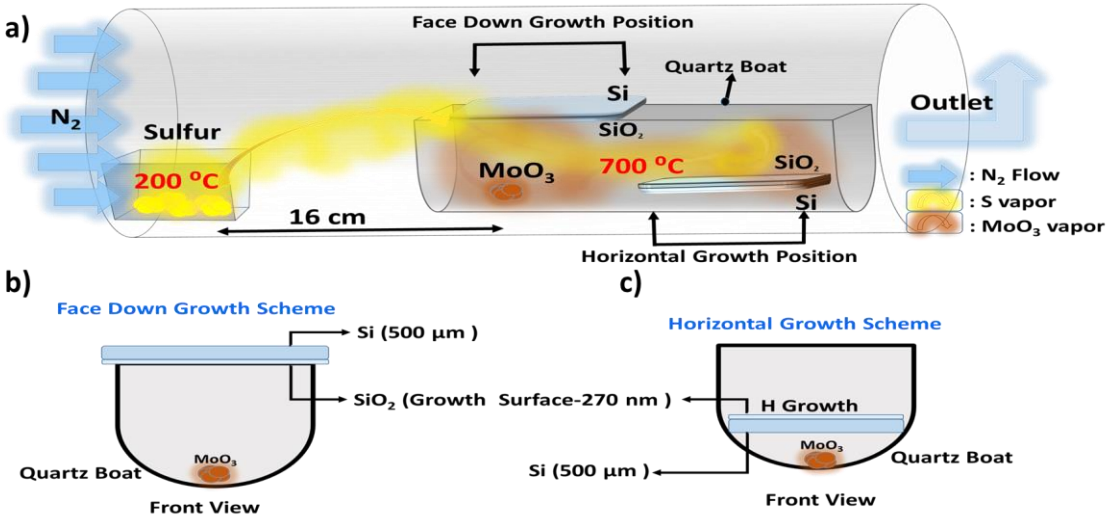

Figure 5.1 *Schematic view of the CVD growth configuration for FD and HO growth (a), Front view of FD growth scheme (b), Front view of HO growth scheme (c).*

In Figure 5.2a, Raman fingerprints of as-grown FD and HO grown MoS_2 (E^1_{2g} and A_{1g}) have been identified and deconvoluted using Lorentzian curves to identify the individual Raman modes [152]. The difference between Raman mode (E^1_{2g} and A_{1g}) positions of MoS_2 is used to determine the thickness of the grown layer[152]. The E and A modes of Raman shift differences are found to be 21.2 ±0.19 cm^{-1} and 21.0 ±0.16 cm^{-1} that indicate monolayer MoS_2 for FD and HO growth, respectively. The PL spectra of FD and HO grown flakes are shown in Figure 5.2b which are typical MoS_2 PL spectra with A-exciton and B-exciton peaks. The PL centre wavelength of the HO grown MoS_2 is red shifted with respect to FD grown flake about 1.37 ±0.17 nm.

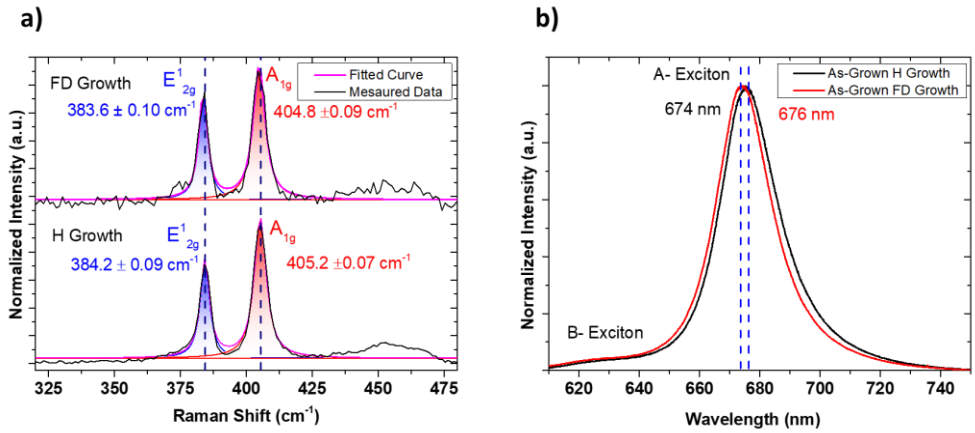

Figure 5.2 *a) Raman spectra and b) PL spectra of as-grown MOS2 with FD and H configurations.*

Rather than single spectrum measurements statistical analysis is required because of the spatial growth dependent strain structure heterogeneity over each MoS_2 flake [169, 173, 174]. Hence, Raman and PL mapping measurements are performed.

5.3. Naturally Aged MoS_2 Flakes Grown by FD and HO CVD growth Configurations

In Figure 5.3a and 5.3e, the optical microscope images of FD and HO as-grown MoS_2 flakes are shown, respectively. For both of the growth configurations the triangular flakes are uniform monolayers apart from the multilayer seed region in the centre of the triangles. However, the FD grown flakes, after the 18 months aging process, have become fractured and exhibit cracks and voids through the network as shown in Figure 5.3c. The grain boundaries and edges, having higher defect density, are observed as primary regions of cracking formation as can be deduced from the optical images of 18 month-aged and SEM images of 6 month-aged FD grown samples (Figure 5.4, Figure 5.3c, Figure 5.5a and 5.5b). On the other hand, HO grown flakes have kept their structural integrity and show no signs of fracturing or structural degradation. All of the samples were kept under ambient conditions at room temperature (25 ºC) without drying desiccant and any other special treatment like encapsulation.

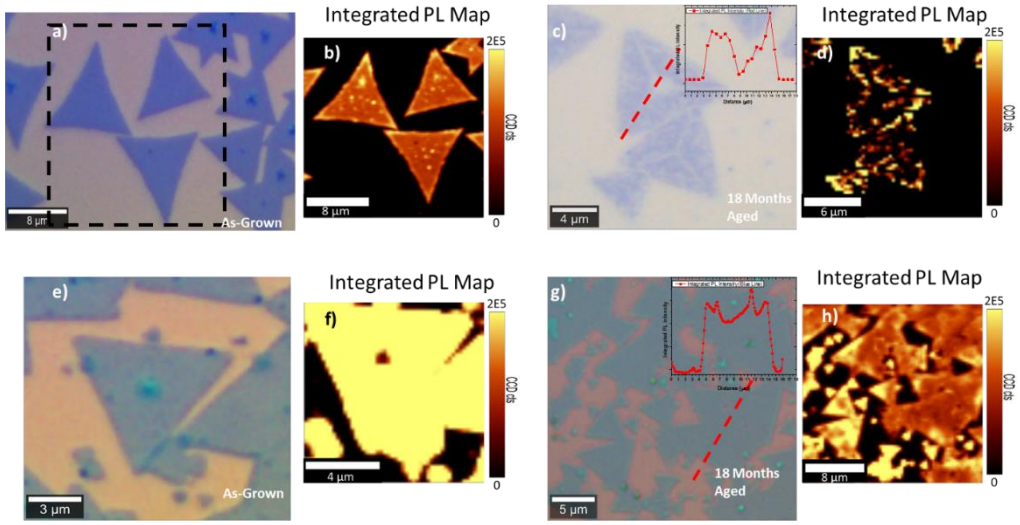

Figure 5.3 *Optical microscope image of as-grown FD flakes (a), integrated PL intensity map of the depicted area for the as-grown FD flakes (b), optical microscope image of the aged (18 months) FD grown flakes (c) (Inset indicate the integrated PL intensity through the red line on the flake), Integrated PL intensity map of 18 months aged FD flakes (d), Optical microscope image of as-grown HO grown flakes (e), Integrated PL intensity map of as-grown HO flakes (f), Optical microscope image of 18 months aged HO grown flakes (g) (Inset graph is the integrated PL intensity through the red line on the flake), Integrated PL intensity map of 18 months aged HO flakes (h).*

In Figure 5.4, the SEM images of FD grown fresh and 6 months aged samples are shown. The SEM images of six months aged samples indicates the initial circumstantial evidence of aging that can be observed via the formed voids trough surface and on the edges and line cracks trough grain boundaries (Figure 5.4).

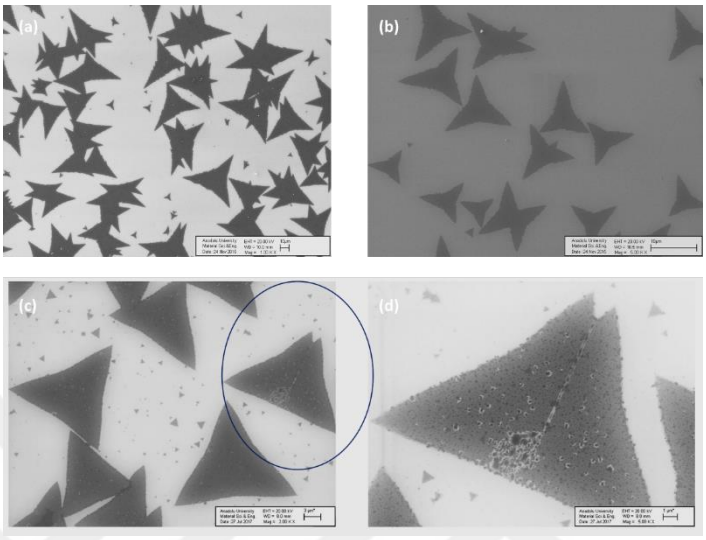

Figure 5.4 *The SEM images of FD grown fresh MoS_2 flakes 1kX (a), 5kX (b) and 6 months aged flakes; 5kX (c) and 20kX magnification (d).*

Figure 5.5(a-d) is also shows the general distribution of cracks over the aged flakes (for FD configuration) and no crack formation for HO configuration.

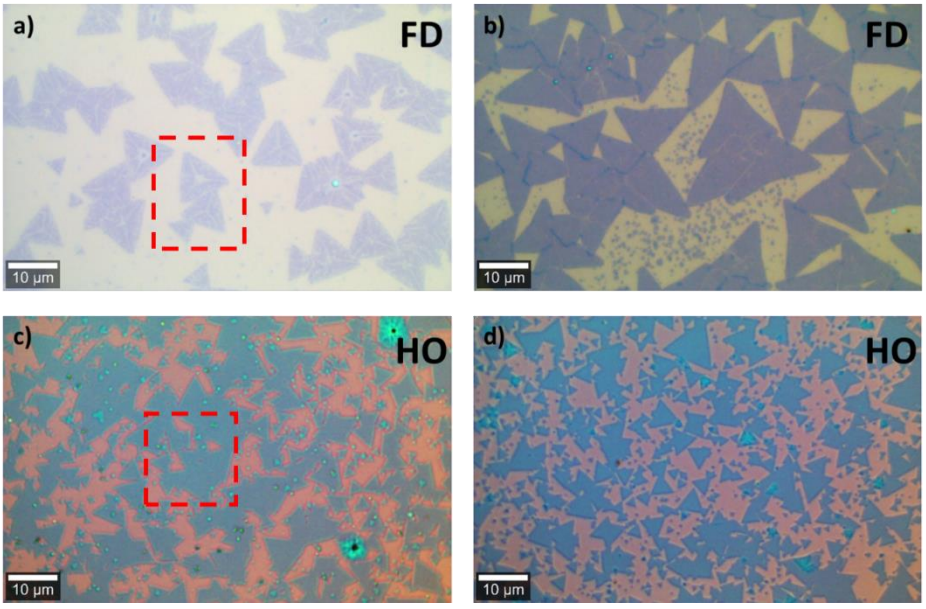

Figure 5.5 *The optical microscope images of the aged (18 months) FD-grown flakes (a) - (b), and 18 months aged HO-grown flakes (c) - (d), The dashed red squares are indicating scanned area for integrated PL maps.*

The integrated PL map of the fresh flakes reveal almost uniform intensity distribution, without any indication of fractures. The small PL intensity variation, specifically at the edges, could be addressed to non-uniform strain due to thermal mismatch between the substrate and MoS_2, as discussed in detail by Liu et al [169]. The integrated PL map of HO grown fresh flakes reveal a uniform intensity distribution. The only difference between the as-grown PL maps of FD and HO samples is HO grown samples has almost one order of magnitude higher PL intensity. Hence, in our study, the integrated PL maps of the as-grown FD and HO grown MoS_2 flakes assert that there is a structural integrity before the aging starts for both of the growth configurations. In Figure 5.3c, the integrated PL map of the 18 months aged FD grown MoS_2 shows regions with excessively quenched PL intensity which is a result of extensive structural aging damage. However, the integrated PL map of HO grown MoS_2 have no regions with PL quenching in addition to no sign of cracking or aging but just decrease in PL intensity. The main difference between two growth configurations is the precursor vapour concentration on the Si/SiO_2 surface during the growth process. The position of the substrate with respect to the MoO_3 precursor will inevitably change the precursor vapour concentration on the growth surface, which can be correlated with the growth rate. In the FD growth scheme, the vapour concentration of the precursors on the growth surface is expected to be higher than in HO growth scheme. Because of the geometry of the FD growth set up (Crucible shape and substrate position creates a small cubic volume with a small inlet and outlet) traps more precursor vapour with respect to HO growth set up. As the concentration of the precursor vapour is high, more growth domains or seeds (nuclei) are expected to form. The comparatively higher number of growth domains and the rather high growth coverage is suggested to cause these structures to coalescence in more defective manner with higher amount of grain boundaries. Cao *et al* mentioned a similar issue as a source of defect formation during growth in their theoretical studies [158, 175-177]. Furthermore, potentially due to higher number of seed formations and resulting higher growth rate, it is observed that the surface coverage of FD grown samples is higher than that of HO grown samples with multilayer to bulk growth zones (Figure 5.6a and 5.6b).

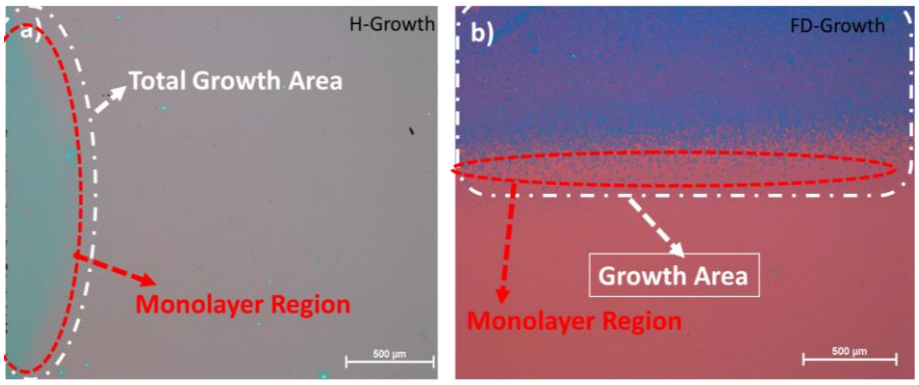

Figure 5.6 *The total growth area of a HO grown sample (a) and FD growth sample is 3 cm x 7 cm so that optical image shows just a quarter of total sample (This growth region contains multilayer and monolayer continuous film region and monolayer flakes)(b).*

Another indication is the size of the obtained flakes where larger flake sizes have been achieved by the FD growth configuration as shown in Figure 5.3, 5.4 and 5.5. Considering the identical growth durations, the FD scheme has a higher growth rate, which presumably is the cause of the higher defect density and the thermal strain due to insufficient relaxation.

5.4. The effect of Stress and Vacancy on Stability of MoS_2

The residual thermal stresses and S vacancies are reported as potential mechanisms that induce aging of the MoS_2 flakes. Our aging resistant HO grown flakes provide an opportunity to determine which mechanism is more effective on the aging of MoS_2 flakes [159, 168]. In order to clarify the effect of S vacancy and stress effect on the oxidation profile of MoS_2, DFT calculations are performed for predicting the oxygen adsorption energy on MoS_2 under stress together with presence of S vacancies. Density functional theory (DFT) is used as implemented in the VASP code[1] with generalized gradient approximation (GGA) within the Perdew-Burke-Ernzerhof (PBE)[2] formulation. The interaction between valence electrons and ionic cores is described by the projector augmented wave (PAW) method[3-4]. 4 x 4 x 1 supercells are used for adsorption calculations. Tensile or compressive strain in xy-plane is introduced by increasing or decreasing ground state lattice vectors and keeping it fixed throughout the corresponding calculations. Moreover, a minimum vacuum spacing of at least 12 Å is preserved by using 20 Å lattice vector in z-direction, to prevent any interaction between the periodic images. During our calculations, 500 eV plane wave energy cutoff and 4 × 4 × 1 k-points sampling grid within the Gamma-centered scheme is used. The convergence criterion for electronic

and ionic relaxations are set as 10^{-6} eV and 10^{-2} eV/ Å, respectively. Furthermore, dissociation energy barriers are calculated by using nudged elastic band (NEB) method[5].

Table 5-1 *Adsorption energy and dissociation energy barrier values of elemental and molecular oxygen on MoS_2 with and without S-vacancy with respect to applied strain.*

Strain (%)	MoS_2 without S-Vacancy			MoS_2 with S-Vacancy		
	E_{ads} O (eV)	E_{ads} O_2 (eV)	E_{diss} (eV)	E_{ads} O (eV)	E_{ads} O_2 (eV)	E_{diss} (eV)
%3 tensile	-0.64	0.00	-	-3.89	-2.39	0.94
%2 tensile	-0.61	0.00	-	-3.90	-2.22	0.94
%1 tensile	-0.59	-0.01	-	-3.89	-2.04	0.93
%0 (w/o strain)	-0.58	-0.03	2.72	-3.88	-1.83	0.92
%1 compressive	-0.54	-0.01	-	-3.85	-1.62	0.90
%2 compressive	-0.52	-0.01	-	-3.80	-1.38	0.88
%3 compressive	-0.51	0.00	-	-3.74	-1.14	0.86

The results of calculations are summarized in Table 5.1. The adsorption energy of elemental O on both pristine MoS_2 surface and S-vacancy slightly increases from compressive strain to tensile strain. On the other hand, the adsorption of molecular O_2 on S-vacancy is largely enhanced by tensile strain while the dissociation energy barriers are very slightly increasing.

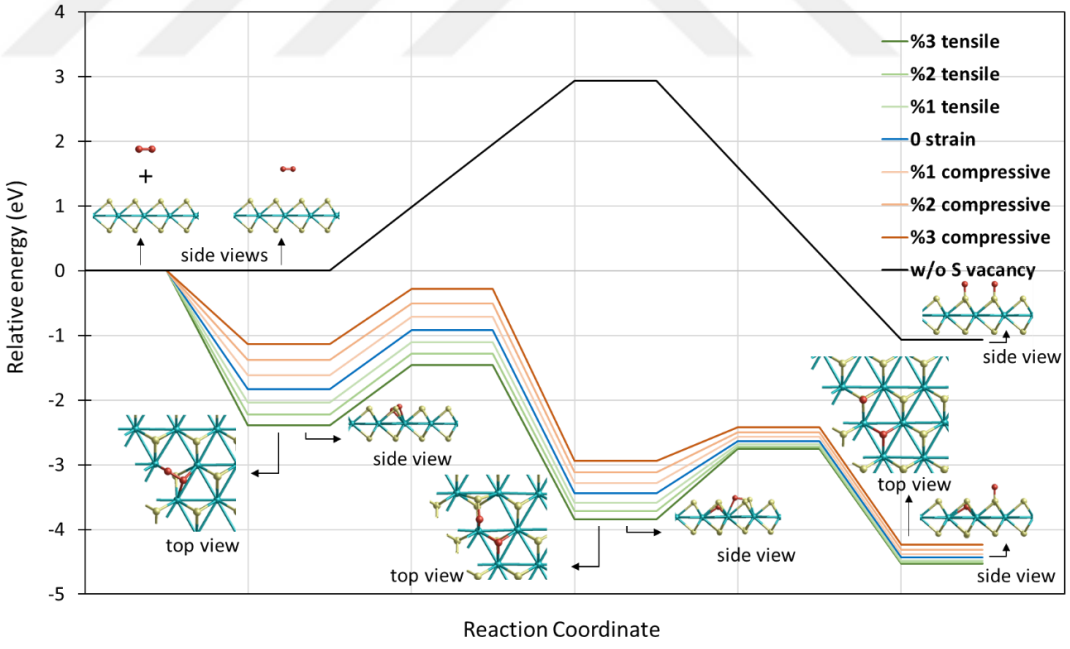

Figure 5.7 *Energy profile of O_2 dissociation on S vacancy of MoS_2 monolayer under strain. Ball and stick structure models indicating the corresponding Oxygen atom positions are given on the energy profile*

As a result, the energy profile of O_2 dissociation in Figure 5.7 implies that strain might stimulate higher oxidation rate. However, since molecular O_2 does not interact at all with

pristine MoS_2 surface and the O_2 dissociation energy barrier is very high (~2.7 eV) on pristine MoS_2 surface, S-vacancy defects are needed for the oxidation. This indicates that the defect density increase occurs probably as a result of higher growth rate (for the FD case) and facilitates oxidation, while the effect of tensile stress on the oxidation behavior is secondary.

5.5. Naturally Aged MoS_2 Flakes Grown by FD and HO CVD growth Configurations

With the aim of further analysis on the aging mechanism and in order to confirm the obtained theoretical and experimental results, we have performed thermal aging tests under ambient conditions for the FD and HO grown MoS_2 by mimicking the natural aging. The thermal aging experiments are implemented on a preheated hot plate at 350 ºC for 5 min in the air. The optical and differential interference contrast (DIC) microscope images of the fresh and thermally aged FD and HO grown MoS_2 are taken from exactly the same region, as shown in Figure 5.8. FD grown individual MoS_2 flakes are continuous and uniform before the thermal aging (Figure 5.8a and 5.8b). DIC microscope image of the FD grown samples before thermal aging confirms the integrity and crack free MoS_2 flakes. After the thermal aging process, the optical microscope images of the same region indicate that cracks are created mainly on the grain boundaries of the structures formed by the combination of triangles (Figure 5.8b). In addition to the cracked structures (through grain boundaries), DIC image also demonstrates voids like damaged regions are created on surface of the triangles after the aging process (Figure 5.8f). The fracture or void formation is observed to be independent of the flake size. On the other hand, for the HO grown MoS_2 case, the DIC and optical microscope images of the MoS_2 structures before and after the thermal aging application indicate no new formations such as cracks or voids, which agrees with the first part of our experimental results. Hence, the HO grown MoS_2 flakes are stable and durable against aging and oxidation.

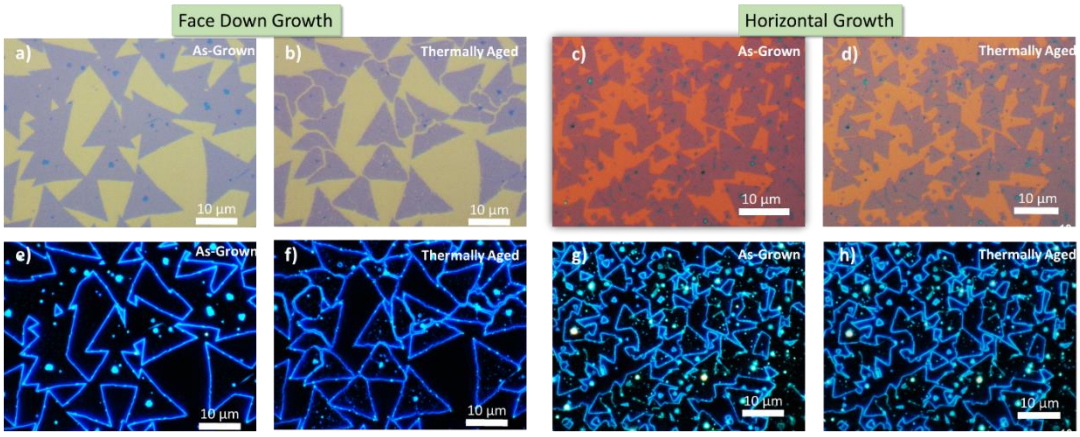

Figure 5.8 *Optical microscope image of as-grown FD-grown flakes before (a) and after (b) thermal aging, optical microscope image of as-grown HO-grown flakes before (c) and after (d) thermal, the DIC microscope image of FD-grown flakes before (e) and after (f) thermal aging, the dark field optical microscope image of HO-grown flakes before (e) and after (f) thermal aging.*

Thermally aged flakes are also characterized by AFM to investigate specifically the cracked regions. The AFM images of aged samples before and after cleaning are shown in Figure 5.9. The size increase in form of local growth on the edges and grain boundaries of aged samples before cleaning is clearly visible (Figure. 5.9a), which is suggestively attributed to organic contaminants or oxidized MoS_2 regions. The before and after cleaning AFM images and line profiles of specific regions on the thermally aged FD grown MoS_2 samples are presented. It is clearly observed that before three solvent cleaning, the thickness of the edges and grain boundaries is relatively high (Fig 5.9a, 5.9b and 5.9d). However, after three solvent cleaning, edges and boundaries are clearly visible. One can speculate that, the deposition on the edges and grain boundaries could be organic contaminants or oxidized MoS_2 regions.

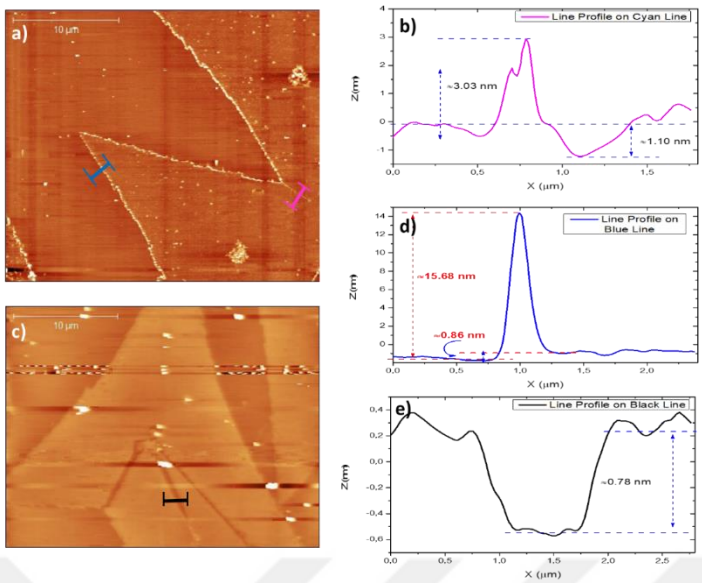

Figure 5.9 *The AFM images of thermally aged, before cleaning (a) and after cleaning (with three solvent cleaning) (c) FD grown MoS_2, the line profiles of cyan (b), blue (d) and black (e) line on AFM images.*

The resistance of the HO grown MoS_2 against aging demonstrated with optical and DIC microscope images is supported by spatially resolved PL maps and central wavelength, statistical analyses of PL central shift and single point PL spectra of FD and HO grown MoS_2 (Figure 5.10). The PL central wavelength and intensity of MoS_2 emission are sensitive to compositional change due to oxidation and the applied stress [169]. Although PL central shift behavior of FD and HO grown MoS_2 are similar, FD grown ones exhibit a larger PL central shift with respect to HO grown ones which can be clearly seen from PL central wavelength maps. In Figure 5.10d and 5.10c, the single PL spectra of before and after thermal aging of HO and FD grown MoS_2 with fitted exciton peaks emphasize the PL central shifts of FD grown flakes. Since the effect of stress is assumed to be secondary according to DFT calculations, these small amounts of shift could be addressed as a result of aging.

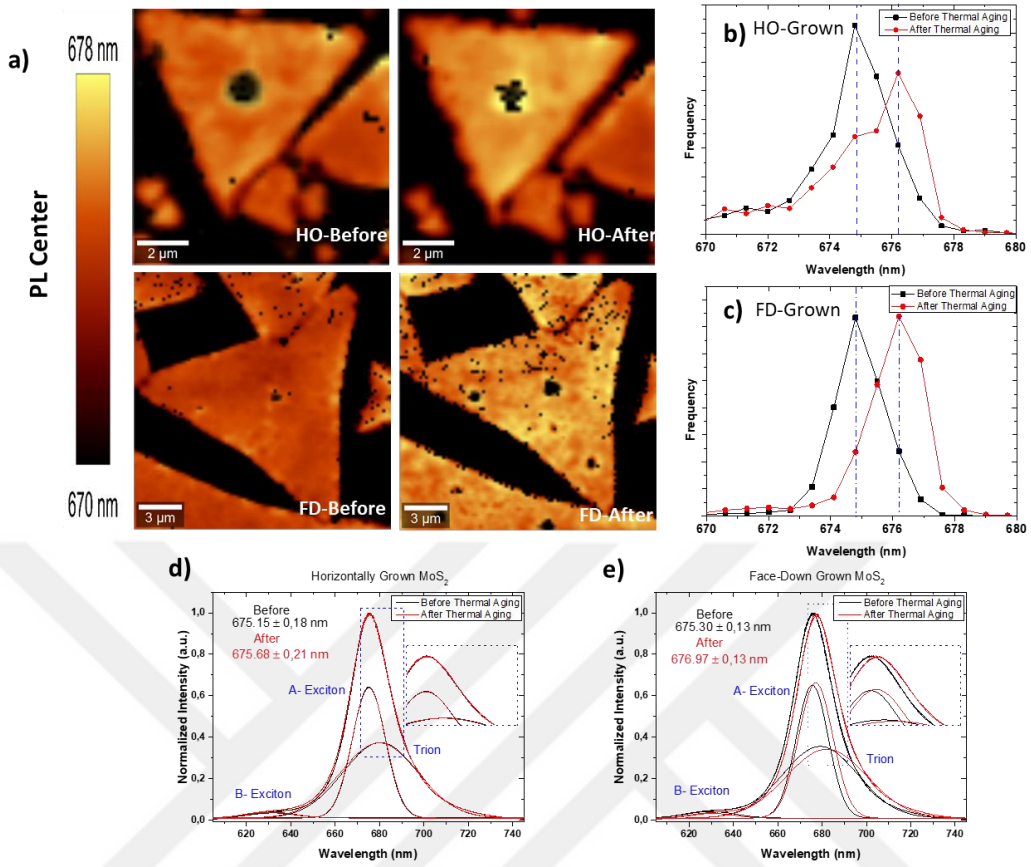

Figure 5.10 *The PL central wavelength maps of FD and HO grown MoS_2 before and after thermal aging test (a), the histogram of the PL central wavelength of HO grown MoS_2 before and after thermal aging test (b), the histogram of the PL central wavelength of FD grown MoS_2 before and after thermal aging test (c), The PL spectra of HO-grown MoS_2 before and after thermal aging (d), The PL spectra of HO-grown MoS_2 before and after thermal aging (e).*

The integrated intensity maps of both samples are given in Figure 5.11. Integrated PL intensity of HO grown flakes shows a larger enhancement with respect to FD grown flakes after thermal aging (Figure 5.11).

The PL enhancement by thermal treatment in the ambient conditions is a known phenomenon which is a result of depletion of excess electrons by physical adsorption of O_2/H_2O molecules or unintentional substrate doping [178, 179]. This phenomenon is a reversible mechanism that can be modulated by changing the measurement atmosphere via vacuum or introducing new gasses [179].

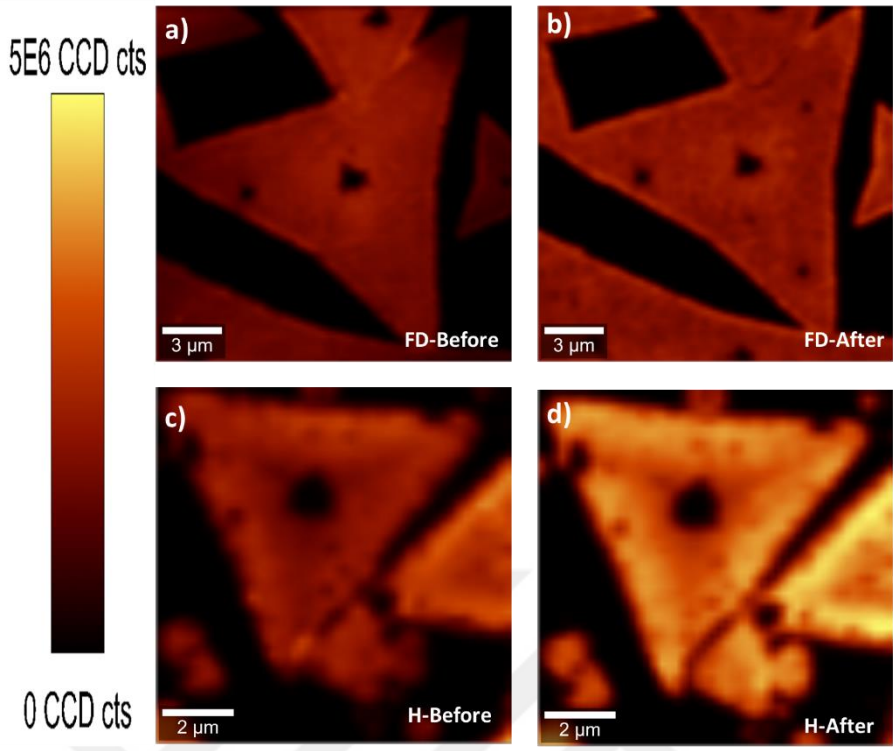

Figure 5.11 *The integrated intensity PL maps of FD and HO grown MoS2 before (a-b) and after (c-d) thermal aging test.*

PL enhancement by thermal treatment occurs at temperatures that are lower than the oxidation or decomposition temperature of MoS_2 with specific treatment durations. After the oxidation temperature or long process times, the PL intensity begins to decrease [179, 180].

5.6. Conclusion

As a conclusion, we observe and demonstrate a clear difference in aging process between the MoS_2 flakes grown under different growth configurations, which brings in relatively different growth rates and hence presumably different defect (S) densities and residual stresses. The difference in growth rates is achieved with the aid of the variation of vapor concentration of the precursors on the growth surface by changing the position of the substrate with respect to precursors while keeping all other growth parameters identical such as heating rates, flow rates of the carrier gases, the amount of precursors. Aging behaviour of the flakes grown with a slower rate are found as aging resistant compared to the flakes grown with a higher growth rate. In order to gain further understanding of the role of strain and S vacancy on aging, we have performed DFT calculations together with controlled aging experiments. Our results indicate that the S

vacancy defects are more effective on the formation of oxidation than the stress effect. Therefore, these results inevitably suggest that S vacancies need to be reduced suggestively by controlling the growth rate, which will improve the long-term stability of MoS_2 monolayers. According to the controlled aging experiments, DFT calculations and spectroscopic measurements, we have proposed a growth method (HO growth) that yields oxidation and moisture resistant MoS_2 flakes durable for more than 18 months at ambient conditions. The effectiveness of proposed method has been also tested and proved by the thermal aging tests.

6. DEVICE PERFORMANCE COMPARISON OF MoS_2 AND WS_2

6.1. Introduction

Two-dimensional (2D) materials era and the 2D material-based electronics have begun with the exploration of the thinnest material, graphene in 2004 [7]. Graphene is the most studied 2D material because of its unique and exceptional mechanical, electrical and optical properties [8, 9]. However, the role of graphene in electronic applications has been limited due to its semi-metallic nature (having zero bandgap) which degrades the current ON/OFF performance of the fabricated electronic devices. 2D transition metal dichalcogenide (TMDCs) family is another widely studied group of 2D materials since the discovery of graphene. The presence of a direct bandgap due to the quantum confinement in 2D TMDCs makes them highly desirable for future electronic and optoelectronic device applications.

Both monolayer MoS_2 and WS_2 have received comparatively more attention because of their outstanding properties. They demonstrate wide direct bandgaps (1.8-2 eV)[181-183], strong photoluminescence (PL) emission [181, 184], thermal and mechanical stability [185] and large area growth ability [156]. According to the theoretical studies, MoS_2 and WS_2 based field effect transistors (FETs) have been estimated to have high current ON/OFF ratios as much as 10^9 and 10^6 and high effective carrier mobilities up to 340 $cm^2V^{-1}s^{-1}$ and 1100 $cm^2V^{-1}s^{-1}$, respectively [186]. Experimental results on MoS_2 and WS_2 FETs also exhibit promising performances, even though they are underperforming compared to the theoretical results. The fabricated MoS_2 and WS_2 based transistors have been shown to operate with high effective carrier mobilities up to 217 $cm^2V^{-1}s^{-1}$ and 60 $cm^2V^{-1}s^{-1}$, high current ON/OFF ratios of ~10^8 and ~10^6 and short channel immunity [10], respectively. The photo detection performance of these devices has also been measured as ≈10^4 AW^{-1} with a response time of 10 s for MoS_2 based photodetectors and ≈10^{-3} AW^{-1} with a response time of several seconds for WS_2 based ones [132, 187].

The mentioned FETs above have been fabricated from exfoliated MoS_2 and WS_2 flakes. On the other hand, the devices fabricated from chemical vapor deposition (CVD) grown flakes have been reported to have lower mobilities and lower current ON/OFF ratios between 0.1 to ≈50 $cm^2V^{-1}s^{-1}$ and ~10^3 to ~10^5 [188], respectively. The observed performance differences between CVD grown and exfoliated flakes are because of the differences between the crystal qualities and the defects induced during CVD process

[189]. The exfoliated MoS_2 and WS_2 have high quality and low defect density but mechanical exfoliation is not a suitable method for industrial scale device fabrication and high-volume manufacturing. Therefore, the studies focusing on CVD grown devices are of crucial importance for future electronics and optoelectronics.

The performance difference between theoretical and experimental results is also due to the surface sensitivity of 2D materials. It is possible that their high surface to volume ratio enables physically adsorbed oxygen (O_2) and water (H_2O) molecules from ambient medium that serves as surface trapped states and affects their charge carrier transport properties [190]. As an evidence of this effect, Ahn *et. al*, reported that the effective carrier mobility of MoS_2 based FETs increased 4 times when the sample is characterized under vacuum conditions [189]. Moreover, Lan *et. al* showed that the photoresponsivity of WS_2 based photodetectors is increased under vacuum or low humidity conditions [187]. As summarized above, since $MoS_2$and WS_2 are very important candidates for future electronic and optoelectronic devices, there have been numerous studies on MoS_2 and WS_2 individually. However, there are few studies focusing on comparative properties of WS_2 and MoS_2 under same growth and characterization conditions.

In this study, we report on the electronic transport and physical properties of MoS_2 and WS_2 based devices where their flakes are grown in the same CVD system, thus enabling a systematic comparison. Electronic transport properties of the fabricated FETs are characterized under the same ambient conditions to measure their relative performances. The electronic transport properties of the fabricated devices are examined comparatively in terms of field effective carrier mobility (μ_{FE}), current ON/OFF ratio and threshold voltages. The FETs of MoS_2 and WS_2 show reasonably high μ_{FE} of 1.45 $cm^2V^{-1}s^{-1}$ and 0.98 $cm^2V^{-1}s^{-1}$, respectively. This indicates comparable electronic properties with exfoliated and CVD grown flake samples. In addition, the photo detecting performance of the fabricated devices is measured and compared.

6.2. CVD Growth and Characterization of MoS_2 and WS_2

The CVD growth of 2D MoS_2 and WS_2 structures is performed in a home-built, dual-zone furnace with a 70 mm horizontal quartz tube at atmospheric pressure. Monolayer MoS_2 and WS_2 flakes are grown by using face-down substrate configuration as described by Ozden et al [155]. The CVD growth of 2D MoS_2 and WS_2 flakes is performed in a home-built, dual-zone furnace with a 70 mm diameter horizontal orientation quartz tube

operated at atmospheric pressure. The growth zone configuration of the set-up is depicted in Figure 6.1a SiO_2/Si substrate is positioned face-down above the MoO_3 or WO_3 precursors. Quartz boats containing the precursors are placed on the quartz plate and therefore are positioned at the center of the quartz tube. Sulfur is placed at the upstream direction of the furnace having 16 cm distance with the metal-oxide precursors. The precursor amounts are kept constant for both MoS_2 and WS_2 growth processes at values of 150 mg for S and 1 mg for MoO_3 and WO_3, respectively. The growth procedure can be summarized as follows: 1 mg of MoO_3 (Sigma Aldrich, 99.5%) and 150 mg of S (Sigma Aldrich, 99.5%) powders are used as precursors and reacted to form MoS_2 flakes at 700 ºC under 400 sccm N_2 flow. Similar to MoS_2 growth configuration, 1 mg of WO_3 (Sigma Aldrich, 99.5%) and 150 mg of S powders have been used as precursors to form WS_2 flakes at 950 ºC, under 95 sccm N_2 and 5 sccm H_2 on SiO_2/Si substrates. An inner one side-sealed quartz tube (2 cm diameter) is used to confine or keep WO_3 vapor on the substrate. The distance between Sulphur and oxide precursors is fixed to 16 cm. The grown structures are analysed by using Witec Alpha 300 R μ-Raman and photoluminescence (PL) spectroscopy system with a Zeiss 50X microscope objective having a numerical aperture (N.A.) of 0.8. A 532 nm CW laser with 1 mW laser power and 0.2 second integration time was used for Raman spectra. The integration time used for the PL measurement was 0.03 second. The AFM measurements were done with Nanomagnetic-ezAFM system.

Figure 6.1b and 6.1c show the optical microcopy images of MoS_2 and WS_2 flakes, respectively. In figure 6.2a and 6.2b Raman finger prints of MoS_2 (E^1_{2g} and A_{1g}) and WS_2 (E′(M), 2LA(M), E′ and A_1) have been identified and deconvoluted using Lorentzian curves to indicate the individual Raman modes [152, 191]. The layer numbers (thickness) of MoS_2 and WS_2 can be identified from Raman shift differences of E and A modes or exact Raman mode positions of materials. The E and A modes Raman shift differences are found to be 21.4 ±0.1 cm^{-1} and 64.5 ±0.2 cm^{-1} and that indicate monolayer MoS_2 and WS_2, respectively [191].

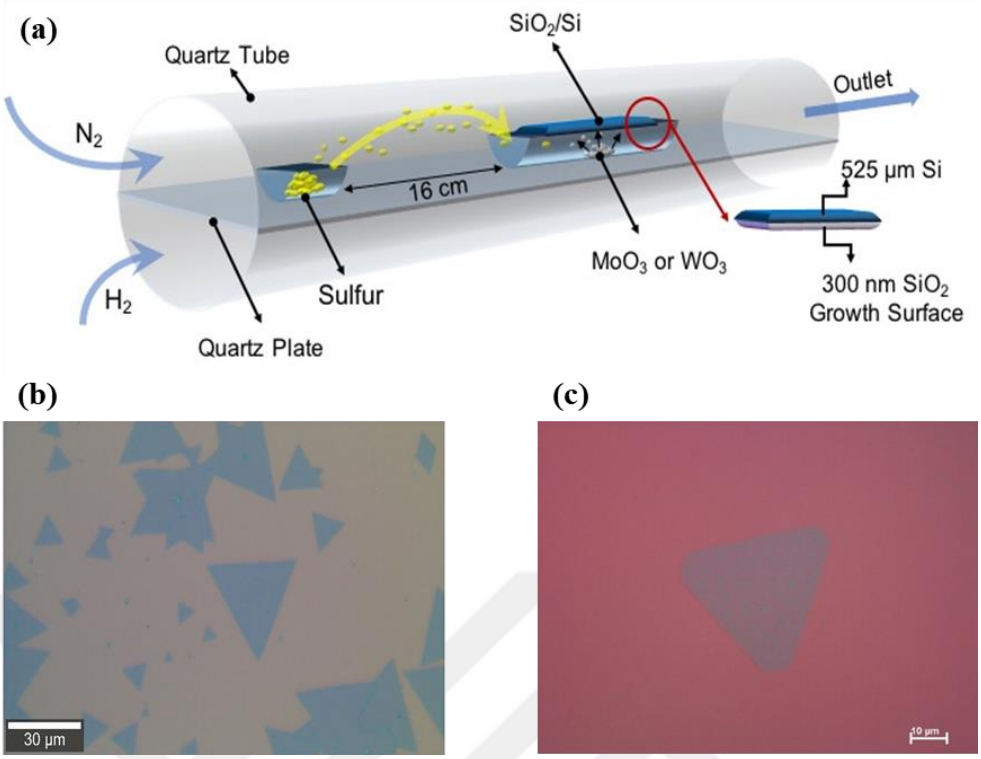

Figure 6.1 *Schematic of the growth of CVD system for MoS_2 and WS_2. The optical images of* ***(b)*** *MoS_2 and* ***(c)*** *WS_2 flakes.*

Typical room temperature PL spectra of monolayer MoS_2 and WS_2 are shown in Figure 6.2c and 6.2d where measurement is performed by using a 2.33 eV (532 nm) excitation wavelength laser at room temperature. The PL spectra of MoS_2 and WS_2 structures consist of three different radiative recombination mechanisms that are as attributed to exciton (A and B), trion (A^-) and biexciton (AA) [78, 192].

The measured PL spectra of materials are deconvoluted to three Gaussian curves which represent A (or B), A^- and AA. The centers of A-exciton, B-exciton and AA-trion which are represented in Figure 6.2c have been extracted as 1.81 eV, 1.92 eV and 1.79 eV for MoS_2, respectively. The intensity of A-exciton is very high with respect to the intensity of B-exciton, which is an indication of the monolayer MoS_2. In Figure 6.2d the PL spectra of WS_2 with A^0-neutral exciton, A^--trion and AA-biexciton is shown. The centers of A^0, A^- and AA are at 1.96 eV, 1.95 eV and 1.85 eV, respectively. Because of the excitation wavelength (2.33 eV) it is not possible to determine the B-exciton of WS_2 which lies around 2.4 eV [192].

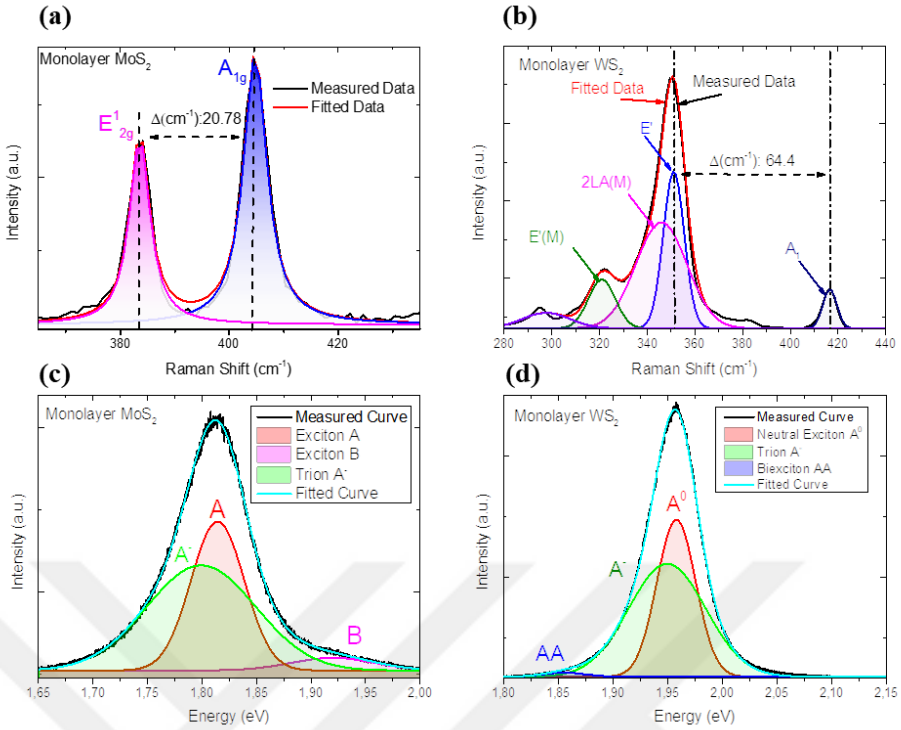

Figure 6.2 *Raman spectra with Lorentzian fits of (a) MoS_2 and (b) WS_2, PL spectra with Gaussian fits of (c) MoS_2 and (d) WS_2.*

The PL spectra of WS_2 and MoS_2 are very sensitive to doping levels or defect densities. In other words, the integrated intensity ratio of trion (I_X) to exciton (I_{X^-}) peaks gives information about the defect densities, which is due to the relationship between charge carrier density and quasi particle concentration that are based on mass action law [193-195].

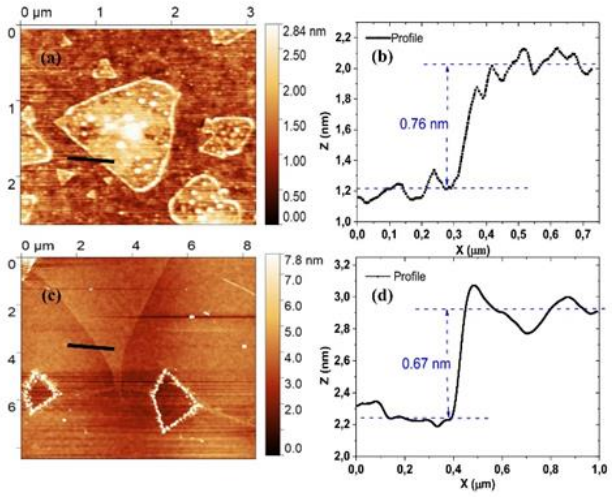

Figure 6.3 *(a) 3 μm x 3 μm AFM image of MoS_2 flakes and (b) the height profile of MoS_2 flake taken from black line on (a), (c) 8 μm x 8 μm AFM image of WS_2 flake and (d) the height profile from black line on AFM image (c).*

In this manner, (I_X-/I_X) has been extracted from over 500 fitted spectra and found to be 0.7 and 0.8 for MoS_2 and WS_2, respectively. MoS_2 and WS_2 are found to have similar defect densities.

Figure 6.3a shows 3 µm × 2.5 µm AFM image of MoS_2 triangles which indicate a maximum height of 2.4 nm caused by contamination. The step height profile of MoS_2 triangle is presented in Figure 6.3b where the thickness of the flake is determined as one layer (0.76 nm). The 8 µm × 7 µm AFM image of WS_2 presented in Figure 6.3c shows a uniform flake surface without any contamination. In Figure 6.3d the structure of WS_2 flake is also determined as a monolayer (0.67 nm).

6.3. Electrical and Opto-Electrical Characterizations

The cross-sectional diagram of the fabricated devices with electrical connections is demonstrated in Figure 6.4a. FETs are fabricated on a 300 nm thick gate oxide layer on top of a highly doped 525 nm thick Si substrate. Gate bias is applied to the Si substrate to modulate our FETs. In order to make a meaningful comparison, both MoS_2 and WS_2 based devices are designed with the same active region channel length determined as L_{CH}=4 µm. Electrical measurement of all the devices are conducted in ambient atmosphere, under dark and illuminated conditions at room temperature.

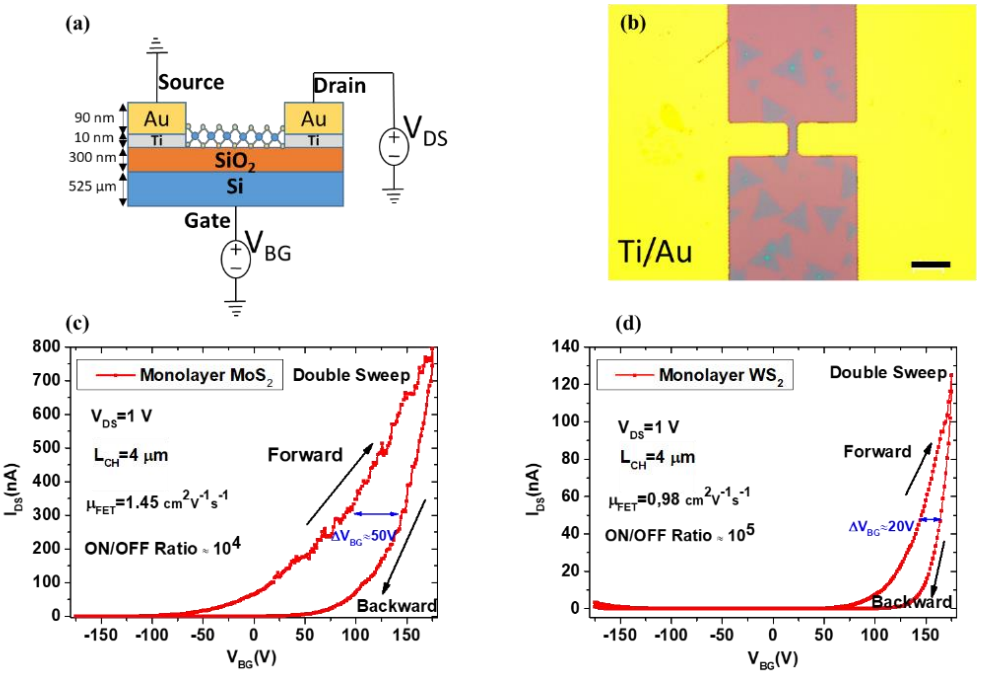

Figure 6.4 ***(a)*** *The cross-sectional view of the device structure* ***(b)*** *the optical image of a typical device (scale 10 µm), the transfer curves (I_{DS}-V_{BG}) of* ***(c)*** *MoS_2 and* ***(d)*** *WS_2.*

According to the measured transfer curves, MoS_2 and WS_2 based FETs display n-type behavior. The threshold voltages (V_{TH}) are determined from the linear regime of the on-state conduction. The tangent line with maximum slope to I_{DS}-V_{BG} curve at the peak transconductance (g_m) is linearly extrapolated to V_{BG} (axis) to extract V_{TH}. The extracted V_{TH} values of MoS_2 and WS_2 FETs are ~ 41 V and ~ 124 V, respectively. According to transfer curves the devices have a low gate modulation efficiency. Field effect mobilities are calculated from estimated transconductance $g_m = \partial I_{DS}/\partial V_{BG}$ using:

$$\mu_{FE} = \frac{L_{CH}}{W_{CH}} \frac{1}{V_{DS} C_g} \frac{\partial I_{DS}}{\partial V_{BG}} \quad (\mathrm{cm^2V^{-1}s^{-1}}) \qquad (1)$$

Where μ_{FE} is the field effective carrier mobility, I_{DS} is drain-source current, L_{CH}/W_{CH} is the ratio of channel length to channel width, V_{DS} is bias voltage and C_g is the gate capacitance per unit area. $C_g = \varepsilon_g/t_g$. ε_g and t_g is the dielectric constant and the thickness of gate oxide, respectively. The FETs of MoS_2 and WS_2 show reasonably high μ_{FE} of 1.45 $cm^2V^{-1}s^{-1}$ and 0.98 $cm^2V^{-1}s^{-1}$, indicating comparable electronic performance with previously reported CVD grown samples[103, 189]. Although the theoretical estimation addresses a higher mobility for WS_2 based devices, our MoS_2 based FETs show a better performance in terms of mobility.

The contact resistance effect is not accounted for mobility estimation which may result in degraded mobilities A dedicated contact resistance measurement is expected to increase the value of field effect mobility around ten percent [196]. In addition to that, the gate voltage sweep modulates the number of carrier electron energy levels. These levels are filled at the electrode-active region intersection position which is the junction point. That modulation depends on capacitive coupling between the gate electrode and active region [78]. The efficiency of this capacitive coupling depends strongly on the quality of the gate oxide, in other words dielectric constant of the gate oxide. Since the devices are fabricated on as-grown substrates to avoid any contamination from the transfer process, the substrates have been exposed to very high growth temperatures like 700 ºC and 950 ºC. These high temperatures may degrade the capacitive coupling efficiency of gate oxide by inducing defects during growth that may also cause degradation in effective carrier mobility and threshold voltages. The subthreshold swing (SS) values of MoS_2 and WS_2 devices are inferred to be comparatively high according to the ones reported in the literature, 19.59 V/decade and 14.66 V/decade, respectively [197]. Furthermore, the

current ON/OFF ratios of devices are obtained as ~10^4 and ~10^5 for MoS_2 and WS_2, respectively. Both devices show rather high ON/OFF ratios performances.

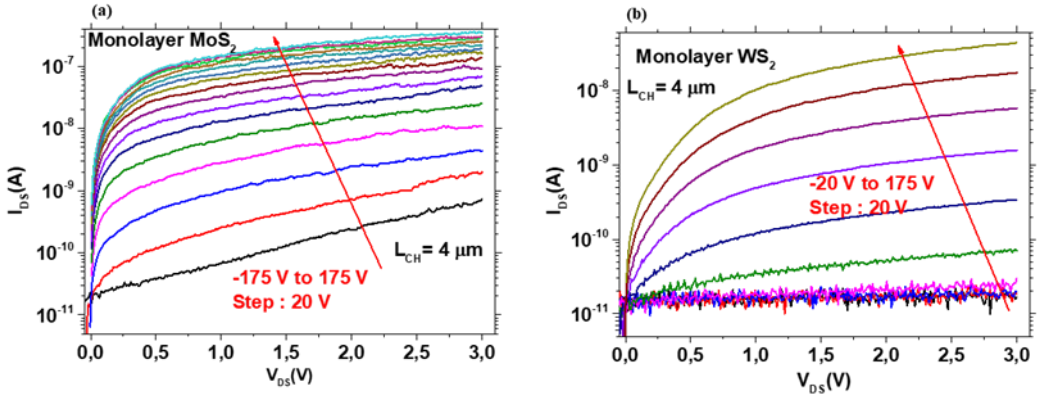

Figure 6.5 *The output characteristic curves (I_{DS}-V_{DS}) of* ***(a)*** *MoS_2 and* ***(b)****.WS_2.*

Figure 6.5a and 6.5b represent the characteristic curves (I_{DS}-V_{DS}) of MoS_2 and WS_2 based devices when the gate modulation voltage changes from V_{BG}=-20 V to V_{BG}=175 V with a step rate of 20 V. The V_{DS} voltage is swept from 0 V to 3 V to show the operation regions of the FETs. The saturation region of both types of the devices can be defined as the region where $V_{GS} \geq V_{TH}$ and $V_{DS} \geq 0.5\,V$. The linear region (ohmic region) is in the range $V_{GS} \geq V_{TH}$ and $0\,V \leq V_{DS} \leq 0.5\,V$. The maximum saturation currents (I_{DSS}) have been measured as 340 nA and 42 nA for MoS_2 and WS_2 FETs, respectively. Two device types show similar characteristic curve behaviors except that MoS_2 has a higher I_{DSS} current and WS_2 operates with a higher gate modulation response when device is in the saturated operation region.

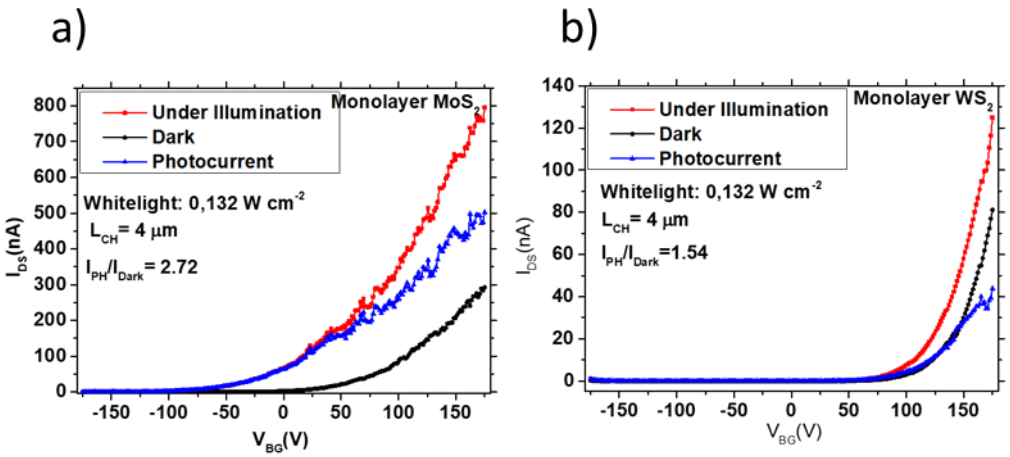

Figure 6.6 *The transfer curves (I_{DS}-V_{DS}) of* ***(a)*** *MoS_2 and* ***(b)****.WS_2 under dark and illumination conditions with plotted photocurrent (I_{PH}).*

An important application area of 2D MoS_2 and WS_2 structures is optoelectronic where they are used as active layers of photodetectors, phototransistors and solar cells [142, 187, 198]. In Figure 6.6a and 6.6b the photo-responsive characteristics of MoS_2 and WS_2 based devices under dark and illuminated conditions are presented. A white light with an intensity of $0.132\ Wcm^{-2}$ has been used as illumination source. Photocurrent is defined as the difference between the current under illumination (I_{II}) and the dark current (I_D) as in (2).

$$I_{PH} = I_{II} - I_D \text{ (A)} \qquad (2)$$

As can be seen from Figure 6.6, both devices are able to modulate the photocurrent according to the gate voltage. However, the modulation efficiency and maximum photocurrent of the MoS_2 based device is higher than that of WS_2 and can be originating from characterizing the devices under ambient conditions. Lan *et. al*, reported that WS_2 is very sensitive to the measurement medium. They demonstrate a significant increase in photoresponsivity of WS_2 based photodetectors in vacuum with respect to measured samples in ambient atmosphere [187]. One can speculate that the surface sensitivity of WS_2 is higher than MoS_2.

As a second metric, the ratio of maximum illuminated current to maximum dark current has been estimated as 2.72 and 1.54 for MoS_2 and WS_2, respectively, which again indicates that the MoS_2 based FETs have a higher sensitivity. Another common benchmark in optical performance measurements is the responsivity (R) which is measured to evaluate the photodetector performance and it is defined as;

$$R = \frac{I_{PH}}{\emptyset} \text{ (AW}^{-1}\text{)} \qquad (3)$$

Where, I_{PH} is the photo current and $\emptyset$ is irradiation intensity. The state of art responsivity values of 2D MoS_2 and WS_2 are between 1.1×10^{-3} AW^{-1} to 10^4 AW^{-1} and 9.2×10^{-5} AW^{-1} to 1.88×10^{-2} AW^{-1}, respectively for visible irradiation [102, 132, 144, 187, 199, 200]. The photoresponsivity of the devices are estimated to be considerably high according to state of the art as 14 AW^{-1} and 1.3 AW^{-1} for MoS_2 and WS_2, respectively [201].

Table 6-1 *The photodetector performance results of MoS_2 and WS_2 devices*

	MoS_2	WS_2
Current ON/OFF Ratio	~10^4	~10^5
Mobility μ_{FE} *(*$cm^2V^{-1}s^{-1}$*)*	~1.45	~0.98
Threshold Voltage (V)	~41	~124
Hysteresis range (V)	~50	~20
Responsivity R (AW^{-1}*)*	~14	~1.3

6.4. Conclusion

In summary, we report on the transport and physical properties of monolayer MoS_2 and WS_2 based devices of which the active materials are grown in the same CVD system, fabricated with optical lithography and characterized under the same ambient conditions to understand their comparative performance. The back-gated, CVD grown MoS_2 based devices in ambient conditions without any encapsulation and doping process show higher effective carrier mobility, lower threshold voltage and higher photoresponsivity which are very important for high performance transistors and optoelectronic applications. On the other hand, WS_2 based devices which have the same configuration and measurement system as the MoS_2 based ones, exhibit high current ON/OFF ratio and low hysteresis behavior suggestively due to the lower density of the trap states between the dielectric material and WS_2 where this low hysteresis behavior is critical for electronic applications. Theoretical research studies estimate that WS_2 based FETs and photodetectors should present a superior performance. However, the photoresponsivity of the MoS_2 based devices (photodetectors) are unexpectedly found to be operating with a better performance than the WS_2 based devices at ambient atmosphere and temperature. The results suggest that MoS_2 based FET devices are more promising compared to WS_2 based ones under ambient conditions without any encapsulation, because 2D WS_2 structures are more sensitive to the ambient conditions with respect to 2D MoS_2 structures.

7. SENSITIZED MoS_2 PHOTOTRANSISTOR

7.1. Introduction

As mentioned in previous chapters, graphene and 2D materials beyond graphene has spectacular properties and applications. Among 2D materials, layered transition metal dichalcogenides (TMDs) semiconductors (*e.g.,* MoS_2 and WS_2) have shown promising capability in optoelectronic applications, thanks to their direct electronic band structures. For instance, semiconducting 2D TMDs crystals including MoS_2 and WS_2 demonstrate strong light-matter interaction accompanied with large excitonic binding energy and strong oscillator strength[202]. In addition, the tunable bandgaps of these materials using external electric field or mechanical strain[203] and their gate dependent photoelectronic responsivity makes them promising material platform for photodetectors[204, 205]and photovoltaics[206].

In particular, a single layer of MoS_2 exhibits an absorption coefficient of $\alpha = 1 - 1.5 \times 10^6$, which results in absorption of approximately 10% of the normal incident light at the excitonic features (~620 nm and ~670 nm)[207, 208]. Besides, a new class of semiconductors with their quasi-2D structure, colloidal semiconductor quantum wells (CQWs), also commonly known as colloidal nanoplatelets (NPLs), have been emerged as a unique class of atomically flat semiconductor nanocrystals[209]. Owing to tight quantum mechanical confinement in only vertical direction, CQWs exhibit favorable optical properties including narrow photoluminescence (PL) emission spectra[210, 211], large absorption cross-section[211-213] and giant oscillator strength[212, 213]. These attractive properties make them versatile and promising light-generating[212, 214] and -harvesting[215] materials.

Specifically, phototransistor of MoS_2 showed the responsivity performance in the order of $\sim 10^4 AW^{-1}$ at low excitation intensities[144, 199, 216]. On the other hand, the ultrathin thickness of TMDs 2D semiconductors results in limited optical absorption of incident light, which hinders their photodetection performances. To address this issue, lots of efforts have already been conducted including surface interface engineering[217], novel hybrid structures[218] and combining these materials with an external light absorber layer[219, 220]. The latter one leads to enhance the photocurrent generation *via* charge transfer or non-radiative energy transfer (NRET) mechanisms. Up to now,

numbers of efficient absorber layer have been used including graphene[221-223], colloidal quantum dots (CQDs)[154, 224], organic dyes[219], WS_2[225], ZnO [220] and p-type MoS_2[218]. However, to the best of our knowledge, the combination of CQWs and MoS_2 (CQWs-MoS_2) have not been considered to enhance the photocurrent. Although, owing to their atomically flat geometries, this hybrid offers highly strong layer-to-layer dipole-dipole coupling[226] , which one would expected to achieve more efficient photocurrent enhancement compared to any other possible hybrid[226]. The main mechanism of the photocurrent enhancement in CQW-MoS_2 hybrid is the potential non-radiatively transfer of the photogenerated excitons (electron–hole pairs) *via* Förster resonance energy transfer (FRET), from CQWs (donor) to MoS_2 (acceptor).

FRET is a near-field electromagnetic dipole–dipole coupling process where an oscillating dipole in the donor specie induces a dipole in the acceptor specie [227], and the excitation energy of the donor is non-radiatively transferred to the acceptor[226]. The efficiency and rate of FRET process essentially depends on the distance between acceptor and donor, the spectral overlap between the PL emission and the absorption spectra of the donor and acceptor, correspondingly, and geometry of the donor[226] and acceptor[145, 227, 228]. The effectiveness of the FRET on light-harvesting and -detecting applications have previously been shown. For instance, Taghipour *et al*. previously reported near-unity efficient of FRET (i.e., 99.88%) along with an ultrafast energy transfer (ET) of ~ 268 ns^{-1} from CdSe/CdS core/crown CQWs to the single layer of MoS_2[226]. This study is an obvious indicator of the promising potential of CdSe/CdS-MoS_2 or more general CQWs-TMDs in photodetection/sensing applications.

In this study, we report FRET-assisted enhancement in photodetection performance of MoS_2 phototransistors sensitized by CQWs. In particular, an ensemble thin film of CdSe/CdS core/crown CQWs was utilized as a sensitizer layer on top MoS_2. Here we systematically study the photodetection performance of hybrid system and we obtained ~11-fold of photoresponsivity and 10-fold of specific Detectivity (D*) enhancement at the irradiation of 1 μW. The main mechanism responsible to this photoresponsivity enhancement was revealed to be FRET process by systematic time-resolved fluorescence (TRF) spectroscopy and electronic transport measurements of the devices under dark and illuminated conditions. We achieved a FRET efficiency of 97.84% along with a fast ET rate of 21.26 ns^{-1}, indicting an ultra-efficient transferring of exciton from CQWs to

monolayer of MoS_2. To understand the mechanism that underlay the photocurrent enhancement in detail and effect of FRET process from CQWs to MoS_2, systematic illumination power-dependent transport measurements and analysis were accomplished. Consequently, we found out that the ET from CQWs to MoS_2 layer is also coupled by traps states of MoS_2 and results an increase in the effect of photogating.

7.2. Experimental Methods

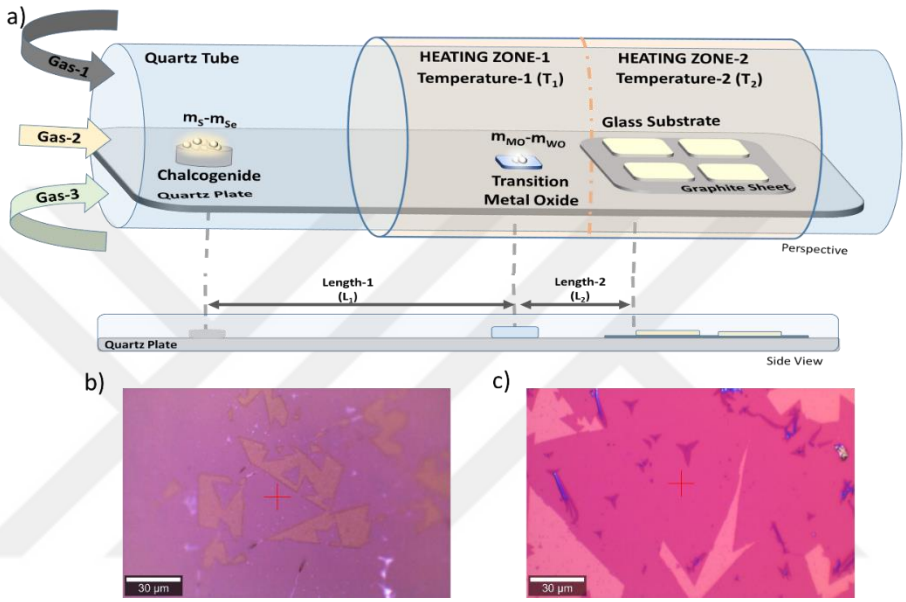

Figure 7.1 *The CVD growth scheme of MoS_2 on microscope cover slip glass (a). The optical microscope images of MoS2 on as-grown glass (SiO_2) substrate (b) and on Al_2O_3/Si substrate.*

The experimental methods and techniques are summarized as follow;

CVD Growth Method: MoS_2 is one the most studied member of 2D materials and TMDs family. Various growth methods have been utilized for high quality and large area growth of MoS_2 including from cost-effective chemical vapor deposition (CVD) setups to more complicated metal-organic chemical vapor deposition (MOCVD) systems[164]. However, growth mechanism of MoS_2 and other TMDs is not fully perceived yet. The usage of glass (soda lime glass) substrates in CVD system has been shown to be promising for the purpose of large area and high quality monolayer MoS_2 growth[61]. Soda lime glass contains Na+ ions, catalyzes the growth of large sized and oriented monolayer TMDCs flakes[167]. So that the glass with efficient Na concentration which is the microscope coverslips, is chosen as growth substrate in this study. The growth scheme of the home-build CVD system is presented in Figure 7.1a. The growth parameters can be summarized as follow; the weight of transition metal oxide (m_{Mo} ve m_{WO}) and

chalcogenides (m_S and m_{Se}) precursors, the distance between two precursors (L_1) and the distance between transition metal oxide and growth substrates (L_2), the temperatures of precursors and substrates (T_1 and T_2) and the flow rates of N_2, Ar ve H_2' carrier gases. The optimized CVD parameters for large area and monolayer MoS_2 growth on glass are as follow; m_{Mo}: 1 mg, m_S: 300 mg, L_1: 12 cm, L_2: 4 cm, T_1: 150 °C, T_2: 750 °C and 20 sccm of N_2. The optical microscope images of monolayer MoS_2 on glass and Al_2O_3 substrates are shown in Figure 7.1b and 7.1c, respectively. The monolayer structure of grown flakes is clearly visible from the images. The single point Raman and PL spectra of as-grown and transferred MoS_2 are represented in the manuscript Figure 7.2c.

Raman and PL Measurements: The single point Raman and PL spectra of as-grown and transferred MoS_2 are analysed by using Witec Alpha 300 R μ-Raman and photoluminescence (PL) spectroscopy system with a Zeiss 50X microscope objective having a numerical aperture (N.A.) of 0.8. A 532 nm CW laser with 1 mW laser power and 0.2 second integration time was used for Raman spectra. The integration time used for the PL measurement was 0.03 second.

CQWs Preparation: The CdSeS/ZnS CQWs (0.15 mg/mL) in hexane solution were synthesized according to previous work by Taghipour *et al* [226]. The CQW/Poly(methyl methacrylate) (PMMA) solution were prepared by dispersing 12.5 μL of each stock solution of QDs in 500 μL of 0.1% wt. PMMA in hexane. The CQWS were dispersed in PMMA solutions by sonication for ~1 min.

Device Fabrication and Opto-electrical Measurement: Source and drain electrodes are firstly patterned by optical lithography and 90 nm of Au is deposited on top of 10 nm Ti by thermal evaporation. After the fabrication process, all devices are baked on a hot plate for 10 minutes at 110 ºC to remove any solvents introduced during the fabrication. Highly doped n-type 500 μm–thick silicon wafer (1-10 Ω.cm) with 44 nm Al_2O_3 (ALD grown) dielectric layer is used as the back-gate electrode and gate dielectric, respectively. The electronic transfer characteristics of the fabricated MoS_2-Only and MoS2-CQWs devices are measured at room temperature under ambient conditions by a grounded probe station with a Keysight B1500A semiconductor device parameter analyzer. The photo-excited measurements were done with a 375 nm pulsed laser in continuous wave mode (CW) with variable power intensity.

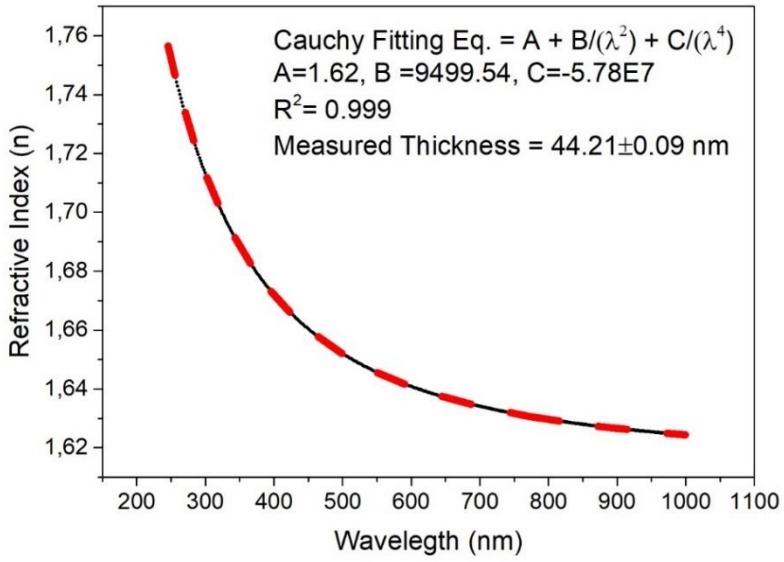

Figure 7.2 *The result of spectroscopic ellipsometer measurement with Cauchy fitting curve for thickness estimation.*

The ALD growth of Al_2O_3 as a high- κ dielectric layer and spectroscopic ellipsometer measurement of grown layer: Atomic Layer Deposition (ALD) (Beneq TFS200) technique is used to grow Al_2O_3 layers using Trimethylaluminum (TMA) and de-ionized water (H_2O) as precursors of Al and O, respectively. Continuously flowing high pure N_2 gas is used as a carrier and purge gas, while during precursor carrying and pumping processes. During the growth process, the N_2 flow rate is 300 sccm. Growth temperature is 300 °C. The substrates used for growth are 525 µm thick p-type Si (100) wafers with a resistivity of 20-40 ohm/cm. Thickness and refractive index of Al_2O_3 layers are measured by spectroscopic ellipsometer as shown in Figure 7.2, the Cauchy equation, which is based on the variation of wavelength according to refractive index, was measured by fitting the measurement data, and the thickness and refractive index were measured. The correlation coefficient (R2) of the fitting is obtained as a very high value of 0.999 as proof of the accuracy of the measurement is high.

7.3. The Characterization of CVD-Grown MoS_2 and CQWs and MoS_2-CQWs Formations

Figure 7.3a depicts a schematic illustration of CdSe/CdS-MoS_2 (CQWs-TMD) phototransistor. Here in, at the bottom layer, a single layer of MoS_2 flakes were grown on a standard microscope coverslip glass substrate with a very high monolayer coverage rate

by chemical vapor deposition (CVD) method (See section 7.1 for details) [61]. Then, the MoS_2 flakes on glass substrate were transferred to Al_2O_3/Si substrate through a wet and etching-free transfer method. To do so, deionized (DI) water was employed to lift MoS_2 layer from glass substrate with the aid of poly (methyl methacrylate) (PMMA) as a support layer. After that, MoS_2/PMMA sample was placed on top of Al_2O_3/Si substrate at 70 ºC for 3 minutes for adhesion of MoS_2/PMMA to the substrate. Then the PMMA was dissolved in hot acetone for 2 hours. Consequently, a high-κ dielectric material of Al_2O_3 was chosen as gate oxide material, where a thin film layer of Al_2O_3 (~ 44 nm) was deposited on top of Si wafer *via* atomic layer deposition technique (ALD), which performed as a back-gate contact. The optical microscope image of the fabricated photodetector along with source and drain contacts are shown in Figure 7.3b. As can be seen in Figure 7.3b, the channel width of the device is 8 μm.

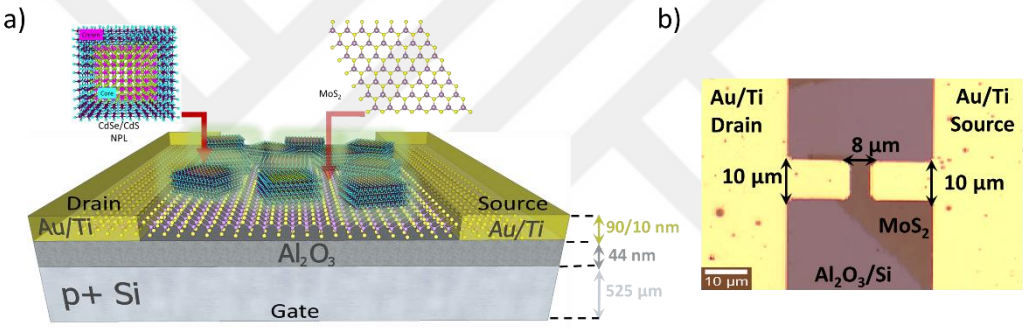

Figure 7.3 *(a) The schematic illustration of CQWs-MoS_2 hybrid phototransistor. (b) The optical microscope image of the fabricated device with Au/Ti metal contacts along with the dimensions.*

To verify single layer formation of MoS_2 triangle flakes before and after of the transfer process, we utilized Raman and photoluminescence (PL) spectroscopy techniques. As a result, Raman spectra of MoS_2 flakes on glass (before transfer) and Al_2O_3/Si (after transfer) and the deconvoluted Raman modes (E^1_{2g} and A_{1g}) using Lorentzian curves are exhibited in Figure 7.4a. The difference between E^1_{2g} and A_{1g} Raman mode positions of MoS_2 was employed to determine the thickness of the grown layer, which was found to be 19.3 ± 0.4 and $18.5 \pm 0.4\ cm^{-1}$ for before and after transfer samples, respectively, indicating monolayer MoS_2 flakes in both case[152].

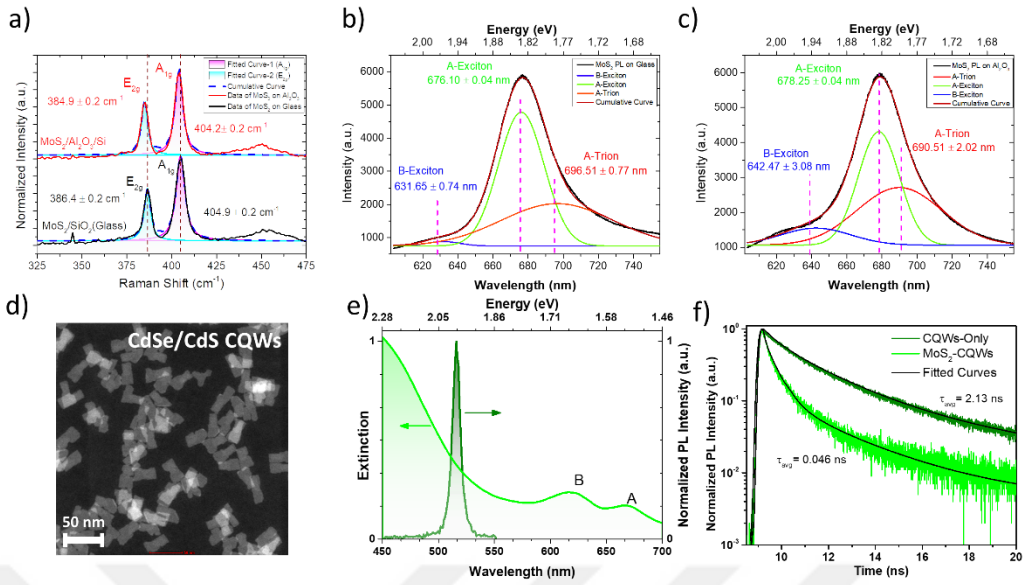

Figure 7.4 *(a) The Raman spectra of monolayer as-grown MoS_2 on glass substrate and transferred on Al_2O_3 along with deconvoluted Raman modes. (b) The photoluminescence spectra of MoS_2 on glass and (c) on AL_2O_3 with excitonic species: A- and B-excitons and A-trion. (d) High-angle annular dark field transmission electron microscopy image of the CQWs. (e) Normalized photoluminescence of the 4 ML CdSe/CdS core/crown CQWs (donor) and UV−vis absorption spectrum of the MoS_2 triangular monolayer flakes (acceptor). (f) Photoluminescence decay curves of the solid films of the CQWs-MoS_2 assembly and CQWs-only. The solid black lines represent the fits of the curves.*

Typical room temperature PL spectra of monolayer MoS_2 on the glass and Al_2O_3/Si are shown in Figure 7.4b and 7.4c, correspondingly[182]. The PL spectra of both samples were deconvoluted to the excitonic features of MoS_2 which called as A- and B-exciton and A-trion peaks, by employing Gaussian curves[229]. The center wavelengths of A-exciton, B-exciton and A-trion were found as $\sim 676\ nm$, $\sim 632\ nm$ and $\sim 697\ nm$ for MoS_2 on grown substrate (glass) and $\sim 678\ nm$, $\sim 642\ nm$, and $\sim 691\ nm$ for MoS_2 on transferred substrate (Al_2O_3/Si), correspondingly. Here, as can be seen in Figure 7.4c, A-trion intensity is increased after transfer procedure which can be attributed to the defects through the transfer procedure. Since, PL characteristics of MoS_2 are very sensitive to the doping levels and defect densities. Particularly, the integrated intensity ratio of A-trion ($I_{A\text{-trion}}$) to A-exciton ($I_{A\text{-exciton}}$) emission are informative about the defect densities, which is based on mass action law due to the relationship between charge carrier density and quasi particle concentration[195]. In addition, due to the induced defects in the transfer procedure, the center wavelength of A-trion peak was blue-shifted while no significant intensity or center wavelength variation occurred for A-exciton[195].

Later on, dilute solution of CdSe/CdS core/crown CQWs (0.15 mg/mL CQWs/hexane diluted in 0.1% hexane/PMMA) was uniformly spin-coated onto the fabricated devices. The ensemble thin film of CdSe/CdS core/crown CQWs acts as an efficient layer of exciton donating, while monolayer of MoS_2 at the bottom layer acting as an exciton sinking layer. Figure 7.4e shows the spectral overlap between the PL spectrum of the donor (CdSe/CdS core/crown CQWs) and absorption spectra of the acceptor (MoS_2, TMD). The central wavelength of CQWs is at 518 nm with an ultra-narrow full-width half maximum of 8 nm and the excitonic features of MoS_2, B-exciton and A-exciton peaks, are around 630 nm and 670 nm, respectively. To investigate luminescence characteristics of CQWs in hybrid of CdSe/CdS-MoS_2 (CQWs-TMD, donor-acceptor pair), we employed time-resolved fluorescence (TRF) spectroscopy. To do so, we recorded the PL decay curve of the donor band-edge emission (at 518 nm) for different cases which are shown in Figure 7.4f. Here, the only CQWs sample, in which only CQWs (0.15 mg/mL CQWs/hexane diluted in 0.1% hexane/PMMA) deposited on a precleaned quartz substrate, which acts as reference sample where the amplitude-averaged PL lifetime corresponds to 2.13 ns. Consequently, as shown in Figure 7.4f, in the presence of monolayer of MoS_2 (i.e., acceptor), CQWs on MoS_2 sample, the PL decay kinetics of donor is significantly altered and becomes faster which reaches to 46 ps, indicating a new channel is opened up for the relaxation of the carriers in CQWs. This tarnation can be ascribed to Förster resonance ET (FRET) or charge transfer process.[226] However, in our structure, the charge transfer is ineffective owing to passivation of CQWs with a nonaromatic ligand of oleic acid, which is in consistent with previous experimental studies [226]. If PL lifetime of CQWs (donor) in absence of MoS_2 (acceptor) is τ_D, and the lifetime of CQWs on MoS_2 (donor-acceptor pair) is τ_{DA}, the FRET efficiency and rate can be quantified from $\eta_{FRET} = 1 - \left(\frac{\tau_{DA}}{\tau_D}\right)$ and $\Gamma_{FRET} = \frac{1}{\tau_{FRET}} = \frac{1}{\tau_{DA}} - \frac{1}{\tau_D}$, correspondingly. As a result, owing to layer-to-layer dipole–dipole coupling in our hybrid, we obtained FRET efficiency of 97.84% along with a fast FRET rate of 21.26 ns^{-1}, indicting an ultra-efficient transferring of exciton from CQWs to monolayer of MoS_2.

7.4. Electrical Characterization of the Hybrid System Under Dark Conditions

The electrical measurements of our fabricated devices are performed in ambient condition at room temperature under the dark and illuminated conditions. It is worth to mentioning

that Si substrate was used as back gate contact for modulation of I_{DS} current. The dark current characteristics of the devices are not only important for photocurrent extraction but also important to reveal any electronic or physical modification on the device before and after utilizing the CQWs layer. In that manner the transport measurements of the pristine and hybrid devices are presented in Figure 7.5. Figure 7.5a demonstrates the transfer characteristics of bare MoS_2 device on the logarithmic and linear scale with a positive bias of $V_{DS} = 1\,V$. The back-gate voltage sweep range of positively biased devices is larger than the negatively biased (Figure 7.5b) one to be able modulated maximum saturation current. This asymmetric bias characteristic of devices is due to formation of asymmetric Schottky contacts between MoS_2 and Au/Ti metal contacts. The asymmetric Schottky barriers is usually caused by the oxidation of metal contacts due to adsorbates at the metal-semiconductor interface and difference between work functions of channel and contact materials[230]. So as to apply a narrow gate-voltage sweep range, all pristine and hybrid devices biased with a negative bias of $V_{DS} = -2\,V$. The transfer characteristics of MoS_2-only and MoS_2-CQWs devices under dark conditions at $V_{DS} = -2\,V$ are shown in Figure 7.5b in both logarithmic and linear scales.

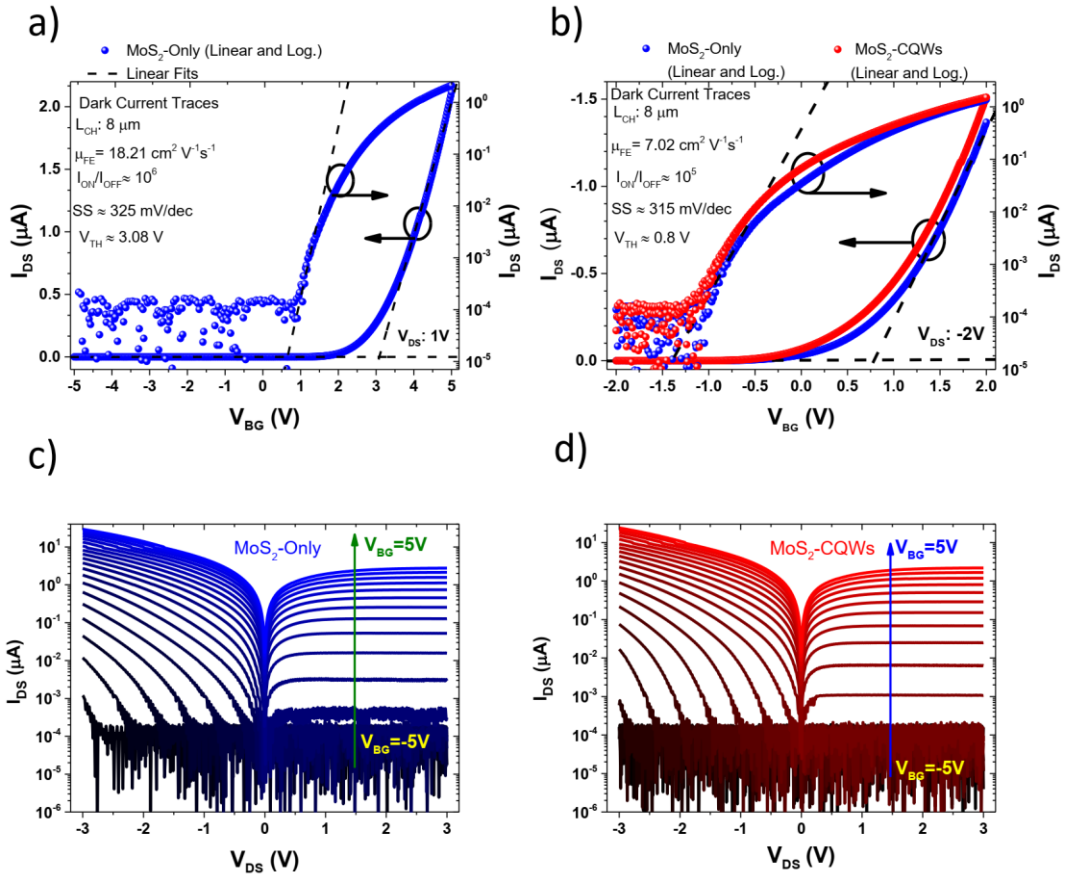

Figure 7.5 *Electronic transport measurement of pristine and hybrid devices under dark conditions. (a) The transfer characteristics ($I_{DS} - V_{BG}$) of MoS_2-Only device for $V_{DS} = 1\ V$ under dark conditions. (b) The transfer characteristics of MoS_2-only and MoS_2-CQWs devices for $V_{DS} = -2\ V$ under dark conditions. The output characteristics ($I_{DS} - V_{DS}$) of (c) MoS_2-CQWs and (d) MoS_2-only devices for V_{BG} sweep from $-5\ V$ to $5\ V$ under dark conditions.*

Here, threshold voltages (V_{TH}) were determined from the linear regime of the on-state conduction with a commonly used method which is known as linear extrapolation (LE)[153], where the tangent line with maximum slope compared to transfer curve at the peak transconductance (g_m) is linearly extrapolated to V_{BG} (axis) and V_{TH} values is extracted by adding $\frac{V_{DS}}{2}$ to the intercept at V_{BG} axis. The estimated threshold voltages for MoS_2-Only and MoS_2-CQWs and are -0.5 V and -0.3 V, respectively. It is worth mentioning that the similar values of V_{TH} for MoS_2-Only and MoS_2-CQWs indicates that there is no charge transfer from CQWs to MoS_2 which is expected to change the V_{TH}[216]. In addition, as can be seen in Figure 7.5b, the dark current for both follows very similar behavior which is another proof for not existing charge transfer or doping effect in our

system. The field-effective carrier mobility (μ_{FE}), subthreshold swing value (SS) and the current ON/OFF ratio of the fabricated devices were calculated to reveal the electronic transport performances. The field-effect mobilities are estimated from the calculated transconductance $g_m = \frac{\partial I_{DS}}{\partial V_{BG}}$ via using the following expression:

$$\mu_{FE} = \frac{L_{CH}}{W_{CH}} \frac{1}{V_{DS} C_g} \frac{\partial I_{DS}}{\partial V_{BG}} \quad (\mathrm{cm^2V^{-1}s^{-1}}) \qquad (1)$$

Where I_{DS} is drain-source current, $\frac{L_{CH}}{W_{CH}}$ is the ratio of length to width of the channel, V_{DS} is bias voltage and C_g is the gate capacitance per unit area. C_g can be defined as $C_g = \frac{\varepsilon_g}{t_g}$ ·where ε_g and t_g is the dielectric constant and the thickness of the gate oxide, respectively[231]. The calculated μ_{FE} values are 7.02 and 18. 21 $\mathrm{cm^2V^{-1}s^{-1}}$ for negatively and positively biased devices, correspondingly which are high carrier mobilities for our device structure and measurement conditions. The fabricated devices are achieved a high current ON/OFF ratio of $\sim 10^5$ and very low SS values of 315 mV/dec and 325 mV/dec under positive and negative bias, respectively. The characteristic curves (I_{DS}-V_{DS}) of MoS_2-Only and MoS_2-CQWs and devices are exhibited in Figure 7.5c and 7.5d, respectively for gate modulation voltage which sweeps from V_{BG}=-5 V to 5 V with an interval of 0.5 V. To further examine the effect of the sensitization layer (i.e., CQWs layer) on the output characteristics of the devices under dark condition, we swept V_{DS} voltages from -3 V to 3 V to. Later, the maximum saturation currents (I_{DSS}) were measured before and after of the CQWs layer deposition, as a result, the measured values are very close to each other, indicating that the CQWs layer did not cause any modification without illumination.

7.5. Opto-Electrical Characterization of the Hybrid System

To evaluate the enhancement of optoelectronic performance of the sensitized MoS_2 phototransistor compared to the pristine MoS_2 one, we investigated the photocurrent-bias voltage (I_{PH}-V_{DS}) (Figure 7.6a) and the photocurrent-gate voltage ($I_{PH} - V_{BG}$) characteristics (Figure 7.6b). The photocurrent (I_{PH}) was quantified from the difference between the measured currents under illumination and dark conditions ($I_{PH} = I_{LIGTH} - I_{DARK}$) for different values of V_{DS} and V_{BG}. Figure 7.6a represents $I_{PH} - V_{DS}$ curves of

both pristine and sensitized MoS_2 phototransistor which were measured under the illumination condition of $375\ nm$ and $1\ mW$ for tuned back-gate voltages from $2\ V$ to $5\ V$ with an interval of 0.5 V. As expected, the photocurrents of both MoS_2-only and MoS_2-CQWs devices were increased with rising the illumination power. Although, owing to an efficient FRET process, the photocurrent of MoS_2-CQWs device was dramatically enhanced with respect to MoS_2-Only one for all gate voltages at $I_{PH} - V_{DS}$ and $I_{PH} - V_{BG}$ (Figure 7.6a and 7.6b). The maximum photocurrent enhancement in sensitized phototransistor was found to be 3-fold lager compared to the pristine MoS_2 device. Furthermore, by rising the illumination power, I_{PH}-V_{BG} curves of both devices shifted in negative gate voltages which also indicates the threshold voltage shift (Figure 7.6b). The threshold voltages of the illuminated transfer curves extracted by LE method, and the shift of the threshold voltages, which is the difference between threshold voltages of the illuminated ($V_{TH(ILL)}$) and dark measurements ($V_{TH(DRK)}$) ($\Delta V_{TH} = V_{TH(ILL)}$-$V_{TH(DRK)}$) for both devices, are plotted in Figure 7.6c as a function of incident power. The shift in the threshold voltages (ΔV_{TH}) is increased with raising the incident illumination power, this can be considered as a signature of photogating which is also known as photovoltaic effect. The MoS_2-CQWs offers a smaller threshold voltage shift range compare to MoS_2-only device where ΔV_{TH} varies from ~ 630 to $\sim 860\ mV$ for CQWs-MoS_2 and from ~ 150 to $\sim 770\ mV$ for MoS_2-only. However, at low level of illumination power (at $1\ \mu W$), ΔV_{TH} exhibits higher absolute shift value of $\sim 630\ mV$ compared to the absolute shift value ($\sim 150\ mV$) of MoS_2-Only device. This higher absolute shift value could be attributed to the effect of the ET from CQWs to MoS_2 layer due to increased exciton population by transferred energy from CQWs to MoS_2 layer. Moreover, $\Delta V_{TH} - P_{IL}$ curves of both devices fitted well with the function of $\Delta V_{TH} = \alpha P_{IL}^{b}$ [232] where α and b are constants. Here, the obtained b values for sensitized- and pristine-MoS_2 device is ≈ 0.07 and ≈ 0.15, respectively, which are smaller than 1, confirming the occurrence of photogating effect. To further understand the mechanism that underlay the photocurrent enhancement and effect of FRET process on MoS_2, the log-plotted photocurrent (I_{PH}) curves of MoS_2-CQWs and MoS_2-Only devices with respect to the illumination power were fitted by a linear function of $I_{PH} \propto P_{IL}^{\alpha}$, where the obtained α factor gives information about the rate of photogating and photoconductivity effects (Figure 7.7a and 7.7b). The photogating effect results in a linearly increase of photocurrent as a function

of illumination power ($I_{PH} \propto P_{IL}$), while photoconductivity shows a sublinear dependency to the incident power ($I_{PH} \propto P_{IL}^{\alpha}$ where $\alpha < 1$)[232-234].

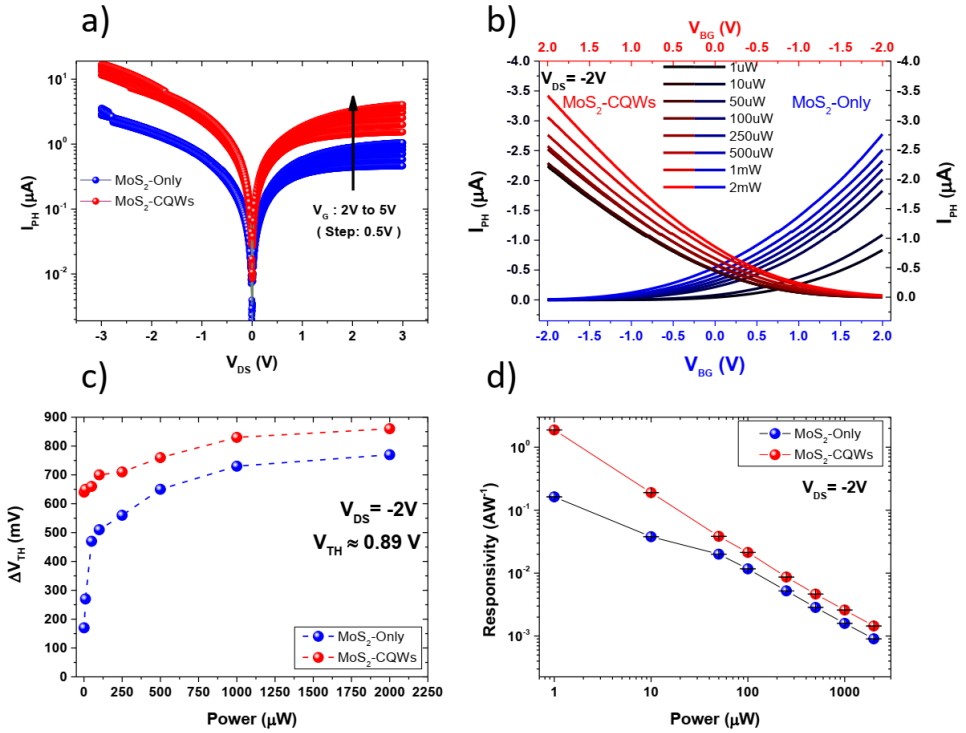

Figure 7.6 *Optoelectronic performance of the CQWs-MoS_2 phototransistor compared with bare MoS_2 phototransistor. (a) The I_{PH}-V_{DS} curves under illumination (P_{IL}) for a range of back-gate voltage (from 2 V to 5 V) and (b) the transfer characteristics of photocurrent (I_{PH}-V_{BG}) as a function of illumination power (from 1 μW to 2 mW) of MoS_2-CQWs (red) and MoS_2-Only (blue) devices. (c) The threshold voltage shift and (d) the photoresponsivity of both devices under the bias voltage of −2 V as function of increasing illumination power.*

The fitting parameter of α is plotted as function of gate voltage for both devices in Figure 7.7c. The α is declined from 1 (at V_{BG}=-2V) to 0.14 (at V_{BG}=2V) for MoS_2-Only device, indicating that the foremost effect was purely photoconductivity at V_{BG}=-2V but it was turned to photogating effect as the back-gate voltage increases from -2V to 2V. On the other hand, the α exponent was decreased from 0.70 (at V_{BG}=-2V) to 0.06 (at V_{BG}=2V) for MoS_2-CQWs device that shows the both mechanisms were coexist at V_{BG}=-2V, then, at the elevated back-gate voltages, the photogating is the dominant mechanism. The photogating effect in the layered materials occurs due to the consequence of long-lived traps at the surface or interface which are mainly induced during the growth process as S-vacancies[229]. The decrease in the α exponent for MoS_2-CQWs- device compared to the pristine MoS_2 device in all gate voltages indicate that the ET from CQWs to MoS_2

layer was also coupled by the traps states of MoS_2 and results in an increase of the effect of photogating.

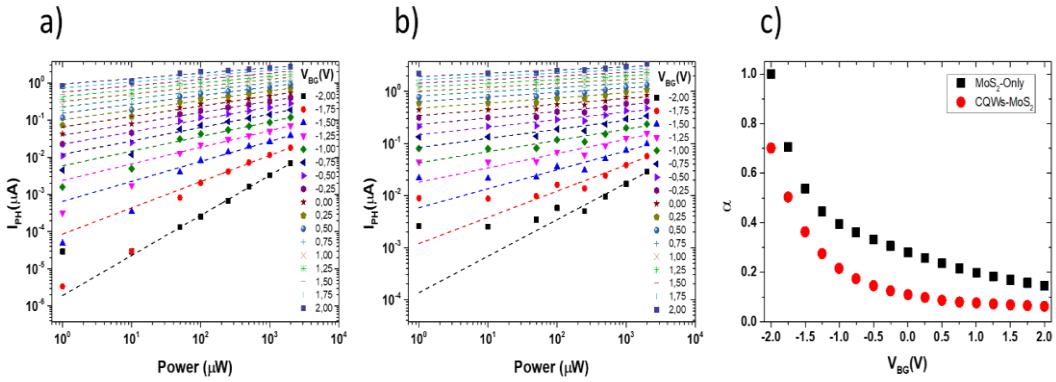

Figure 7.7 *The photocurrent extracted from transport measurements versus incident laser power of MoS_2-Only (a) and MoS_2-CQWs (b) devices. The exponent (α) extracted from linearly fitted photocurrent vs power curves; black squares for MoS_2-Only and red circles for MoS_2-CQWs devices (c).*

Furthermore, we estimated the photo-responsivities of both devices from $R = \frac{I_{PH}}{P_{eff}}$ where $P_{eff} = P_{in} \times \frac{A_{device}}{A_{beamspot}}$, A is the area and I_{PH} is the photocurrent. The estimated R values are plotted as function of the illumination power at $V_{BG} = 2V$ in Figure 7.6d. In particular, at $1\ \mu W$ of illumination power, R for MoS_2-Only device was found to be $\sim 0.16\ AW^{-1}$, while for MoS_2-CQWs device was obtained as $\sim 1.88\ AW^{-1}$, which indicates ~ 11 fold enhancement with ultra-efficient FRET from CQWs to MoS_2 layer enabled us to achieve higher level of the photo-responsivity factor at operating illumination powers.

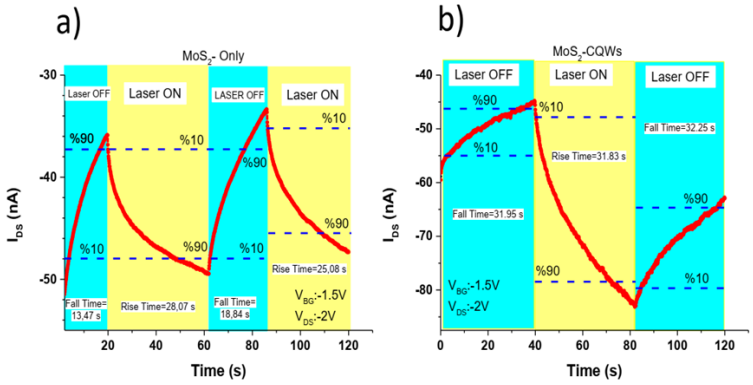

Figure 7.8 *The transient response of the MoS_2-Only and MoS_2-CQWs devices at an incident laser power of $1\ mW$ with constant bias and gate voltage.*

In addition, the temporal response of the MoS_2-Only and MoS_2-CQWs devices are shown in Figure 7.8a and 7.8b, respectively. The decay and rise times of both devices are in the

orders of seconds due to the trap states at the oxide material interface or surface adsorbates which are fully consistent with those reported values in literature[140, 144].

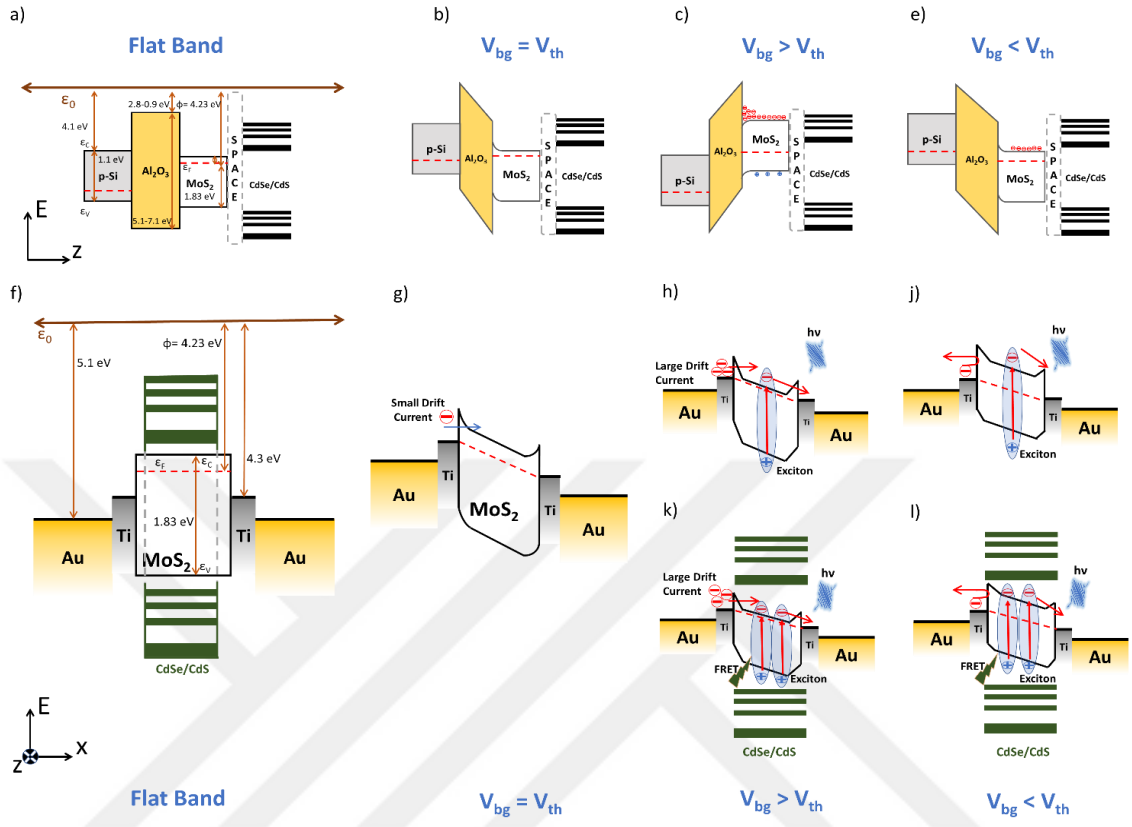

Figure 7.9 *The schematic of channel current transport mechanism with and without assistance of FRET process and energy band diagram of MoS_2-CQWs and MoS_2-Only phototransistors flat band diagrams (a) and (f). Under $V_{BG} = V_{TH}$ (b) and (g), $V_{BG} > V_{TH}$ (ON-state) (c), without CQWs (h) and with CQWs (k) and $V_{BG} < V_{TH}$ (OFF-state) (d) without CQWs (j) and with CQWs (l). The schematics in (a) to (d) are in E-z plane without illumination and the schematics in (f) to (l) are in E-x plane with illumination but the band states of CQWs drawn in (f) to (I) are on E-z-plane that shown E-x plane just for demonstration purposes. E stands for energy-axis.*

Moreover, the effect of illumination, back-gate voltage modulation and FRET process on channel current transport and energy band alignment are explained in details through the schematics in Figure 7.9. The work functions (∅) of MoS_2, Si and Al_2O_3 are 4.23 eV[206, 235], 4.1 eV[235] and 2.8 - 0.9 eV[236], respectively. Because of the distance between, CQWs and MoS_2 which is due to a nonaromatic ligand of oleic acid of CQWs, the charge transfer is ineffective between sensitizer layer and MoS_2. The channel current transfer is mainly modulated by back gate voltage. For the $V_{BG} > V_{TH}$ there is a large drift current (Figure 7.9c, 7.9h and 7.9k). On the other hand, there is small or no drift current for $V_{BG} < V_{TH}$ (Figure 7.9e, 7.9j and 7.9l).

Then, the addition of CQWs layer on top MoS_2 enhanced the photo-induced current by highly efficient transferring of the excitation energy through an electromagnetic

dipole–dipole coupling process (Figure 7.9k and 7.9l). Owing to FRET, the recombination lifetime of electron–hole pairs in MoS_2 is elongated, resulting in higher photocurrent. The ET process also increases the effectiveness of photo-gating process over photoconductivity process as discussed above.

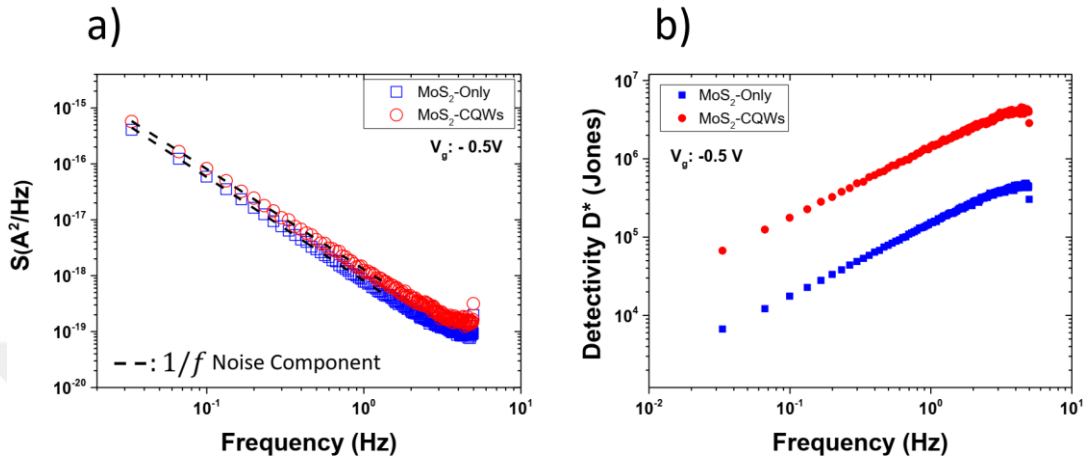

Figure 7.10 *(a) The noise power density and (b) the specific detectivity (D^*) of MoS_2-CQWs and MoS_2-Only phototransistors at $V_{BG} = -0.5\ V$ and $V_{DS} = -2V$.*

Additionally, we analyzed another important figure of merit for our photodetector, which is the specific detectivity (D^*). D^* can be defined as $D^* = (AB)^{1/2}/NEP = RA^{1/2}/S_n$, where A is the active detector area, B is the noise bandwidth, NEP is the noise equivalent power, R is the responsivity and S_n is the noise spectral density. To obtain the noise spectral density, dark current traces were measured at constant gate (V_{BG}) and bias (V_{DS}) voltages (same conditions used for optical characterization) with sample rate of 10 Hz. Then, the noise power density curves calculated from fast Fourier transform of the dark current traces, which are shown in Figure 7.10a, where the noise power density of the sensitized and pristine MoS_2 devices are almost similar. Consequently, the noise power density curves of both devices were fitted via a linear function, where both devices exhibit a similar noise behavior of $1/f$. This behavior is in a good agreement with previously reported MoS_2 based phototransistors, which rises due to the fluctuations in mobility of the carriers[237]. The calculated D^* for CQWs-MoS_2 and MoS_2-Only devices are shown Figure 7.10b as a function of frequency. As can be seen in Figure 7.10b, thanks to ultra-efficient (~%98) FRET from layer of CQWs to MoS_2 in MoS_2-CQWs device (red-colored data points), the estimated D^* is enhanced 10-fold compared to the pristine MoS_2 device (blue-colored data points).

7.6. Conclusion

In conclusion, we have presented a novel hybrid MoS_2-CQWs phototransistor where CQWs acts a layer of sensitization in our system. Owing to ultra-fast (~21 ns^{-1}) and -efficient FRET (~ 98%) from sensitization layer (i.e., CQWs) to active layer (i.e., MoS_2) in our proposed structure, we have achieved 11-fold enhancement in photoresponsivity performance compared to pristine MoS_2 phototransistors. In addition, a 10-fold enhancement was obtained in specific detectivity of sensitized device. Moreover, from transport characteristics, we showed that due to the existence of FRET in our hybrid system, the contribution of photogating mechanism is enhanced compared to photoconductivity effect. This novel hybrid structure described herein offers a new pathway for 2D materials-based detectors with high performances, endorsing their applications in optical communication, video imaging and spectroscopy.

8. CONCLUSIONS and FUTURE OUTLOOK

In this closing chapter, the outputs of this dissertation and their conclusions are briefly summarized. The prospects of future research and possible directions are then addressed

8.1. Conclusion

In the first part of the dissertation, the formation of MoS_2/Graphene heterostructure by using transfer and direct growth methods are demonstrated. The results of Raman and PL analysis of these heterostructures are presented and compared by the Raman and PL characteristics of CVD-grown bare monolayer MoS_2 onto SiO_2/Si. The effect of transfer procedure and graphene itself on the PL and Raman characteristics of MoS_2 has also been studied in detail. It is found that the PL intensity of the MoS_2 has been quenched as one order of magnitude because of charge transfer between MoS_2 and graphene. A blue shift has been measured on peak center of A-exciton which may be the result of stress relaxation.

In Chapter 5, The effect of CVD growth configuration on the long-term stability of the grown structures is investigated. It is found that there is a clear difference in aging process between the MoS_2 flakes grown under different growth configurations, which brings in relatively different growth rates and hence presumably different defect (S) densities and residual stresses. Aging behaviour of the flakes grown with a slower rate are found as aging resistant compared to the flakes grown with a higher growth rate. In order to gain further understanding of the role of strain and S vacancy on aging, DFT calculations are performed together with controlled aging experiments. The results indicate that the S vacancy defects are more effective on the formation of oxidation than the stress effect. Therefore, these results inevitably suggest that S vacancies need to be reduced suggestively by controlling the growth rate, which will improve the long-term stability of MoS_2 monolayers. According to the controlled aging experiments, DFT calculations and spectroscopic measurements, a novel CVD growth configuration that yields oxidation and moisture resistant MoS_2 flakes durable for more than 18 months at ambient conditions is proposed. The effectiveness of proposed method has been also tested and proved by the thermal aging tests.

After being able to growth aging resistant TMDs with proposed novel CVD configuration, the device performance of CVD-grown MoS_2 and WS_2 are compared in Chapter 6. The transport and physical properties of devices based on monolayer MoS_2

and WS_2, which are grown in the of same CVD system and fabricated with optical lithography are presented. The characterization of the both devices are done under the same ambient conditions to understand their comparative performance. The back-gated, CVD-grown MoS_2 based devices in ambient conditions without any encapsulation and doping process show higher effective carrier mobility, lower threshold voltage and higher photoresponsivity which are very important for high performance transistors and optoelectronic applications. On the other hand, WS_2 based devices which have the same configuration and measurement system as the MoS_2 based ones, exhibit high current ON/OFF ratio and low hysteresis behavior suggestively due to the lower density of the trap states between the dielectric material and WS_2 where this low hysteresis behavior is critical for electronic applications. The results suggest that MoS_2 based FET devices are more promising compared to WS_2 based ones under ambient conditions without any encapsulation, because 2D WS_2 structures are more sensitive to the ambient conditions with respect to 2D MoS_2 structures.

In Chapter 7, a novel photodetection performance enhancement methodology is applied to MoS_2-based phototransistors. The MoS2-based phototransistors are sensitized by a thin film of colloidal quantum wells. The novel hybrid MoS_2-CQWs phototransistor where CQWs acts a layer of sensitization in the structure is presented. Owing to ultra-fast (~21 ns^{-1}) and -efficient FRET (~ 98%) from sensitization layer (i.e., CQWs) to active layer (i.e., MoS_2) in the proposed structure, 11-fold enhancement in photoresponsivity performance compared to pristine MoS_2 phototransistors have achieved. In addition, a 10-fold enhancement is obtained in specific detectivity of sensitized device. Moreover, from transport characteristics, it is shown that due to the existence of FRET in the hybrid system, the contribution of photogating mechanism is enhanced compared to photoconductivity effect. This novel hybrid structure described herein offers a new pathway for 2D materials-based detectors with high performances, endorsing their applications in optical communication, video imaging and spectroscopy.

8.2. Future Outlook

The direct growth of heterostructures of 2D materials except from MoS_2/Graphene could be beneficial to decrease the transfer related defects and damages. Since the positive effect of glass substrates on CVD growth of TMDs could be used to advance on direct growth of 2D heterostructures. The investigation of 2D heterostructures has crucial

importance on future electronics. The latest FET architecture which is called FinFET, is a suitable and promising structure for heterostructure made from monolayer materials including several numbers of layers.

It is shown that the growth induced defects and stress determines the long-term stability of the grown 2D monolayer materials. However, the long-term stability investigation of 2D materials grown on glass substrates has not been investigated in that manner due to limited time for the PhD period. Since TMDs growth onto glass is a promising method, it is important to research on the stability of monolayer grown on glass.

The sensitive of WS_2 to environmental conditions and atmosphere could be beneficial to fabricate WS_2 based gas sensors with possible high detectivity and sensitivity. In this sense it is important to design and fabricate unique device architectures to take full advantage of sensitivity of WS_2.

The effect of quantum wells on the performance enhancement is demonstrated in the related Chapter. However, the effect of other quantum structures such quantum dots, or thicker quantum wells has not been investigated yet. To fabricate different TMDs or direct bandgap 2D material-based phototransistor with different sensitizer layer is promising for high performance optoelectronic devices.

9. REFERENCES

[1] Lojek, B., (2007). The MOS Transistor. *History of Semiconductor Engineering*, 317-374.

[2] Moore, G.E. *No exponential is forever: but" Forever" can be delayed![semiconductor industry]*. in *2003 IEEE International Solid-State Circuits Conference, 2003. Digest of Technical Papers. ISSCC.* 2003. IEEE.

[3] Schwierz, F., Pezoldt, J., and Granzner, R., (2015). Two-dimensional materials and their prospects in transistor electronics. *Nanoscale*, 7(18), 8261-8283.

[4] Thompson, S.E., Sun, G., Choi, Y.S., and Nishida, T., (2006). Uniaxial-process-induced strained-Si: Extending the CMOS roadmap. *IEEE Transactions on Electron Devices*, 53(5), 1010-1020.

[5] Del Alamo, J.A., (2011). Nanometre-scale electronics with III–V compound semiconductors. *Nature*, 479(7373), 317.

[6] Shang, H., Frank, M.M., Gusev, E.P., Chu, J.O., Bedell, S.W., Guarini, K.W., and Ieong, M., (2006). Germanium channel MOSFETs: Opportunities and challenges. *IBM Journal of Research and Development*, 50(4.5), 377-386.

[7] Novoselov, K.S., Geim, A.K., Morozov, S.V., Jiang, D., Zhang, Y., Dubonos, S.V., Grigorieva, I.V., and Firsov, A.A., (2004). Electric field effect in atomically thin carbon films. *science*, 306(5696), 666-669.

[8] Akbar, F., Kolahdouz, M., Larimian, S., Radfar, B., and Radamson, H., (2015). Graphene synthesis, characterization and its applications in nanophotonics, nanoelectronics, and nanosensing. *Journal of Materials Science: Materials in Electronics*, 26(7), 4347-4379.

[9] Novoselov, K.S., Fal'ko, V.I., Colombo, L., Gellert, P.R., Schwab, M.G., and Kim, K., (2012). A roadmap for graphene. *Nature*, 490(7419), 192-200.

[10] Radisavljevic, B., Radenovic, A., Brivio, J., Giacometti, V., and Kis, A., (2011). Single-layer MoS2 transistors. *Nat Nanotechnol*, 6(3), 147-50.

[11] Liu, C.-C., Feng, W., and Yao, Y., (2011). Quantum spin Hall effect in silicene and two-dimensional germanium. *Physical review letters*, 107(7), 076802.

[12] Zhang, Y., Tan, Y.-W., Stormer, H.L., and Kim, P., (2005). Experimental observation of the quantum Hall effect and Berry's phase in graphene. *nature*, 438(7065), 201.

[13] Zhang, Y., Li, H., Wang, H., Liu, R., Zhang, S.-L., and Qiu, Z.-J., (2015). On valence-band splitting in layered MoS2. *ACS nano*, 9(8), 8514-8519.

[14] Mak, K.F., He, K., Shan, J., and Heinz, T.F., (2012). Control of valley polarization in monolayer MoS 2 by optical helicity. *Nature nanotechnology*, 7(8), 494.

[15] Mak, K.F., Lee, C., Hone, J., Shan, J., and Heinz, T.F., (2010). Atomically thin MoS(2): a new direct-gap semiconductor. *Phys Rev Lett*, 105(13), 136805.

[16] Hoefflinger, B., *ITRS: The international technology roadmap for semiconductors*, in *Chips 2020*. 2011, Springer. p. 161-174.

[17] *Web of Science Citation Report*. 2019; Available from: http://www.webofknowledge.com/.

[18] Geim, A.K. and Grigorieva, I.V., (2013). Van der Waals heterostructures. *Nature*, 499(7459), 419.

[19] Miró, P., Audiffred, M., and Heine, T., (2014). An atlas of two-dimensional materials. *Chemical Society Reviews*, 43(18), 6537-6554.
[20] Mounet, N., Gibertini, M., Schwaller, P., Campi, D., Merkys, A., Marrazzo, A., Sohier, T., Castelli, I.E., Cepellotti, A., and Pizzi, G., (2018). Two-dimensional materials from high-throughput computational exfoliation of experimentally known compounds. *Nature nanotechnology*, 13(3), 246.
[21] Novoselov, K.S., Jiang, D., Schedin, F., Booth, T., Khotkevich, V., Morozov, S., and Geim, A.K., (2005). Two-dimensional atomic crystals. *Proceedings of the National Academy of Sciences*, 102(30), 10451-10453.
[22] Eda, G., Yamaguchi, H., Voiry, D., Fujita, T., Chen, M., and Chhowalla, M., (2011). Photoluminescence from chemically exfoliated MoS2. *Nano letters*, 11(12), 5111-5116.
[23] Thripuranthaka, M. and Late, D.J., (2014). Temperature dependent phonon shifts in single-layer WS2. *ACS Appl. Mater. Interfaces*, 6, 1158-1163.
[24] Cheng, J., Wang, C., Zou, X., and Liao, L., (2019). Recent advances in optoelectronic devices based on 2d materials and their heterostructures. *Advanced Optical Materials*, 7(1), 1800441.
[25] Plechinger, G., Mann, J., Preciado, E., Barroso, D., Nguyen, A., Eroms, J., Schueller, C., Bartels, L., and Korn, T., (2014). A direct comparison of CVD-grown and exfoliated MoS2 using optical spectroscopy. *Semiconductor Science and Technology*, 29(6), 064008.
[26] Zhi, C., Bando, Y., Tang, C., Kuwahara, H., and Golberg, D., (2009). Large-scale fabrication of boron nitride nanosheets and their utilization in polymeric composites with improved thermal and mechanical properties. *Advanced Materials*, 21(28), 2889-2893.
[27] Joensen, P., Frindt, R., and Morrison, S.R., (1986). Single-layer MoS2. *Materials research bulletin*, 21(4), 457-461.
[28] Zeng, Z., Yin, Z., Huang, X., Li, H., He, Q., Lu, G., Boey, F., and Zhang, H., (2011). Single-Layer Semiconducting Nanosheets: High-yield preparation and device fabrication. *Angewandte Chemie International Edition*, 50(47), 11093-11097.
[29] Liu, N., Fu, L., Dai, B., Yan, K., Liu, X., Zhao, R., Zhang, Y., and Liu, Z., (2010). Universal segregation growth approach to wafer-size graphene from non-noble metals. *Nano letters*, 11(1), 297-303.
[30] Yu, Q., Lian, J., Siriponglert, S., Li, H., Chen, Y.P., and Pei, S.-S., (2008). Graphene segregated on Ni surfaces and transferred to insulators. *Applied Physics Letters*, 93(11), 113103.
[31] Kwon, S.-Y., Ciobanu, C.V., Petrova, V., Shenoy, V.B., Bareno, J., Gambin, V., Petrov, I., and Kodambaka, S., (2009). Growth of semiconducting graphene on palladium. *Nano letters*, 9(12), 3985-3990.
[32] Bae, S., Kim, H., Lee, Y., Xu, X., Park, J.-S., Zheng, Y., Balakrishnan, J., Lei, T., Kim, H.R., and Song, Y.I., (2010). Roll-to-roll production of 30-inch graphene films for transparent electrodes. *Nature nanotechnology*, 5(8), 574.
[33] Li, X., Magnuson, C.W., Venugopal, A., Tromp, R.M., Hannon, J.B., Vogel, E.M., Colombo, L., and Ruoff, R.S., (2011). Large-area graphene single crystals grown by low-pressure chemical vapor deposition of methane on copper. *Journal of the American Chemical Society*, 133(9), 2816-2819.
[34] Somani, P.R., Somani, S.P., and Umeno, M., (2006). Planer nano-graphenes from camphor by CVD. *Chemical Physics Letters*, 430(1-3), 56-59.

[35] Tetlow, H., De Boer, J.P., Ford, I., Vvedensky, D., Coraux, J., and Kantorovich, L., (2014). Growth of epitaxial graphene: Theory and experiment. *Physics reports*, 542(3), 195-295.
[36] Ma, L., Ren, W., Dong, Z., Liu, L., and Cheng, H., (2012). Progress of graphene growth on copper by chemical vapor deposition: Growth behavior and controlled synthesis. *Chinese science bulletin*, 57(23), 2995-2999.
[37] Geng, D., Wang, H., and Yu, G., (2015). Graphene single crystals: size and morphology engineering. *Advanced Materials*, 27(18), 2821-2837.
[38] Ma, T., Ren, W., Liu, Z., Huang, L., Ma, L.-P., Ma, X., Zhang, Z., Peng, L.-M., and Cheng, H.-M., (2014). Repeated growth–etching–regrowth for large-area defect-free single-crystal graphene by chemical vapor deposition. *Acs Nano*, 8(12), 12806-12813.
[39] Addou, R., Dahal, A., Sutter, P., and Batzill, M., (2012). Monolayer graphene growth on Ni (111) by low temperature chemical vapor deposition. *Applied Physics Letters*, 100(2), 021601.
[40] Hass, J., De Heer, W., and Conrad, E., (2008). The growth and morphology of epitaxial multilayer graphene. *Journal of Physics: Condensed Matter*, 20(32), 323202.
[41] Sun, Z., Yan, Z., Yao, J., Beitler, E., Zhu, Y., and Tour, J.M., (2010). Growth of graphene from solid carbon sources. *Nature*, 468(7323), 549.
[42] Deng, B., Liu, Z., and Peng, H., (2019). Toward mass production of CVD graphene films. *Advanced Materials*, 31(9), 1800996.
[43] Hesjedal, T., (2011). Continuous roll-to-roll growth of graphene films by chemical vapor deposition. *Applied Physics Letters*, 98(13), 133106.
[44] Deng, B., Hsu, P.-C., Chen, G., Chandrashekar, B., Liao, L., Ayitimuda, Z., Wu, J., Guo, Y., Lin, L., and Zhou, Y., (2015). Roll-to-roll encapsulation of metal nanowires between graphene and plastic substrate for high-performance flexible transparent electrodes. *Nano letters*, 15(6), 4206-4213.
[45] Liu, K.-K., Zhang, W., Lee, Y.-H., Lin, Y.-C., Chang, M.-T., Su, C.-Y., Chang, C.-S., Li, H., Shi, Y., and Zhang, H., (2012). Growth of large-area and highly crystalline MoS2 thin layers on insulating substrates. *Nano letters*, 12(3), 1538-1544.
[46] Feng, Y., Zhang, K., Wang, F., Liu, Z., Fang, M., Cao, R., Miao, Y., Yang, Z., Mi, W., and Han, Y., (2015). Synthesis of large-area highly crystalline monolayer molybdenum disulfide with tunable grain size in a H2 atmosphere. *ACS applied materials & interfaces*, 7(40), 22587-22593.
[47] George, A.S., Mutlu, Z., Ionescu, R., Wu, R.J., Jeong, J.S., Bay, H.H., Chai, Y., Mkhoyan, K.A., Ozkan, M., and Ozkan, C.S., (2014). Wafer scale synthesis and high resolution structural characterization of atomically thin MoS2 layers. *Advanced Functional Materials*, 24(47), 7461-7466.
[48] Zhan, Y., Liu, Z., Najmaei, S., Ajayan, P.M., and Lou, J., (2012). Large-area vapor-phase growth and characterization of MoS2 atomic layers on a SiO2 substrate. *Small*, 8(7), 966-971.
[49] Lin, Y.-C., Zhang, W., Huang, J.-K., Liu, K.-K., Lee, Y.-H., Liang, C.-T., Chu, C.-W., and Li, L.-J., (2012). Wafer-scale MoS 2 thin layers prepared by MoO 3 sulfurization. *Nanoscale*, 4(20), 6637-6641.
[50] Pyeon, J.J., Kim, S.H., Jeong, D.S., Baek, S.-H., Kang, C.-Y., Kim, J.-S., and Kim, S.K., (2016). Wafer-scale growth of MoS 2 thin films by atomic layer deposition. *Nanoscale*, 8(20), 10792-10798.

[51] Wang, X., Feng, H., Wu, Y., and Jiao, L., (2013). Controlled synthesis of highly crystalline MoS2 flakes by chemical vapor deposition. *Journal of the American Chemical Society*, 135(14), 5304-5307.

[52] Kumar, P., Singh, M., Gopal, P., and Reddy, G. *Sulfurization of WO3 nanorods into WS2 as a function of H2S/Ar partial pressure*. in *AIP Conference Proceedings*. 2018. AIP Publishing.

[53] Liu, H., Wong, S.L., and Chi, D., (2015). CVD growth of MoS2-based two-dimensional materials. *Chemical Vapor Deposition*, 21(10-11-12), 241-259.

[54] Huang, X., Zeng, Z., and Zhang, H., (2013). Metal dichalcogenide nanosheets: preparation, properties and applications. *Chemical Society Reviews*, 42(5), 1934-1946.

[55] Liu, H.F., Wong, S.L., and Chi, D.Z., (2015). CVD Growth of MoS2-based Two-dimensional Materials. *Chemical Vapor Deposition*, 21(10-11-12), 241-259.

[56] Butler, S.Z., Hollen, S.M., Cao, L., Cui, Y., Gupta, J.A., Gutiérrez, H.R., Heinz, T.F., Hong, S.S., Huang, J., and Ismach, A.F., (2013). Progress, challenges, and opportunities in two-dimensional materials beyond graphene. *ACS nano*, 7(4), 2898-2926.

[57] Chen, Y., Sun, J., Gao, J., Du, F., Han, Q., Nie, Y., Chen, Z., Bachmatiuk, A., Priydarshi, M.K., Ma, D., Song, X., Wu, X., Xiong, C., Rümmeli, M.H., Ding, F., Zhang, Y., and Liu, Z., (2015). Growing Uniform Graphene Disks and Films on Molten Glass for Heating Devices and Cell Culture. *Advanced Materials*, 27(47), 7839-7846.

[58] Chen, J., Zhao, X., Tan, S.J.R., Xu, H., Wu, B., Liu, B., Fu, D., Fu, W., Geng, D., Liu, Y., Liu, W., Tang, W., Li, L., Zhou, W., Sum, T.C., and Loh, K.P., (2017). Chemical Vapor Deposition of Large-Size Monolayer MoSe2 Crystals on Molten Glass. *Journal of the American Chemical Society*, 139(3), 1073-1076.

[59] Yang, P., Zou, X., Zhang, Z., Hong, M., Shi, J., Chen, S., Shu, J., Zhao, L., Jiang, S., Zhou, X., Huan, Y., Xie, C., Gao, P., Chen, Q., Zhang, Q., Liu, Z., and Zhang, Y., (2018). Batch production of 6-inch uniform monolayer molybdenum disulfide catalyzed by sodium in glass. *Nature Communications*, 9(1), 979.

[60] Yuping, S., Pengfei, Y., Shaolong, J., Zhepeng, Z., Yahuan, H., Chunyu, X., Min, H., Jianping, S., and Yanfeng, Z., (2019). Na-assisted fast growth of large single-crystal MoS 2 on sapphire. *Nanotechnology*, 30(3), 034002.

[61] Chen, J., Zhao, X., Tan, S.J., Xu, H., Wu, B., Liu, B., Fu, D., Fu, W., Geng, D., Liu, Y., Liu, W., Tang, W., Li, L., Zhou, W., Sum, T.C., and Loh, K.P., (2017). Chemical Vapor Deposition of Large-Size Monolayer MoSe2 Crystals on Molten Glass. *J Am Chem Soc*, 139(3), 1073-1076.

[62] Liu, L., Kumar, S.B., Ouyang, Y., and Guo, J., (2011). Performance limits of monolayer transition metal dichalcogenide transistors. *IEEE Transactions on Electron Devices*, 58(9), 3042-3047.

[63] Yoon, Y., Ganapathi, K., and Salahuddin, S., (2011). How good can monolayer MoS2 transistors be? *Nano letters*, 11(9), 3768-3773.

[64] Mayorov, A.S., Gorbachev, R.V., Morozov, S.V., Britnell, L., Jalil, R., Ponomarenko, L.A., Blake, P., Novoselov, K.S., Watanabe, K., and Taniguchi, T., (2011). Micrometer-scale ballistic transport in encapsulated graphene at room temperature. *Nano letters*, 11(6), 2396-2399.

[65] Lee, C., Wei, X., Kysar, J.W., and Hone, J., (2008). Measurement of the elastic properties and intrinsic strength of monolayer graphene. *science*, 321(5887), 385-388.

[66] Balandin, A.A., (2011). Thermal properties of graphene and nanostructured carbon materials. *Nature materials*, 10(8), 569.
[67] Neto, A.C., Guinea, F., Peres, N.M., Novoselov, K.S., and Geim, A.K., (2009). The electronic properties of graphene. *Reviews of modern physics*, 81(1), 109.
[68] Han, M.Y., Özyilmaz, B., Zhang, Y., and Kim, P., (2007). Energy band-gap engineering of graphene nanoribbons. *Physical review letters*, 98(20), 206805.
[69] Schwierz, F., (2010). Graphene transistors. *Nature nanotechnology*, 5(7), 487.
[70] Nakada, K., Fujita, M., Dresselhaus, G., and Dresselhaus, M.S., (1996). Edge state in graphene ribbons: Nanometer size effect and edge shape dependence. *Physical Review B*, 54(24), 17954.
[71] Obradovic, B., Kotlyar, R., Heinz, F., Matagne, P., Rakshit, T., Giles, M., Stettler, M., and Nikonov, D., (2006). Analysis of graphene nanoribbons as a channel material for field-effect transistors. *Applied Physics Letters*, 88(14), 142102.
[72] Areshkin, D.A., Gunlycke, D., and White, C.T., (2007). Ballistic transport in graphene nanostrips in the presence of disorder: Importance of edge effects. *Nano letters*, 7(1), 204-210.
[73] Novoselov, K.S., Geim, A.K., Morozov, S., Jiang, D., Katsnelson, M.I., Grigorieva, I., Dubonos, S., Firsov, and AA, (2005). Two-dimensional gas of massless Dirac fermions in graphene. *nature*, 438(7065), 197.
[74] Morozov, S., Novoselov, K., Katsnelson, M., Schedin, F., Elias, D., Jaszczak, J.A., and Geim, A., (2008). Giant intrinsic carrier mobilities in graphene and its bilayer. *Physical review letters*, 100(1), 016602.
[75] Manzeli, S., Ovchinnikov, D., Pasquier, D., Yazyev, O.V., and Kis, A., (2017). 2D transition metal dichalcogenides. *Nature Reviews Materials*, 2(8), 17033.
[76] Splendiani, A., Sun, L., Zhang, Y., Li, T., Kim, J., Chim, C.-Y., Galli, G., and Wang, F., (2010). Emerging photoluminescence in monolayer MoS2. *Nano letters*, 10(4), 1271-1275.
[77] Pulkin, A. and Yazyev, O.V., (2016). Spin-and valley-polarized transport across line defects in monolayer MoS 2. *Physical Review B*, 93(4), 041419.
[78] Chhowalla, M., Jena, D., and Zhang, H., (2016). Two-dimensional semiconductors for transistors. *Nature Reviews Materials*, 1, 16052.
[79] Jariwala, D., Sangwan, V.K., Lauhon, L.J., Marks, T.J., and Hersam, M.C., (2014). Emerging device applications for semiconducting two-dimensional transition metal dichalcogenides. *ACS nano*, 8(2), 1102-1120.
[80] Papageorgopoulos, C. and Jaegermann, W., (1995). Li intercalation across and along the van der Waals surfaces of MoS2 (0001). *Surface science*, 338(1-3), 83-93.
[81] Wypych, F. and Schöllhorn, R., (1992). 1T-MoS 2, a new metallic modification of molybdenum disulfide. *Journal of the Chemical Society, Chemical Communications*, (19), 1386-1388.
[82] Chhowalla, M., Shin, H.S., Eda, G., Li, L.-J., Loh, K.P., and Zhang, H., (2013). The chemistry of two-dimensional layered transition metal dichalcogenide nanosheets. *Nature chemistry*, 5(4), 263.
[83] Santosh, K., Longo, R.C., Addou, R., Wallace, R.M., and Cho, K., (2014). Impact of intrinsic atomic defects on the electronic structure of MoS2 monolayers. *Nanotechnology*, 25(37), 375703.
[84] Lin, Z., Carvalho, B.R., Kahn, E., Lv, R., Rao, R., Terrones, H., Pimenta, M.A., and Terrones, M., (2016). Defect engineering of two-dimensional transition metal dichalcogenides. *2D Materials*, 3(2), 022002.

[85] Savan, A., Pflüger, E., Voumard, P., Schröer, A., and Simmonds, M., (2000). Modern solid lubrication: recent developments and applications of MoS2. *Lubrication Science*, 12(2), 185-203.

[86] Santhosh, S. and Madhavan, A.A. *A review on the structure, properties and characterization of 2D Molybdenum Disulfide*. in *2019 Advances in Science and Engineering Technology International Conferences (ASET)*. 2019. IEEE.

[87] Yun, W.S., Han, S., Hong, S.C., Kim, I.G., and Lee, J., (2012). Thickness and strain effects on electronic structures of transition metal dichalcogenides: 2H-M X 2 semiconductors (M= Mo, W; X= S, Se, Te). *Physical Review B*, 85(3), 033305.

[88] Zhu, Z., Cheng, Y., and Schwingenschlögl, U., (2011). Giant spin-orbit-induced spin splitting in two-dimensional transition-metal dichalcogenide semiconductors. *Physical Review B*, 84(15), 153402.

[89] Pulizzi, F. (2012) Spintronics. 2012, Nature Publishing Group.

[90] Kim, S., Konar, A., Hwang, W.-S., Lee, J.H., Lee, J., Yang, J., Jung, C., Kim, H., Yoo, J.-B., and Choi, J.-Y., (2012). High-mobility and low-power thin-film transistors based on multilayer MoS 2 crystals. *Nature communications*, 3, 1011.

[91] Lu, C.-P., Li, G., Mao, J., Wang, L.-M., and Andrei, E.Y., (2014). Bandgap, mid-gap states, and gating effects in MoS2. *Nano letters*, 14(8), 4628-4633.

[92] Lavrov, S., Shestakova, A., Avdizhiyan, A.Y., and Mishina, E., (2018). Optical Characterization of the Structural Imperfection of Two-Dimensional MoS 2 Crystallites. *Technical Physics Letters*, 44(11), 1008-1009.

[93] Meric, I., Dean, C.R., Petrone, N., Wang, L., Hone, J., Kim, P., and Shepard, K.L., (2013). Graphene field-effect transistors based on boron–nitride dielectrics. *Proceedings of the IEEE*, 101(7), 1609-1619.

[94] Melios, C., Giusca, C.E., Panchal, V., and Kazakova, O., (2018). Water on graphene: review of recent progress. *2D Mater.*, 5(2), 022001.

[95] Zhang, H., Chhowalla, M., and Liu, Z., (2018). 2D nanomaterials: graphene and transition metal dichalcogenides. *Chemical Society Reviews*, 47(9), 3015-3017.

[96] Li, X., Wang, X., Zhang, L., Lee, S., and Dai, H., (2008). Chemically derived, ultrasmooth graphene nanoribbon semiconductors. *science*, 319(5867), 1229-1232.

[97] Wang, X., Ouyang, Y., Li, X., Wang, H., Guo, J., and Dai, H., (2008). Room-temperature all-semiconducting sub-10-nm graphene nanoribbon field-effect transistors. *Physical review letters*, 100(20), 206803.

[98] Lin, M.-W., Ling, C., Zhang, Y., Yoon, H.J., Cheng, M.M.-C., Agapito, L.A., Kioussis, N., Widjaja, N., and Zhou, Z., (2011). Room-temperature high on/off ratio in suspended graphene nanoribbon field-effect transistors. *Nanotechnology*, 22(26), 265201.

[99] Yang, H., Heo, J., Park, S., Song, H.J., Seo, D.H., Byun, K.-E., Kim, P., Yoo, I., Chung, H.-J., and Kim, K., (2012). Graphene barristor, a triode device with a gate-controlled Schottky barrier. *Science*, 336(6085), 1140-1143.

[100] Britnell, L., Gorbachev, R., Jalil, R., Belle, B., Schedin, F., Mishchenko, A., Georgiou, T., Katsnelson, M., Eaves, L., and Morozov, S., (2012). Field-effect tunneling transistor based on vertical graphene heterostructures. *Science*, 335(6071), 947-950.

[101] Tong, X., Ashalley, E., Lin, F., Li, H., and Wang, Z.M., (2015). Advances in MoS2-Based Field Effect Transistors (FETs). *Nano-Micro Letters*, 7(3), 203-218.

[102] Perea-López, N., Elías, A.L., Berkdemir, A., Castro-Beltran, A., Gutiérrez, H.R., Feng, S., Lv, R., Hayashi, T., López-Urías, F., and Ghosh, S., (2013). Photosensor Device Based on Few-Layered WS2 Films. *Advanced Functional Materials*, 23(44), 5511-5517.

[103] Amani, M., Chin, M.L., Birdwell, A.G., O'Regan, T.P., Najmaei, S., Liu, Z., Ajayan, P.M., Lou, J., and Dubey, M., (2013). Electrical performance of monolayer MoS2 field-effect transistors prepared by chemical vapor deposition. *Applied Physics Letters*, 102(19), 193107.

[104] Wachter, S., Polyushkin, D.K., Bethge, O., and Mueller, T., (2017). A microprocessor based on a two-dimensional semiconductor. *Nature communications*, 8, 14948.

[105] Radisavljevic, B., Whitwick, M.B., and Kis, A., (2011). Integrated circuits and logic operations based on single-layer MoS2. *ACS nano*, 5(12), 9934-9938.

[106] Kaasbjerg, K., Thygesen, K.S., and Jacobsen, K.W., (2012). Phonon-limited mobility in n-type single-layer MoS 2 from first principles. *Physical Review B*, 85(11), 115317.

[107] Li, X., Mullen, J.T., Jin, Z., Borysenko, K.M., Nardelli, M.B., and Kim, K.W., (2013). Intrinsic electrical transport properties of monolayer silicene and MoS 2 from first principles. *Physical Review B*, 87(11), 115418.

[108] Ma, N. and Jena, D., (2014). Charge scattering and mobility in atomically thin semiconductors. *Physical Review X*, 4(1), 011043.

[109] Fivaz, R. and Mooser, E., (1967). Mobility of charge carriers in semiconducting layer structures. *Physical Review*, 163(3), 743.

[110] Radisavljevic, B. and Kis, A., (2013). Mobility engineering and a metal–insulator transition in monolayer MoS 2. *Nature materials*, 12(9), 815.

[111] Chamlagain, B., Li, Q., Ghimire, N.J., Chuang, H.-J., Perera, M.M., Tu, H., Xu, Y., Pan, M., Xaio, D., and Yan, J., (2014). Mobility improvement and temperature dependence in MoSe2 field-effect transistors on parylene-C substrate. *ACS nano*, 8(5), 5079-5088.

[112] Iqbal, M.W., Iqbal, M.Z., Khan, M.F., Shehzad, M.A., Seo, Y., Park, J.H., Hwang, C., and Eom, J., (2015). High-mobility and air-stable single-layer WS 2 field-effect transistors sandwiched between chemical vapor deposition-grown hexagonal BN films. *Scientific reports*, 5, 10699.

[113] Xu, S., Wu, Z., Lu, H., Han, Y., Long, G., Chen, X., Han, T., Ye, W., Wu, Y., and Lin, J., (2016). Universal low-temperature Ohmic contacts for quantum transport in transition metal dichalcogenides. *2D Materials*, 3(2), 021007.

[114] Ovchinnikov, D., Allain, A., Huang, Y.-S., Dumcenco, D., and Kis, A., (2014). Electrical transport properties of single-layer WS2. *ACS nano*, 8(8), 8174-8181.

[115] Liu, W., Sarkar, D., Kang, J., Cao, W., and Banerjee, K., (2015). Impact of contact on the operation and performance of back-gated monolayer MoS2 field-effect-transistors. *Acs Nano*, 9(8), 7904-7912.

[116] Das, S., Chen, H.-Y., Penumatcha, A.V., and Appenzeller, J., (2012). High performance multilayer MoS2 transistors with scandium contacts. *Nano letters*, 13(1), 100-105.

[117] Kaushik, N., Nipane, A., Basheer, F., Dubey, S., Grover, S., Deshmukh, M.M., and Lodha, S., (2014). Schottky barrier heights for Au and Pd contacts to MoS2. *Applied Physics Letters*, 105(11), 113505.

[118] Allain, A., Kang, J., Banerjee, K., and Kis, A., (2015). Electrical contacts to two-dimensional semiconductors. *Nature materials*, 14(12), 1195.

[119] Xu, Y., Cheng, C., Du, S., Yang, J., Yu, B., Luo, J., Yin, W., Li, E., Dong, S., and Ye, P., (2016). Contacts between two-and three-dimensional materials: ohmic, Schottky, and p–n heterojunctions. *ACS nano*, 10(5), 4895-4919.
[120] Liu, Y., Stradins, P., and Wei, S.-H., (2016). Van der Waals metal-semiconductor junction: Weak Fermi level pinning enables effective tuning of Schottky barrier. *Science advances*, 2(4), e1600069.
[121] McDonnell, S., Addou, R., Buie, C., Wallace, R.M., and Hinkle, C.L., (2014). Defect-dominated doping and contact resistance in MoS2. *ACS nano*, 8(3), 2880-2888.
[122] Addou, R., Colombo, L., and Wallace, R.M., (2015). Surface defects on natural MoS2. *ACS applied materials & interfaces*, 7(22), 11921-11929.
[123] Zhong, H., Quhe, R., Wang, Y., Ni, Z., Ye, M., Song, Z., Pan, Y., Yang, J., Yang, L., and Lei, M., (2016). Interfacial properties of monolayer and bilayer MoS 2 contacts with metals: Beyond the energy band calculations. *Scientific reports*, 6, 21786.
[124] Withers, F., Bointon, T.H., Hudson, D.C., Craciun, M.F., and Russo, S., (2014). Electron transport of WS 2 transistors in a hexagonal boron nitride dielectric environment. *Scientific reports*, 4, 4967.
[125] Bao, W., Cai, X., Kim, D., Sridhara, K., and Fuhrer, M.S., (2013). High mobility ambipolar MoS2 field-effect transistors: Substrate and dielectric effects. *Applied Physics Letters*, 102(4), 042104.
[126] Koppens, F., Mueller, T., Avouris, P., Ferrari, A., Vitiello, M., and Polini, M., (2014). Photodetectors based on graphene, other two-dimensional materials and hybrid systems. *Nature nanotechnology*, 9(10), 780.
[127] Xia, F., Mueller, T., Lin, Y.-m., Valdes-Garcia, A., and Avouris, P., (2009). Ultrafast graphene photodetector. *Nature nanotechnology*, 4(12), 839.
[128] Baugher, B.W., Churchill, H.O., Yang, Y., and Jarillo-Herrero, P., (2014). Optoelectronic devices based on electrically tunable p–n diodes in a monolayer dichalcogenide. *Nature nanotechnology*, 9(4), 262.
[129] Lee, C.-H., Lee, G.-H., Van Der Zande, A.M., Chen, W., Li, Y., Han, M., Cui, X., Arefe, G., Nuckolls, C., and Heinz, T.F., (2014). Atomically thin p–n junctions with van der Waals heterointerfaces. *Nature nanotechnology*, 9(9), 676.
[130] Fontana, M., Deppe, T., Boyd, A.K., Rinzan, M., Liu, A.Y., Paranjape, M., and Barbara, P., (2013). Electron-hole transport and photovoltaic effect in gated MoS 2 Schottky junctions. *Scientific reports*, 3, 1634.
[131] Yin, Z., Li, H., Li, H., Jiang, L., Shi, Y., Sun, Y., Lu, G., Zhang, Q., Chen, X., and Zhang, H., (2011). Single-layer MoS2 phototransistors. *ACS nano*, 6(1), 74-80.
[132] Kufer, D. and Konstantatos, G., (2015). Highly sensitive, encapsulated MoS2 photodetector with gate controllable gain and speed. *Nano letters*, 15(11), 7307-7313.
[133] Guo, X., Wang, W., Nan, H., Yu, Y., Jiang, J., Zhao, W., Li, J., Zafar, Z., Xiang, N., and Ni, Z., (2016). High-performance graphene photodetector using interfacial gating. *Optica*, 3(10), 1066-1070.
[134] Liu, Y., Cheng, R., Liao, L., Zhou, H., Bai, J., Liu, G., Liu, L., Huang, Y., and Duan, X., (2011). Plasmon resonance enhanced multicolour photodetection by graphene. *Nature communications*, 2, 579.

[135] Liu, M., Yin, X., Ulin-Avila, E., Geng, B., Zentgraf, T., Ju, L., Wang, F., and Zhang, X., (2011). A graphene-based broadband optical modulator. *Nature*, 474(7349), 64.
[136] Schedin, F., Lidorikis, E., Lombardo, A., Kravets, V.G., Geim, A.K., Grigorenko, A.N., Novoselov, K.S., and Ferrari, A.C., (2010). Surface-enhanced Raman spectroscopy of graphene. *ACS nano*, 4(10), 5617-5626.
[137] Cançado, L., Jorio, A., Ismach, A., Joselevich, E., Hartschuh, A., and Novotny, L., (2009). Mechanism of near-field Raman enhancement in one-dimensional systems. *Physical review letters*, 103(18), 186101.
[138] Yao, Y., Shankar, R., Rauter, P., Song, Y., Kong, J., Loncar, M., and Capasso, F., (2014). High-responsivity mid-infrared graphene detectors with antenna-enhanced photocarrier generation and collection. *Nano letters*, 14(7), 3749-3754.
[139] Lee, H.S., Min, S.-W., Chang, Y.-G., Park, M.K., Nam, T., Kim, H., Kim, J.H., Ryu, S., and Im, S., (2012). MoS2 nanosheet phototransistors with thickness-modulated optical energy gap. *Nano letters*, 12(7), 3695-3700.
[140] Lopez-Sanchez, O., Lembke, D., Kayci, M., Radenovic, A., and Kis, A., (2013). Ultrasensitive photodetectors based on monolayer MoS 2. *Nature nanotechnology*, 8(7), 497.
[141] Wang, X., Wang, P., Wang, J., Hu, W., Zhou, X., Guo, N., Huang, H., Sun, S., Shen, H., and Lin, T., (2015). Ultrasensitive and broadband MoS2 photodetector driven by ferroelectrics. *Advanced materials*, 27(42), 6575-6581.
[142] Gong, F., Luo, W., Wang, J., Wang, P., Fang, H., Zheng, D., Guo, N., Wang, J., Luo, M., and Ho, J.C., (2016). High-Sensitivity Floating-Gate Phototransistors Based on WS2 and MoS2. *Advanced Functional Materials*, 26(33), 6084-6090.
[143] Yu, Y., Zhang, Y., Song, X., Zhang, H., Cao, M., Che, Y., Dai, H., Yang, J., Zhang, H., and Yao, J., (2017). PbS-decorated WS2 phototransistors with fast response. *ACS Photonics*, 4(4), 950-956.
[144] Zhang, W., Huang, J.K., Chen, C.H., Chang, Y.H., Cheng, Y.J., and Li, L.J., (2013). High-gain phototransistors based on a CVD MoS2 monolayer. *Advanced materials*, 25(25), 3456-3461.
[145] Olutas, M., Guzelturk, B., Kelestemur, Y., Gungor, K., and Demir, H.V., (2016). Highly efficient nonradiative energy transfer from colloidal semiconductor quantum dots to wells for sensitive noncontact temperature probing. *Advanced Functional Materials*, 26(17), 2891-2899.
[146] Kholin, N., Rut'kov, E., and Tontegode, A.Y., (1984). The nature of the adsorption bond between graphite islands and iridium surface. *Surface science*, 139(1), 155-172.
[147] Li, X., Cai, W., An, J., Kim, S., Nah, J., Yang, D., Piner, R., Velamakanni, A., Jung, I., and Tutuc, E., (2009). Large-area synthesis of high-quality and uniform graphene films on copper foils. *science*, 324(5932), 1312-1314.
[148] Budania, P., Baine, P., Montgomery, J., McGeough, C., Cafolla, T., Modreanu, M., McNeill, D., Mitchell, N., Hughes, G., and Hurley, P., (2017). Long-term stability of mechanically exfoliated MoS2 flakes. *MRS Communications*, 7(04), 813-818.
[149] Lin, Z., McCreary, A., Briggs, N., Subramanian, S., Zhang, K., Sun, Y., Li, X., Borys, N.J., Yuan, H., and Fullerton-Shirey, S.K., (2016). 2D materials advances: from large scale synthesis and controlled heterostructures to improved characterization techniques, defects and applications. *2D Materials*, 3(4), 042001.

[150] Ferrari, A.C., Meyer, J., Scardaci, V., Casiraghi, C., Lazzeri, M., Mauri, F., Piscanec, S., Jiang, D., Novoselov, K., and Roth, S., (2006). Raman spectrum of graphene and graphene layers. *Physical review letters*, 97(18), 187401.
[151] Ferraro, J.R., *Introductory raman spectroscopy*. 2003: Elsevier.
[152] Li, H., Zhang, Q., Yap, C.C.R., Tay, B.K., Edwin, T.H.T., Olivier, A., and Baillargeat, D., (2012). From bulk to monolayer MoS2: evolution of Raman scattering. *Advanced Functional Materials*, 22(7), 1385-1390.
[153] Ortiz-Conde, A., Sánchez, F.G., Liou, J.J., Cerdeira, A., Estrada, M., and Yue, Y., (2002). A review of recent MOSFET threshold voltage extraction methods. *Microelectronics reliability*, 42(4-5), 583-596.
[154] Kufer, D., Nikitskiy, I., Lasanta, T., Navickaite, G., Koppens, F.H., and Konstantatos, G., (2015). Hybrid 2D–0D MoS2–PbS quantum dot photodetectors. *Advanced materials*, 27(1), 176-180.
[155] Özden, A., Ay, F., Sevik, C., and Perkgöz, N.K., (2017). CVD growth of monolayer MoS2: Role of growth zone configuration and precursors ratio. *Japanese Journal of Applied Physics*, 56(6S1), 06GG05.
[156] Cunningham, P.D., McCreary, K.M., Hanbicki, A.T., Currie, M., Jonker, B.T., and Hayden, L.M., (2016). Charge Trapping and Exciton Dynamics in Large-Area CVD Grown MoS2. *The Journal of Physical Chemistry C*, 120(10), 5819-5826.
[157] Şar, H., Özden, A., Demiroğlu, İ., Sevik, C., Perkgoz, N.K., and Ay, F., (2019). Long-Term Stability Control of CVD-Grown Monolayer MoS2. *physica status solidi (RRL) – Rapid Research Letters*, 13(7), 1800687.
[158] van der Zande, A.M., Huang, P.Y., Chenet, D.A., Berkelbach, T.C., You, Y., Lee, G.H., Heinz, T.F., Reichman, D.R., Muller, D.A., and Hone, J.C., (2013). Grains and grain boundaries in highly crystalline monolayer molybdenum disulphide. *Nat Mater*, 12(6), 554-61.
[159] Gao, J., Li, B., Tan, J., Chow, P., Lu, T.M., and Koratkar, N., (2016). Aging of Transition Metal Dichalcogenide Monolayers. *ACS Nano*, 10(2), 2628-35.
[160] Wang, Q.H., Kalantar-Zadeh, K., Kis, A., Coleman, J.N., and Strano, M.S., (2012). Electronics and optoelectronics of two-dimensional transition metal dichalcogenides. *Nature nanotechnology*, 7(11), 699.
[161] Mak, K.F., Lee, C., Hone, J., Shan, J., and Heinz, T.F., (2010). Atomically thin MoS 2: a new direct-gap semiconductor. *Physical review letters*, 105(13), 136805.
[162] Zeng, H., Dai, J., Yao, W., Xiao, D., and Cui, X., (2012). Valley polarization in MoS2 monolayers by optical pumping. *Nat Nanotechnol*, 7(8), 490-3.
[163] Cai, Z., Liu, B., Zou, X., and Cheng, H.-M., (2018). Chemical Vapor Deposition Growth and Applications of Two-Dimensional Materials and Their Heterostructures. *Chemical Reviews*.
[164] Sun, J., Li, X., Guo, W., Zhao, M., Fan, X., Dong, Y., Xu, C., Deng, J., and Fu, Y., (2017). Synthesis Methods of Two-Dimensional MoS2: A Brief Review. *Crystals*, 7(7).
[165] Zhan, L., Wan, W., Zhu, Z., Shih, T.-M., and Cai, W., (2017). MoS2 materials synthesized on SiO2/Si substrates via MBE. *Journal of Physics: Conference Series*, 864.
[166] Liu, L., Qiu, H., Wang, J., Xu, G., and Jiao, L., (2016). Atomic MoS2 monolayers synthesized from a metal-organic complex by chemical vapor deposition. *Nanoscale*, 8(8), 4486-90.
[167] Yang, P., Zou, X., Zhang, Z., Hong, M., Shi, J., Chen, S., Shu, J., Zhao, L., Jiang, S., Zhou, X., Huan, Y., Xie, C., Gao, P., Chen, Q., Zhang, Q., Liu, Z., and Zhang,

Y., (2018). Batch production of 6-inch uniform monolayer molybdenum disulfide catalyzed by sodium in glass. *Nat Commun*, 9(1), 979.
[168] Hao, S., Yang, B., and Gao, Y., (2017). Orientation-specific transgranular fracture behavior of CVD-grown monolayer MoS2 single crystal. *Applied Physics Letters*, 110(15).
[169] Liu, Z., Amani, M., Najmaei, S., Xu, Q., Zou, X., Zhou, W., Yu, T., Qiu, C., Birdwell, A.G., Crowne, F.J., Vajtai, R., Yakobson, B.I., Xia, Z., Dubey, M., Ajayan, P.M., and Lou, J., (2014). Strain and structure heterogeneity in MoS2 atomic layers grown by chemical vapour deposition. *Nat Commun*, 5, 5246.
[170] Martincova, J., Otyepka, M., and Lazar, P., (2017). Is Single Layer MoS2 Stable in the Air? *Chemistry*, 23(53), 13233-13239.
[171] Kc, S., Longo, R.C., Wallace, R.M., and Cho, K., (2015). Surface oxidation energetics and kinetics on MoS2 monolayer. *Journal of Applied Physics*, 117(13).
[172] Wu, D., Huang, H., Zhu, X., He, Y., Xie, Q., Chen, X., Zheng, X., Duan, H., and Gao, Y., (2016). E''Raman Mode in Thermal Strain-Fractured CVD-MoS2. *Crystals*, 6(11), 151.
[173] Niehues, I., Blob, A., Stiehm, T., Schmidt, R., Jadriško, V., Radatović, B., Čapeta, D., Kralj, M., de Vasconcellos, S.M., and Bratschitsch, R., (2018). Strain transfer across grain boundaries in MoS2 monolayers grown by chemical vapor deposition. *2D Materials*, 5(3), 031003.
[174] Castellanos-Gomez, A., Roldan, R., Cappelluti, E., Buscema, M., Guinea, F., van der Zant, H.S., and Steele, G.A., (2013). Local strain engineering in atomically thin MoS2. *Nano Lett*, 13(11), 5361-6.
[175] Zhou, W., Zou, X., Najmaei, S., Liu, Z., Shi, Y., Kong, J., Lou, J., Ajayan, P.M., Yakobson, B.I., and Idrobo, J.C., (2013). Intrinsic structural defects in monolayer molybdenum disulfide. *Nano Lett*, 13(6), 2615-22.
[176] Cao, D., Shen, T., Liang, P., Chen, X., and Shu, H., (2015). Role of Chemical Potential in Flake Shape and Edge Properties of Monolayer MoS2. *The Journal of Physical Chemistry C*, 119(8), 4294-4301.
[177] Chin, H.-T., Lee, J.-J., Hofmann, M., and Hsieh, Y.-P., (2018). Impact of growth rate on graphene lattice-defect formation within a single crystalline domain. *Scientific reports*, 8(1), 4046.
[178] Tongay, S., Zhou, J., Ataca, C., Liu, J., Kang, J.S., Matthews, T.S., You, L., Li, J., Grossman, J.C., and Wu, J., (2013). Broad-range modulation of light emission in two-dimensional semiconductors by molecular physisorption gating. *Nano letters*, 13(6), 2831-2836.
[179] Nan, H., Wang, Z., Wang, W., Liang, Z., Lu, Y., Chen, Q., He, D., Tan, P., Miao, F., and Wang, X., (2014). Strong photoluminescence enhancement of MoS2 through defect engineering and oxygen bonding. *ACS nano*, 8(6), 5738-5745.
[180] Zhao, H.-Q., Mao, X., Zhou, D., Feng, S., Shi, X., Ma, Y., Wei, X., and Mao, Y., (2016). Bandgap modulation of MoS 2 monolayer by thermal annealing and quick cooling. *Nanoscale*, 8(45), 18995-19003.
[181] Gutierrez, H.R., Perea-Lopez, N., Elias, A.L., Berkdemir, A., Wang, B., Lv, R., Lopez-Urias, F., Crespi, V.H., Terrones, H., and Terrones, M., (2013). Extraordinary room-temperature photoluminescence in triangular WS2 monolayers. *Nano Lett*, 13(8), 3447-54.
[182] Özden, A., Şar, H., Yeltik, A., Madenoğlu, B., Sevik, C., Ay, F., and Perkgöz, N.K., (2016). CVD grown 2D MoS2layers: A photoluminescence and

fluorescence lifetime imaging study. *physica status solidi (RRL) - Rapid Research Letters*, 10(11), 792-796.
[183] Adelifard, M., Salamatizadeh, R., and Ketabi, S., (2016). Fabrication and characterization of nanostructural WS2/WO3 binary compound semiconductors prepared by the sulfurization of sprayed thin films. *Journal of Materials Science: Materials in Electronics*, 27(5), 5243-5250.
[184] Li, X. and Zhu, H., (2015). Two-dimensional MoS2: Properties, preparation, and applications. *Journal of Materiomics*, 1(1), 33-44.
[185] Brainard, W. (1969) The thermal stability and friction of the disulfides, diselenides, and ditellurides of molybdenum and tungsten in vacuum, in *Nasa TN D5141*. 1969: Nasa Technical Note.
[186] Zhang, W., Huang, Z., Zhang, W., and Li, Y., (2014). Two-dimensional semiconductors with possible high room temperature mobility. *Nano Research*, 7(12), 1731-1737.
[187] Lan, C., Li, C., Yin, Y., and Liu, Y., (2015). Large-area synthesis of monolayer WS2 and its ambient-sensitive photo-detecting performance. *Nanoscale*, 7(14), 5974-5980.
[188] Perkins, F.K., Friedman, A.L., Cobas, E., Campbell, P., Jernigan, G., and Jonker, B.T., (2013). Chemical vapor sensing with monolayer MoS2. *Nano letters*, 13(2), 668-673.
[189] Ahn, J.-H., Parkin, W.M., Naylor, C.H., Johnson, A.C., and Drndić, M., (2017). Ambient effects on electrical characteristics of CVD-grown monolayer MoS2 field-effect transistors. *Scientific Reports*, 7.
[190] Cong, C., Shang, J., Wu, X., Cao, B., Peimyoo, N., Qiu, C., Sun, L., and Yu, T., (2014). Synthesis and Optical Properties of Large-Area Single-Crystalline 2D Semiconductor WS2 Monolayer from Chemical Vapor Deposition. *Advanced Optical Materials*, 2(2), 131-136.
[191] Shi, W., Lin, M.-L., Tan, Q.-H., Qiao, X.-F., Zhang, J., and Tan, P.-H., (2016). Raman and photoluminescence spectra of two-dimensional nanocrystallites of monolayer WS2and WSe2. *2D Materials*, 3(2).
[192] Zhu, B., Chen, X., and Cui, X., (2015). Exciton binding energy of monolayer WS2. *Scientific reports*, 5.
[193] Fan, Y., Zhou, Y., Wang, X., Tan, H., Rong, Y., and Warner, J.H., (2016). Photoinduced Schottky Barrier Lowering in 2D Monolayer WS2Photodetectors. *Advanced Optical Materials*, 4(10), 1573-1581.
[194] Peimyoo, N., Yang, W., Shang, J., Shen, X., Wang, Y., and Yu, T., (2014). Chemically driven tunable light emission of charged and neutral excitons in monolayer WS2. *ACS nano*, 8(11), 11320-11329.
[195] Mouri, S., Miyauchi, Y., and Matsuda, K., (2013). Tunable photoluminescence of monolayer MoS2 via chemical doping. *Nano letters*, 13(12), 5944-5948.
[196] Giannazzo, F., Fisichella, G., Piazza, A., Di Franco, S., Greco, G., Agnello, S., and Roccaforte, F., (2017). Impact of contact resistance on the electrical properties of MoS2 transistors at practical operating temperatures. *Beilstein journal of nanotechnology*, 8, 254.
[197] Nourbakhsh, A., Zubair, A., Joglekar, S., Dresselhaus, M., and Palacios, T., (2017). Subthreshold swing improvement in MoS 2 transistors by the negative-capacitance effect in a ferroelectric Al-doped-HfO 2/HfO 2 gate dielectric stack. *Nanoscale*, 9(18), 6122-6127.

[198] Tian, H., Chin, M.L., Najmaei, S., Guo, Q., Xia, F., Wang, H., and Dubey, M., (2016). Optoelectronic devices based on two-dimensional transition metal dichalcogenides. *Nano Research*, 9(6), 1543-1560.
[199] Perea-López, N., Lin, Z., Pradhan, N.R., Iñiguez-Rábago, A., Elías, A.L., McCreary, A., Lou, J., Ajayan, P.M., Terrones, H., and Balicas, L., (2014). CVD-grown monolayered MoS2 as an effective photosensor operating at low-voltage. *2D Materials*, 1(1), 011004.
[200] Xie, C., Mak, C., Tao, X., and Yan, F., (2017). Photodetectors Based on Two-Dimensional Layered Materials Beyond Graphene. *Advanced Functional Materials*, 27(19).
[201] Zeng, L., Tao, L., Tang, C., Zhou, B., Long, H., Chai, Y., Lau, S.P., and Tsang, Y.H., (2016). High-responsivity UV-vis photodetector based on transferable ws2 film deposited by magnetron sputtering. *Scientific reports*, 6.
[202] Li, Y., Chernikov, A., Zhang, X., Rigosi, A., Hill, H.M., van der Zande, A.M., Chenet, D.A., Shih, E.-M., Hone, J., and Heinz, T.F., (2014). Measurement of the optical dielectric function of monolayer transition-metal dichalcogenides: MoS 2, Mo S e 2, WS 2, and WS e 2. *Physical Review B*, 90(20), 205422.
[203] Lloyd, D., Liu, X., Christopher, J.W., Cantley, L., Wadehra, A., Kim, B.L., Goldberg, B.B., Swan, A.K., and Bunch, J.S., (2016). Band Gap Engineering with Ultralarge Biaxial Strains in Suspended Monolayer MoS2. *Nano Lett*, 16(9), 5836-41.
[204] Huo, N., Yang, S., Wei, Z., Li, S.-S., Xia, J.-B., and Li, J., (2014). Photoresponsive and gas sensing field-effect transistors based on multilayer WS 2 nanoflakes. *Scientific reports*, 4, 5209.
[205] Zeng, Q. and Liu, Z., (2018). Novel Optoelectronic Devices: Transition-Metal-Dichalcogenide-Based 2D Heterostructures. *Advanced Electronic Materials*, 4(2), 1700335.
[206] Tsai, M.-L., Su, S.-H., Chang, J.-K., Tsai, D.-S., Chen, C.-H., Wu, C.-I., Li, L.-J., Chen, L.-J., and He, J.-H., (2014). Monolayer MoS2 heterojunction solar cells. *ACS nano*, 8(8), 8317-8322.
[207] Eda, G. and Maier, S.A., (2013). Two-dimensional crystals: managing light for optoelectronics. *Acs Nano*, 7(7), 5660-5665.
[208] Xia, F., Wang, H., Xiao, D., Dubey, M., and Ramasubramaniam, A., (2014). Two-dimensional material nanophotonics. *Nature Photonics*, 8(12), 899.
[209] Ithurria, S., Tessier, M., Mahler, B., Lobo, R., Dubertret, B., and Efros, A.L., (2011). Colloidal nanoplatelets with two-dimensional electronic structure. *Nature materials*, 10(12), 936.
[210] Tessier, M.D., Javaux, C., Maksimovic, I., Loriette, V., and Dubertret, B., (2012). Spectroscopy of single CdSe nanoplatelets. *ACS nano*, 6(8), 6751-6758.
[211] Dede, D., Taghipour, N., Quliyeva, U., Sak, M., Kelestemur, Y., Gungor, K., and Demir, H.V., (2019). Highly stable multicrown heterostructures of type-II nanoplatelets for ultralow threshold optical gain. *Chemistry of Materials*, 31(5), 1818-1826.
[212] Taghipour, N., Delikanli, S., Shendre, S., Sak, M., Li, M., Isik, F., Tanriover, I., Guzelturk, B., Sum, T.C., and Demir, H.V., (2019). Sub-single exciton optical gain threshold in colloidal semiconductor quantum wells with gradient alloy shelling. *arXiv preprint arXiv:1906.06913*.

[213] Guzelturk, B., Kelestemur, Y., Olutas, M., Delikanli, S., and Demir, H.V., (2014). Amplified spontaneous emission and lasing in colloidal nanoplatelets. *Acs Nano*, 8(7), 6599-6605.
[214] Liu, B., Delikanli, S., Gao, Y., Dede, D., Gungor, K., and Demir, H.V., (2018). Nanocrystal light-emitting diodes based on type II nanoplatelets. *Nano Energy*, 47, 115-122.
[215] Sharma, M., Gungor, K., Yeltik, A., Olutas, M., Guzelturk, B., Kelestemur, Y., Erdem, T., Delikanli, S., McBride, J.R., and Demir, H.V., (2017). Near-Unity Emitting Copper-Doped Colloidal Semiconductor Quantum Wells for Luminescent Solar Concentrators. *Advanced Materials*, 29(30), 1700821.
[216] Yang, Y., Huo, N., and Li, J., (2017). Sensitized monolayer MoS 2 phototransistors with ultrahigh responsivity. *Journal of Materials Chemistry C*, 5(44), 11614-11619.
[217] Choi, M.S., Qu, D., Lee, D., Liu, X., Watanabe, K., Taniguchi, T., and Yoo, W.J., (2014). Lateral MoS2 p–n junction formed by chemical doping for use in high-performance optoelectronics. *ACS nano*, 8(9), 9332-9340.
[218] Huo, N. and Konstantatos, G., (2017). Ultrasensitive all-2D MoS 2 phototransistors enabled by an out-of-plane MoS 2 PN homojunction. *Nature communications*, 8(1), 572.
[219] Yu, S.H., Lee, Y., Jang, S.K., Kang, J., Jeon, J., Lee, C., Lee, J.Y., Kim, H., Hwang, E., and Lee, S., (2014). Dye-sensitized MoS2 photodetector with enhanced spectral photoresponse. *ACS nano*, 8(8), 8285-8291.
[220] Hsiao, Y.-J., Fang, T.-H., Ji, L.-W., and Yang, B.-Y., (2015). Red-shift effect and sensitive responsivity of MoS 2/ZnO flexible photodetectors. *Nanoscale research letters*, 10(1), 443.
[221] Zhang, W., Chuu, C.-P., Huang, J.-K., Chen, C.-H., Tsai, M.-L., Chang, Y.-H., Liang, C.-T., Chen, Y.-Z., Chueh, Y.-L., and He, J.-H., (2014). Ultrahigh-gain photodetectors based on atomically thin graphene-MoS 2 heterostructures. *Scientific reports*, 4, 3826.
[222] Yu, W.J., Liu, Y., Zhou, H., Yin, A., Li, Z., Huang, Y., and Duan, X., (2013). Highly efficient gate-tunable photocurrent generation in vertical heterostructures of layered materials. *Nature nanotechnology*, 8(12), 952.
[223] Deng, W., Chen, Y., You, C., Liu, B., Yang, Y., Shen, G., Li, S., Sun, L., Zhang, Y., and Yan, H., (2018). High Detectivity from a Lateral Graphene–MoS2 Schottky Photodetector Grown by Chemical Vapor Deposition. *Advanced Electronic Materials*, 4(9), 1800069.
[224] Kufer, D., Lasanta, T., Bernechea, M., Koppens, F.H., and Konstantatos, G., (2016). Interface engineering in hybrid quantum dot–2D phototransistors. *ACS Photonics*, 3(7), 1324-1330.
[225] Huo, N., Kang, J., Wei, Z., Li, S.S., Li, J., and Wei, S.H., (2014). Novel and enhanced optoelectronic performances of multilayer MoS2–WS2 heterostructure transistors. *Advanced Functional Materials*, 24(44), 7025-7031.
[226] Taghipour, N., Hernandez Martinez, P.L., Ozden, A., Olutas, M., Dede, D., Gungor, K., Erdem, O., Perkgoz, N.K., and Demir, H.V., (2018). Near-Unity Efficiency Energy Transfer from Colloidal Semiconductor Quantum Wells of CdSe/CdS Nanoplatelets to a Monolayer of MoS2. *ACS nano*, 12(8), 8547-8554.
[227] Guzelturk, B. and Demir, H.V., (2016). Near-Field Energy Transfer Using Nanoemitters For Optoelectronics. *Advanced Functional Materials*, 26(45), 8158-8177.

[228] Forster, T., (1946). Energiewanderung und fluoreszenz. *Naturwissenschaften*, 33(6), 166-175.
[229] Şar, H., Özden, A., Demiroğlu, İ., Sevik, C., Perkgoz, N.K., and Ay, F., Long-Term Stability Control of CVD-Grown Monolayer MoS2. *physica status solidi (RRL)–Rapid Research Letters*, 1800687.
[230] Di Bartolomeo, A., Grillo, A., Urban, F., Iemmo, L., Giubileo, F., Luongo, G., Amato, G., Croin, L., Sun, L., and Liang, S.J., (2018). Asymmetric schottky contacts in bilayer MoS2 field effect transistors. *Advanced Functional Materials*, 28(28), 1800657.
[231] Şar, H., Özden, A., Yorulmaz, B., Sevik, C., Perkgoz, N.K., and Ay, F., (2018). A comparative device performance assesment of CVD grown MoS 2 and WS 2 monolayers. *Journal of Materials Science: Materials in Electronics*, 29(10), 8785-8792.
[232] Island, J.O., Blanter, S.I., Buscema, M., van der Zant, H.S., and Castellanos-Gomez, A., (2015). Gate controlled photocurrent generation mechanisms in high-gain In2Se3 phototransistors. *Nano letters*, 15(12), 7853-7858.
[233] Wu, H., Kang, Z., Zhang, Z., Zhang, Z., Si, H., Liao, Q., Zhang, S., Wu, J., Zhang, X., and Zhang, Y., (2018). Interfacial Charge Behavior Modulation in Perovskite Quantum Dot-Monolayer MoS2 0D-2D Mixed-Dimensional van der Waals Heterostructures. *Advanced Functional Materials*, 28(34), 1802015.
[234] Li, L., Wang, W., Chai, Y., Li, H., Tian, M., and Zhai, T., (2017). Few-Layered PtS2 Phototransistor on h-BN with High Gain. *Advanced Functional Materials*, 27(27), 1701011.
[235] Li, H.-M., Lee, D.-Y., Choi, M.S., Qu, D., Liu, X., Ra, C.-H., and Yoo, W.J., (2014). Metal-semiconductor barrier modulation for high photoresponse in transition metal dichalcogenide field effect transistors. *Scientific reports*, 4, 4041.
[236] Pradhan, S.K., Xiao, B., and Pradhan, A.K., (2016). Energy band alignment of high-k oxide heterostructures at MoS2/Al2O3 and MoS2/ZrO2 interfaces. *Journal of Applied Physics*, 120(12), 125305.
[237] Sangwan, V.K., Arnold, H.N., Jariwala, D., Marks, T.J., Lauhon, L.J., and Hersam, M.C., (2013). Low-frequency electronic noise in single-layer MoS2 transistors. *Nano letters*, 13(9), 4351-4355.

RESUME

Name Surname : Hüseyin ŞAR

Foreign Language : English

Birth Place and Date : Adıyaman / 01.07.1987

E-Mail : hsar@eskisehir.edu.tr , hsar413@gmail.com

EDUCATION

2014-Current	Eskisehir Technical University (Anadolu University)	Ph.D.
2012-2014	Anadolu University	M.Sc.
2005-2009	Mustafa Kemal University	B.Sc.

SCI PUBLICATIONS

1. **Şar, H. ,** Özden, A. , Demiroğlu, İ. , Sevik, C. , Perkgoz, N. K. and Ay, F. (**2019**), Long-Term Stability Control of CVD-Grown Monolayer MoS2. **Phys. Status Solidi RRL**, doi:10.1002/pssr.201800687

2. B. Yorulmaz, A. Özden, **H. Şar**, F. Ay, C. Sevik, N.K. Perkgöz "CVD growth of monolayer WS2 through controlled seed formation and vapor density" ***Materials Science in Semiconductor Processing, 2019***

3. **H. Şar**, A. Özden, B. Yorulmaz, C. Sevik, N. K. Perkgoz, F. Ay "A Comparative Device Performance Assesment of CVD Grown MoS_2 and WS_2 Monolayers " ***Journal of Materials Science: Materials in Electronics, 2018.***

4. A. Özden, **H. Şar,** A. Yeltik, B. Madenoğlu, C. Sevik, F. Ay, N. K. Perkgöz, "CVD grown 2-D MoS_2 layers: A photoluminescence and fluorescence lifetime imaging study" ***Physica Status Solidi (RRL), 2016***

5. Y Hameş, SE San, T Özdal, E Aslan, H Çabalak, **H. Şar**, "Manufacturing of inorganic-organic hybrid solar cells by screen printing method", ***Turkish Journal of Engineering and Environmental Sciences, 2011.***

CONFERENCES & WORKSHOPS

1. **H. Şar**, M. Bay, C. Sevik, H. V. Demir, N. K. Perkgoz, F. Ay, "Transport Properties of P-Type 2D $MoSe_2$ Field Effect Transistor", E-MRS Spring Meeting,

2019,Nice, France, **Submitted**

2. **H. Şar**, A. Özden, I. Demiroglu, C. Sevik, N. K. Perkgoz, F. Ay, "The Effect of CVD Growth Configuration on the stability of MoS_2", Graphene 2019, Rome, Italy, 2019, **Submitted**

3. A. Özden, **H. Şar**, C. Odacı , C. Sevik, F. Ay, N. K. Perkgöz "Time Dependent Structural Analysis of CVD Grown MoS_2 Flakes With Different Configurations" Solid State Devices and Materials 2017, pp1023-1024, Sendai, Japan, 2017.

4. **H. Şar**, A. Özden, C. Odacı, C. Sevik, N. K. Perkgöz, F. Ay, "Investigation of Long Term Electrical Transport Stability of MoS_2 Flakes" Solid State Devices and Materials 2017, pp1027-1028, Sendai, Japan, 2017.

5. **H. Şar,** A. Özden, B. Yorulmaz, C. Sevik, N.K. Perkgöz, F. Ay, "A Comparative Study on Transport Properties of 2D MoS2 and WS2 Field Effect Transistors" 13th Nanoscience and Nanotechnology Congress, Antalya, Turkey, 2017.

6. M. Bay, **H. Şar**, C. Sevik, N.K. Perkgöz, F. Ay, "Phototransistor Fabrication Based on CVD Grown 2D $MoSe_2$ films" 13th Nanoscience and Nanotechnology Congress, Antalya, Turkey, 2017.

7. A. Özden, U. Savacı, **H. Şar**, C. Sevik, N. K. Perkgoz, S. Turan, F. Ay, "Evolution of 2D MoS_2 Structures as a Function of the Hydrogen Flow Rate" 13th Nanoscience and Nanotechnology Congress, Antalya, Turkey, 2017.

8. **H. Şar,** A. Özden, B. Yorulmaz, C. Sevik, N.K. Perkgöz, F. Ay, "A Comparative Study on Transport Properties of 2D MoS2 and WS2 Field Effect Transistors" 13th Nanoscience and Nanotechnology Congress, Antalya, Turkey, 2017.

9. A. Özden, B. Yorulmaz, **H. Şar**, C. Sevik, F. Ay, N. K. Perkgöz "CVD Formation of Hetero of Hetero 2D MoS2-WS2 Flakes" 13th Nanoscience and Nanotechnology Congress, Antalya, Turkey, 2017.

10. **H. Şar,** A. Özden, O. Balcı, C. Kocabaş, N. K. Perkgöz, F. Ay, C. Sevik,. "Systematic Characterization of MoS2 CVD Growth on Transferred and As-grown Graphene", European MRS, Fall Meeting, Lille, France**,** 2016

11. I.Kyriakides, R. Pribic, **H. Şar**, N. At, "GRID matching in Monte Carlo Bayesian compressive sensing" 16th International Conference on Information Fusion (FUSION), 2013, Full Paper**.**

12. **H. Şar**, C. Topal, N. At, Ö. N. Gerek, "Improving the efficiency of predictive coders via adaptive multiple predictor cooperation", IEEE International Conference on Acoustics, Speech and Signal Processing (ICASSP - 2013), 2013, Full Paper**.**